

11/11/10  
TD-10-023

## LARP LQS01b Magnet Test Summary

G. Chlachidze, G. Ambrosio, N. Andreev, E. Barzi, R. Carcagno, S. Caspi, D. Dietderich,  
H. Felice, P. Ferracin, A. Ghosh, V.V. Kashikhin, M.J. Kim, M.J. Lamm, F. Lewis, F. Nobrega,  
I. Novitski, D. Orris, G.L. Sabbi, J. Schmalzle, C. Sylvester, M. Tartaglia, J.C. Tompkins,  
G. Velev, P. Wanderer, A.V. Zlobin

### Content:

1. Introduction	2
2. LQS01a disassembly and LQS01b assembly	2
3. LQS01b Instrumentation	3
4. Quench History	7
5. Ramp rate dependence	11
6. Temperature dependence	16
7. Quench Locations	16
8. Strain Gauge Data	19
9. Magnetic measurements	51
10. Spike Data Analysis	58
11. Summary	60
Attachment I	62
Attachment II	63

# 1. Introduction

In December 2009 during its first cold test, LQS01a, the first long Nb<sub>3</sub>Sn quadrupole made by LARP (LHC Accelerator Research Program), reached its target field gradient of 200 T/m [1]. This target was set in 2005 by the US Department of Energy, CERN and LARP, as a significant milestone toward the development of Nb<sub>3</sub>Sn quadrupoles for possible use in LHC luminosity upgrades.

Despite this significant achievement the LQS01a training was stopped at 202 T/m in order to avoid possible coil damages. Training history, strain-gauge data, and temperature dependence showed that the quench training was strongly affected by low pre-stress in the inner layer. Analysis of the strain-gauge data after pre-load [2] and after cool-down, together with FE modeling, showed that this non-optimal pre-stress distribution could be caused by a mismatch between coil outer diameter (OD) and structure inner (ID) diameter. The computed stress could degrade the coil at currents higher than the target. The magnet was subsequently disassembled, inspected, and reassembled with higher and more uniform preload [3] using all four original coils (#6-#9). More details on the magnet reassembly are presented in Section 2.

The LQS01 coils were made of 27-strand Rutherford cable with 0.7-mm Nb<sub>3</sub>Sn strand based on the “Restack Rod Process” (RRP) of 54/61 sub-element design. The coil layout is equal to the layout used in the LARP Technological Quadrupoles (TQC and TQS models). Pre-stress and support are provided by a segmented aluminum shell pre-loaded using bladders and keys, similarly to the TQS models. Details of the design, coil fabrication, magnet assembly and instrumentation can be found in [4]. Description of the magnet also can be found in [5].

The reassembled magnet LQS01b was delivered to the Fermilab’s vertical magnet test facility (VMTF) on June 8<sup>th</sup>, 2010. The magnet was installed into the VMTF dewar and it was electrically checked by June 18<sup>th</sup>, 2010. Cool down started after warm magnetic measurements on June 22 and the VMTF dewar was filled with liquid helium on June 30. Test was started on July 1<sup>st</sup> and first test cycle was completed on July 31<sup>st</sup>. Then the magnet was warmed up for a thermal cycling from August 2<sup>nd</sup> to August 11<sup>th</sup> so that the lowest temperature of the magnet was not less than 270 K. The magnet was cooled down again from August 12<sup>th</sup> to August 18<sup>th</sup>. The 2<sup>nd</sup> test cycle was performed only at 4.5 K and test was completed on August 26<sup>th</sup>. Finally the LQS01b magnet has been removed from the VMTF dewar on September 13<sup>th</sup>, 2010.

Additional warm magnetic measurements were done with the new Fermilab mole-type probe (locally called the “Ferret”) designed specifically to use circuit-board probes driven externally through a flexible shaft.

## 2. LQS01a Disassembly and LQS01b Assembly

The LQS01 pre-stress target values were chosen in order to avoid separation between coil and pole at field gradient of 230-240 T/m, according to FEM computation. In LQS01a, the aluminum shell and stainless steel rods reached after cool-down a pre-

tension consistent with calculations. On the contrary a large discrepancy was observed between measured and expected azimuthal coil pre-load [3]. In addition, most of the pole gauges showed a “stress plateau” during current ramps indicating coil-pole separation.

After the LQS01a test, the magnet was unloaded and disassembled at LBNL. Tests with pressure sensitive paper confirmed the mismatch between the coil outer surface and the pad inner surface. Based on the results of these tests and additional measurements, it was decided to apply two modifications to LQS01b structure and loading. The thickness of the G10 shim providing electrical insulation between coils and pads was reduced from 0.765 mm to 0.380 mm. In addition the pre-load was increased, based on the successful experience with the TQS03 series [6], to further mitigate the risk of low coil pre-stress. After the modifications were implemented the pole compression at cold increased to  $-130 \pm 31$  MPa (corresponding to 165 MPa in the coil), and no separation was observed between coil and pole during excitation.

### 3. LQS01b Instrumentation

The LQS01b magnet was built using coils #6, #7, #8 and #9. Each coil is equipped with 4 protection heaters and 1 spot heater. Protection heaters are installed on both the outer and inner coil surfaces. Protection heaters (see Fig. 1) were made of stainless steel with 6.2-6.7 Ohm resistance at room temperature.

The 15-kA top plate assembly at VMTF was modified to accommodate more protection heaters. 8 additional pairs of wire were routed through the “Lambda” plate and the header which made it possible to bring out signals from 16 heaters in total. 14 protection heaters and two spot heaters of LQS01b were wired individually and only two protection heaters (on the outer layer return end of coils 6 and 8) were connected in parallel at the heater Hypertronics connector mounted on the magnet shell. More heaters wired individually provided required flexibility in case of a heater failure during the cold test. All heater signals were brought to the distribution box at VMTF where the final connections were made to the heater firing units (HFU).

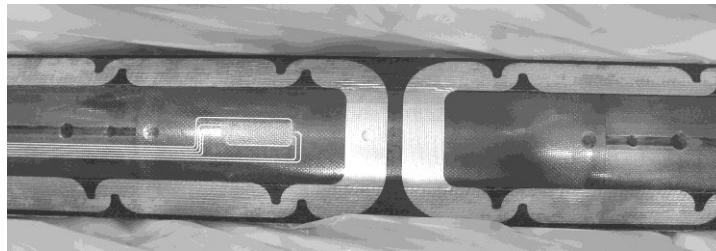


Fig. 1. LQS01 protection heaters.

Protection heaters were connected in 4 groups. In each group all heaters on the same coil layer and at the same side (lead end or return end) are connected in parallel. Only one heater on the outer layer return end in coil #7 (PH07B02) failed the heater-to-coil hipot test and was removed from the magnet protection. Another heater on the inner layer lead end in coil #7 (PH07A01) was damaged during the LQS01a test. After the test this heater

was found open with a carbon spot at a heating station. Heater “stations” are narrow parts of heater trace equidistantly distributed longitudinally (see Fig. 1). This protection heater was cleaned and repaired: exposed area was filled with Stycast and 5-mil Kapton on top of it and cured with pressure. Damaged area of the heater was replaced with a copper wire (see Fig. 2). After a few quenches in LQS01b the same PH07A01 heater failed again and was removed from the magnet protection. An external 4.5-Ohm dummy load was connected instead. Peak current in the individual heaters during the test varied from 48 A to 52 A.

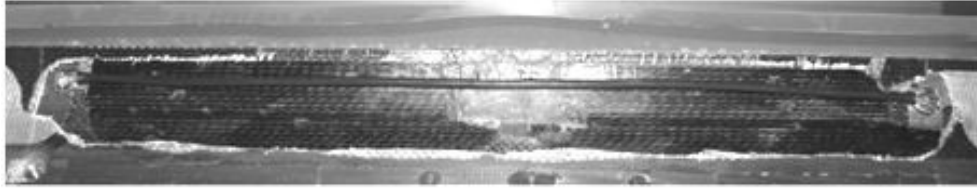


Fig. 2. Repaired protection heater PH07A01.

Voltage tap system in LQS01b covers the inner and outer coil layers, pole turn, multi-turn and splice sections (see Fig. 3). There are 13 voltage taps on the inner layer and 7 voltage taps on the outer layer. Only one voltage tap was missing: **B7** in coil #9 was lost before the cool down of LQS01a. After 10 quenches in LQS01b voltage tap **A7** both in coil #6 and #9 became floating and were removed from the data taking. LQS01b magnet schematic is similar to one for LQS01a and is shown in Attachment I.

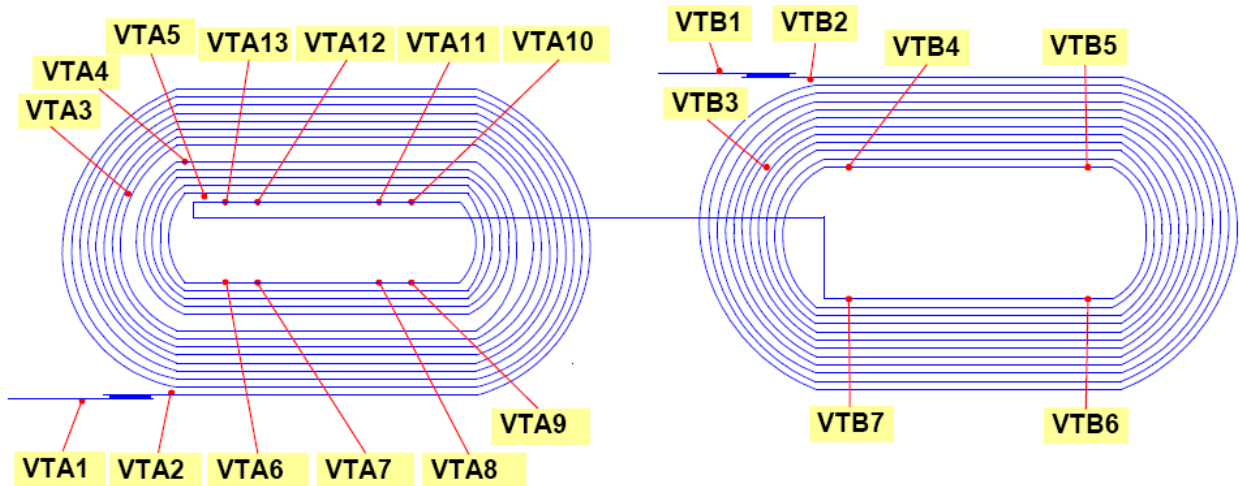


Fig. 3. LQS01b voltage tap locations for the inner (left) and outer (right) layers

56 strain gauges (SG) were installed on shell, coils and rods for monitoring mechanical strain and calculating coil stresses during the magnet construction and testing. Each gauge consists of active and temperature-compensating gauges connected into a full-bridge circuit. Prior to the test we lost only one SG in coil #6 (SG061T). SG data were continuously monitored during the mechanical work before the test at Fermilab using the portable SG readout system provided by the LBNL.

In addition to the standard set of the dewar temperature sensors 5 additional resistive temperature devices (RTD) were mounted at top, middle and bottom of the magnet outer skin (*Cernox cx43235*, *cx43233*, *cx50629*, *cx53864* and *cx53825* sensors respectively), and were insulated from the surrounding gas to provide a better indication of the cold mass temperature during cool down and warm up.

The magnetic measurement warm bore was instrumented with a quench antenna for localization of quenches. We used two different quench antennas during this test. The “KEK/HGO” quench antenna consists of three stationary coil segments each 35 cm long and separated by 10.5 cm long couplings. Each coil is made with four windings that are sensitive to normal and skew sextupole and octupole magnetic flux changes, at a radius of 23 mm. The total length of the “KEK” quench antenna is about 120 cm and is not enough to cover even half of the magnet; when installed, it was roughly centered in the LQS01b.

Another experimental quench antenna was built using 12 pc-board (PCB) circuits, each 4-cm long. These boards, 3 per coil, were mounted on a Styrofoam bar with a rectangular cross-section at the end of magnet, distributed evenly with 30 cm spacing. As the warm bore tube extended only ~2 m into the magnet bore, these PCB probes were actually installed in the magnet bore and were operating in liquid helium. More details on location of PCB circuits are presented in Section 7.

Both the VME- and FPGA-based quench detection systems were used in this test. Quench detection thresholds were obtained from the voltage spike data analysis of LQS01a. Current dependent thresholds were used for half-coil signals in both systems (see Attachment II). The 1<sup>st</sup> half-coil signal is formed by coils #8 and #7, and the 2<sup>nd</sup> half-coil signal - by coils #6 and #9.

Only few modifications were performed at VMTF in preparation for the LQS01b test. The passive ground fault detection system was changed into an “active” system by implementing a 5 V circuit connected in series with the ground current limiting resistor. In addition, symmetric grounding was implemented for the protection heaters. These modifications, briefly described below, were fully validated in a test using TQM04, a TQ coil in the Fermilab mirror magnet structure.

### 3.1 Active Ground Fault Detection System

The purpose of a ground fault detection system is to detect ground current associated with an electrical fault of a magnet coil to ground and initiate a slow ramp down to minimize the inductive voltage across the coil and therefore minimize the fault current. Old “passive” ground fault detection system was able to detect a fault only during the current ramps and could not detect coil-to-heater shorts.

In order to lower the risk of testing magnets associated with potential faults to ground an active ground fault detection system was implemented at VMTF. The 5V circuit, which changes the passive system into an active system, is inserted into the grounding path of the 30-kA power supply bus (see Fig. 4). The active ground fault detection circuit design is simple and robust, it uses passive components, diodes, and solid state relays. A continuous ground path exists through the 5V supply via an internal resistor so if the voltage source fails it behaves as the original passive ground fault detection system.

Active ground fault detection system allows detection of coil to ground fault at any ramp rate, magnet inductance or current.

Due to high frequency noise from the active components, the ground fault detection threshold had to be higher than 200 mV and lower than 400 mV based on simulation results. A 350 mV threshold was recommended compared to 150 mV for a passive symmetric grounding.

### 3.2 Symmetric heater grounding

After symmetric grounding of the 30 kA power supply bus at VMTF proved its functionality and reliability, it was decided to implement a symmetric heater grounding as well. Prior to this, heater ground was floating with respect to coils. The magnet protection heater power supplies (HFUs) were tied to ground using a symmetric grounding configuration shown in Fig. 4. Two 1 k $\Omega$  resistors and 100  $\Omega$  ground fault current limiting resistor were used to build the symmetric heater grounding. When there is no fault, it is an independent circuit from the coil active grounding system and has no active components for HFU grounding. But an active ground fault detection system for the magnet coupled with a grounding of the protection heaters allows detection of fault between the coil and heaters.

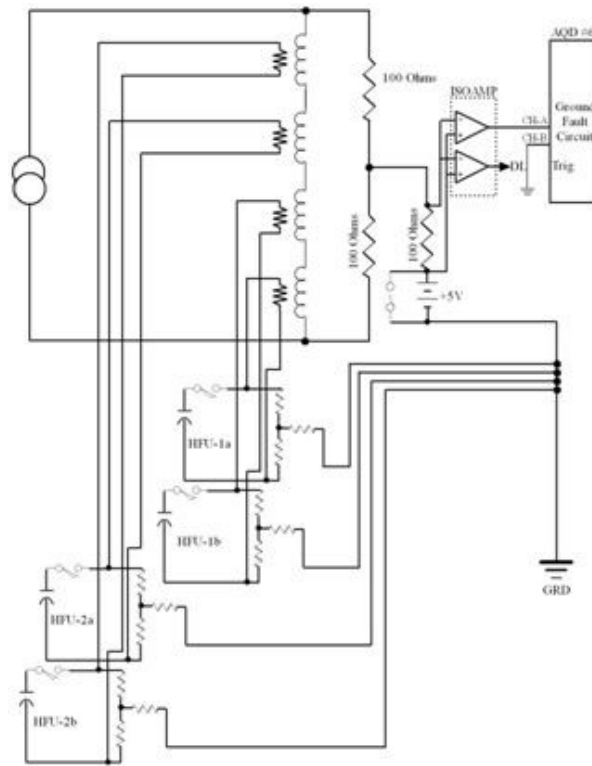


Fig. 4. The magnet coil and protection heater grounding at VMTF

The HFU circuit was also modified in order to preserve the capability to detect an open load. The load status (LS) detection circuit of the original HFU design had a trip threshold of  $\sim 10$  k $\Omega$ . Trip threshold was reduced to  $\sim 2$  k $\Omega$  after modification, so for failure modes in which the magnet protection heaters deteriorate each time they are fired, the more sensitive LS detection circuit will detect it sooner and prevent further testing.

## 4. Quench History

1<sup>st</sup> test cycle (TC1) started with quench training at 4.5 K. For the quench training we were using following ramp rates: 200 A/s up to 3000 A, then 50 A/s up to 5000 A, 20 A/s up to 9000 A and 10 A/s until the quench. This ramping profile is based on our past experience of testing magnets with large voltage spikes. The same ramp rates were used in LQS01a test.

Quench training at 4.5 K started with a quench at 193 T/m (10.7 kA) and already in the second quench it reached 209 T/m exceeding the target field gradient of 200 T/m. In four quenches the magnet reached 220 T/m (12.45 kA). In order to reduce liquid helium consumption, training was continued at 3 K. The magnet performance at 3 K was slightly erratic with quench currents varying from 12.5 kA to 12.8 kA (220-225 T/m), and with a set back at 196 T/m. LQS01b quench history in TC1 is presented in Fig. 5

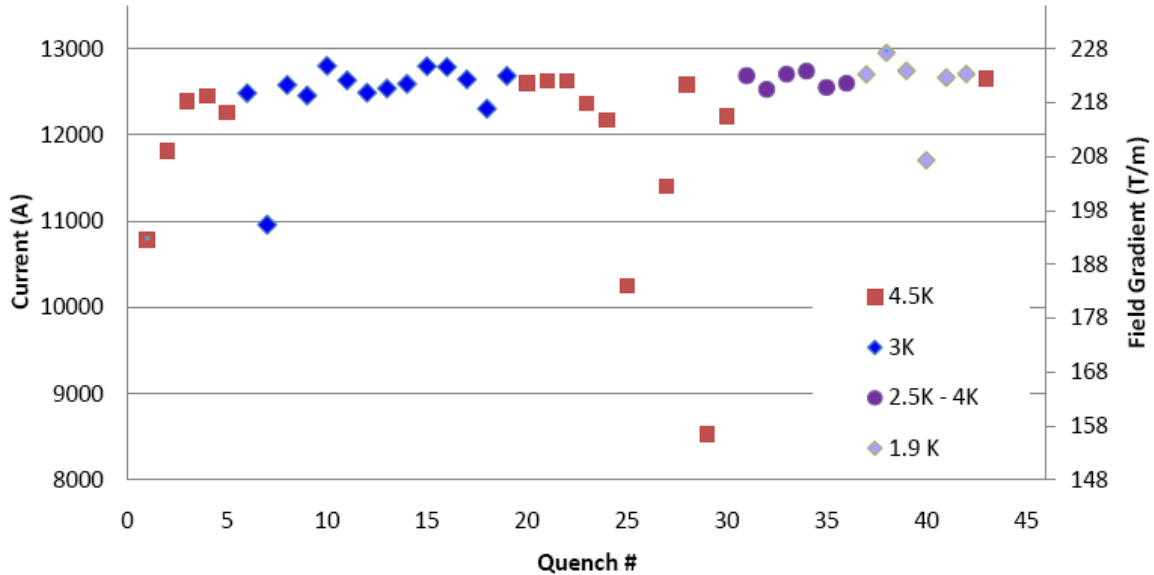


Fig. 5. LQS01b quench history in TC1.

Coils #6, #7 and #8 participated in the training at 4.5 K. All training quenches at 4.5 K started in the pole turn of the inner layer with the only exception being the third quench that started in a multi-turn segment of the outer layer of coil #8. At 3 K the first quenches occurred in the pole turn of the inner layer of coil #6, #8 (set back quench) and #9; and most of the following quenches occurred in the same segment of coil #6 (inner layer, pole turn, central segment **A11-A12**). LQS01b quench history with quench locations in TC1 is shown in Fig. 6.

After training at 3 K, LQS01b showed a plateau of 222 T/m (12.63 kA) at 4.5 K with all quenches starting in the straight section of coil #8 outer layer pole turn (**B4-B5**). Toward the end of the test LQS01b reached 227.5 T/m (12.95 kA) in the second quench at 1.9 K. However it also showed another set-back at 208 T/m.

First 1.9 K quench developed in coil #6 inner layer pole turn, while all others at this

temperature started in coil #9 from different segments (pole turn of inner or outer layer, or inner layer multi-turn mid-plane block).

Last quench in TC1 at 4.5 K was consistent with the previously reached plateau at 222 T/m (12.6 kA).

After 1<sup>st</sup> test cycle LQS01b was warmed up to room temperature so that the lowest temperature of the magnet was above 270 K and then was cooled down again to 4.5 K. Both warm-up and cool down were performed with the same requirement on the temperature gradient - difference between top and bottom of the magnet should not exceed 100 K.

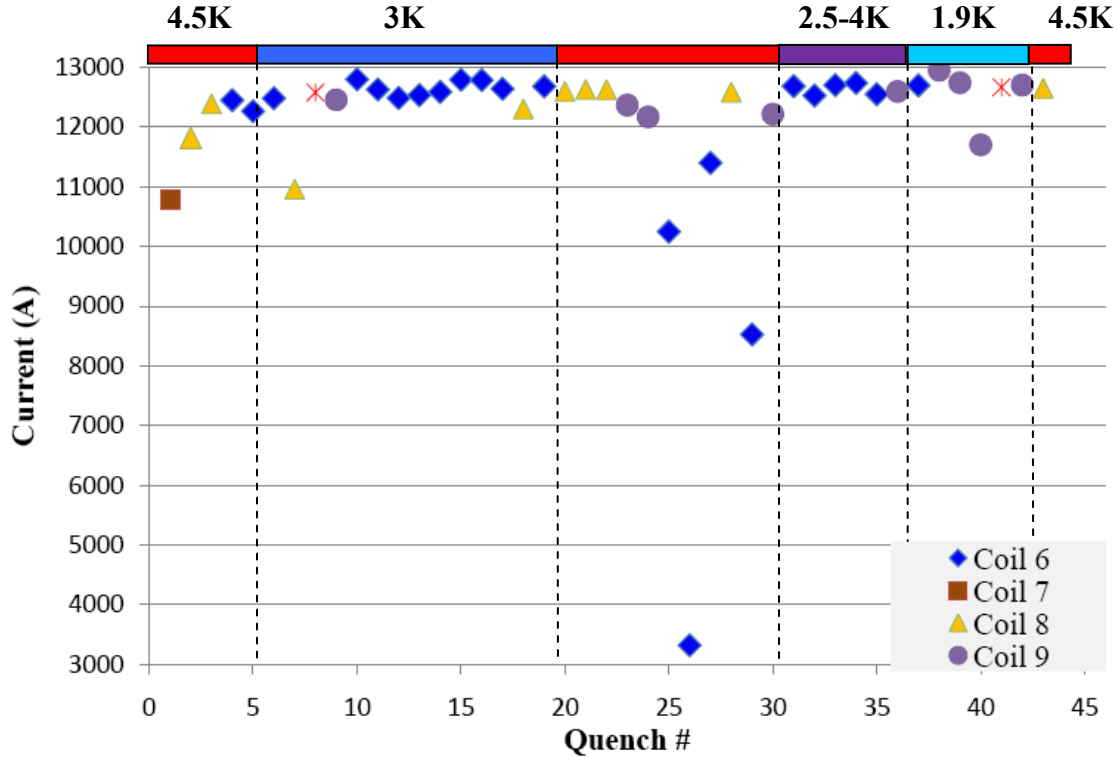


Fig. 6. LQS01b quench history in first TC with quench locations. Colored bars are used to indicate test temperature. Data were lost for quenches # 8 and #41.

LQS01b showed good training memory after thermal cycle and practically in the second ramp the magnet reached quench plateau at 4.5 K. Training quenches at 4.5 K in TC1 and TC2 are compared in Fig. 7. The full quench history is presented in Tables 1 and 2.

Room temperature magnetic measurements were done before (June 22<sup>nd</sup>) and after (September 9<sup>th</sup>) the cold test. A series of field quality measurements were performed at 4.5 K with 82-cm (July 8, 12 and 20) and 10-cm (July 21) tangential probes. In addition, magnetic measurements at 4.5 K were also done using the circuit-board based probes of 10- and 25-cm length (July 23 and August 24-25). Results of these measurements are presented in Section 9.

In addition, warm magnetic measurements after the test were performed using the “Ferret” probe. Preliminary data analysis showed acceptable agreement with the results



obtained in measurements with the conventional tangential probes. The new “Ferret” is still under development and results of these measurements are not presented in this report.

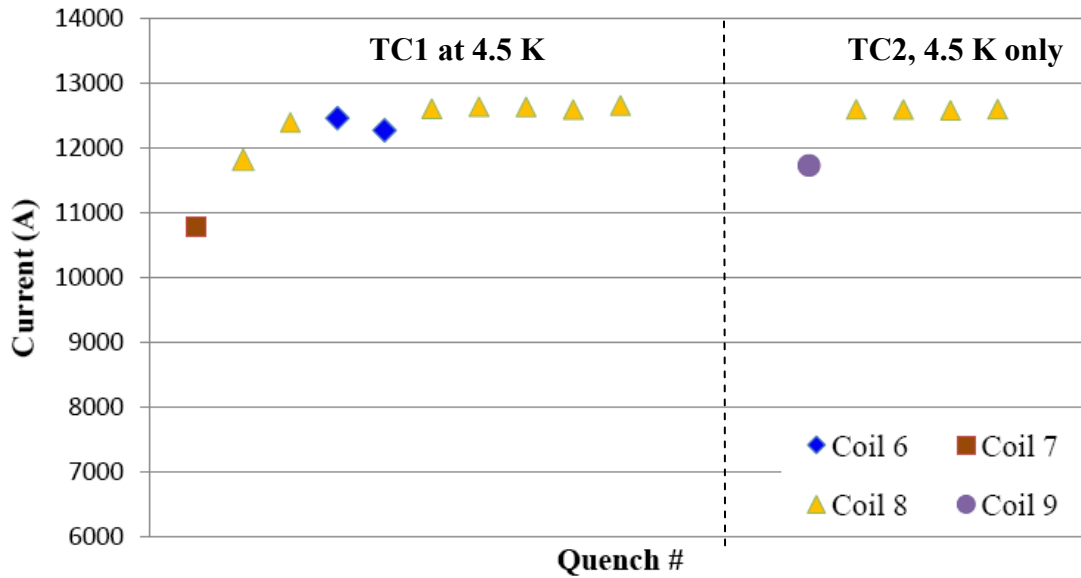


Fig. 7. LQS01b quench training in TC1 and TC2 with quench locations.

Quench multiplicity in all coils is summarized in Fig. 8. 48 quenches were performed in total excluding few trips at low currents and provoked quenches.

For quench localization we mainly used the “KEK” quench antenna, even though it covered only the central portion of the magnet.

We lost data for only two quenches, number 8 and 41. No particular reasons were found for this failure and as a preventive measure we should restart data logger node in every 1-2 weeks.

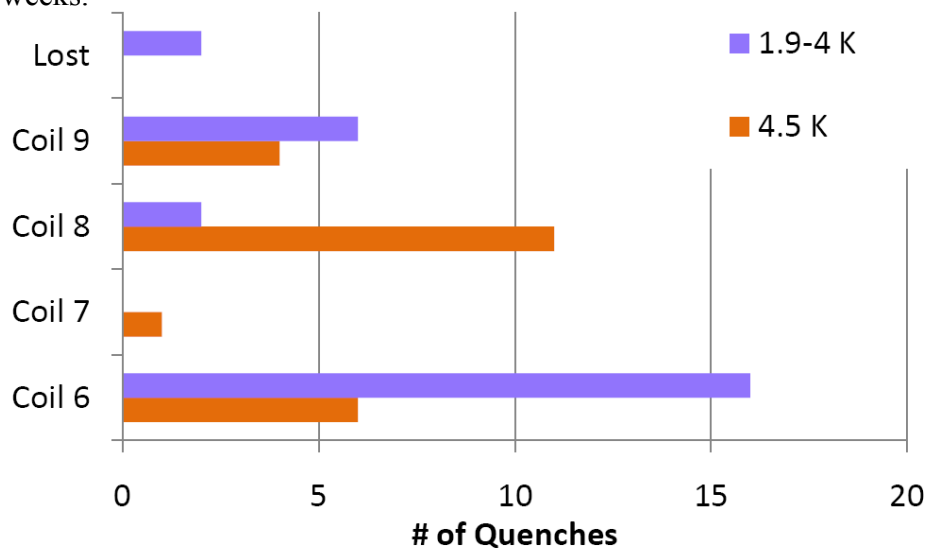


Fig. 8. Quench multiplicity in coils

#### 4.1 Protection heater failure

Protection heater on the inner layer lead end of coil #7 (PH07A01) in LQS01b was damaged after first few quenches at 4.5 K. Magnet protection system did not detect this failure because no short developed between the heater and ground. Heater failure originally was noticed by offline monitoring of the protection heater discharge profile after the quench.

From previous tests we knew that heater discharge (voltage decay) profile is very sensitive to the heater resistance. Usually this profile is steady from quench to quench if nothing happens with the heater and if the HFU bank capacitance and voltage is fixed. But if heater started to deteriorate one can easily see a change in profile.

As a reference plot we used the HFU voltage decay plot after the first training quench when HFU parameters were fixed. Then after each quench the heater discharge plot was compared bin-by-bin with the reference plot.

Differences between the heater discharge profiles before and after the incident with PH07A01 are shown in Fig. 9. Very sharp and narrow spike on the order of 4-5 V at  $t=0$  (see Fig. 9, left) can be explained with a small spike in the HFU voltage signal at the moment of its discharge. Much larger difference for a longer time period, exceeding the decay time of  $\sim 30$  ms, was observed after the incident (see Fig. 9, right).

Reference heater discharge plot was updated if the HFU parameters or other test conditions were changed (test temperature for example).

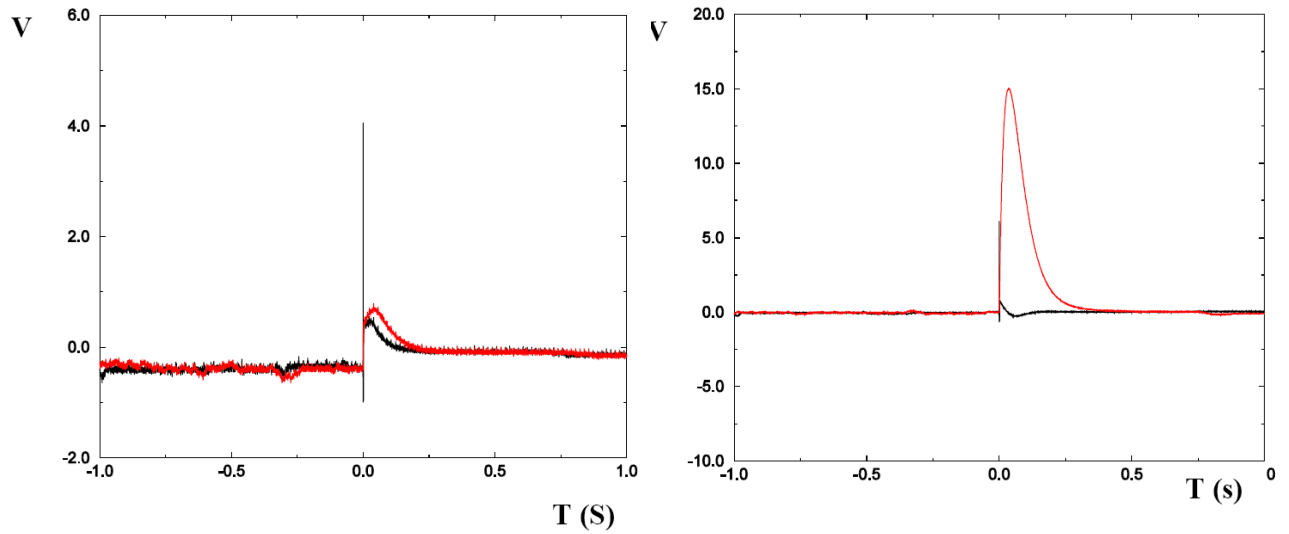


Fig. 9. Differences in protection heater discharge profile before (left) and after (right) the incident with PH07A01. Red and Black plots represent two different HFU.

## 5. Ramp Rate Dependence

Ramp rate dependence study was performed at 4.5 K after the quench training at 3 K. Summarizing plot both for LQS01a and LQS01b magnets is shown in Fig. 10.

Quenches at a high ramp rates in LQS01b developed in the mid-plane segments of coil #6 (125 – 200 A/s) or coil #9 (50 - 100 A/s). In LQS01a quenches at ramp rates up to 100 A/s still originated from the pole-turn segments of coil #7.

Low ramp rate quenches (10 A/s and 20 A/s) in LQS01b were located in the pole-turn segments of coil #8.

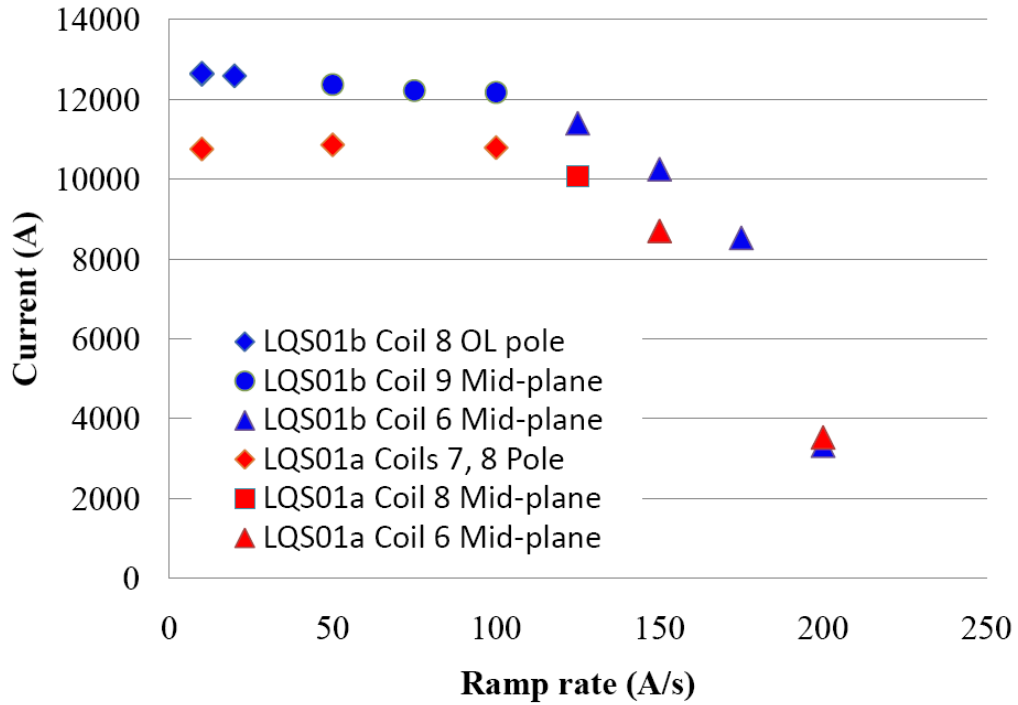


Fig. 10. Ramp rate dependence study at 4.5 K.

**Table 1: LQS01b Quench History with comments**

File	#	I (A)	dI/dt (A/sec)	t <sub>quench</sub> (sec)	MITs (10 <sup>6</sup> A <sup>2</sup> sec)	T (K) Mag. Bottom	T (K) Mag. Top	Comments (from file)
1st Thermal cycle								
lqs01b.Quench.100701171803.664		1011	0	0.0003	0.15	4.5844	4.5821	DQD coil manual trip at 1kA, 150A/s, 4.6K
lqs01b.Quench.100701182228.266		3008	0	-0.3043	3.88	4.5937	4.593	HFU1 testing 350V, 19.2mF, HFU2 protection, T=4.6K
lqs01b.Quench.100701184950.756		3005	0	-0.0155	1.29	4.5877	4.591	HFU2 testing at 330V, 19.2mF, HFU1 protection 350V, 19.2mF, 3kA
lqs01b.Quench.100701192317.411	1	10783	10	-0.0132	6.1	4.601	4.6019	quench at 10.8kA, 10A/s, 4.6K37
lqs01b.Quench.100702132040.726	2	11817	10	-0.0112	6.16	4.5878	4.5866	quench at 11.8 kA, 10A/s, 4.6K
lqs01b.Quench.100702155725.885	3	12390	10	-0.0046	5.33	4.5375	4.5377	quench at 12.4 kA, 10A/s, 4.5K
lqs01b.Quench.100702173828.982	4	12450	10	-0.0029	5.05	4.5419	4.548	quench at 12.44kA, 10A/s, 4.5K
lqs01b.Quench.100706111139.252	5	12265	10	-0.0032	5.09	4.6245	4.6161	quench at 12.2kA, 10A/s, 4.6K
lqs01b.Quench.100706143411.872	-	3149	50	-0.0127	1.37	2.9838	3.024	Trip at 3kA, 50A/s, 3K
lqs01b.Quench.100706145001.138	6	12484	10	-0.0028	5.26	2.9615	3.0119	quench at 12.5kA, 10A/s, 3K
lqs01b.Quench.100706174001.714	7	10959	10	-0.0080	5.73	2.9582	3.0552	quench at 11kA, 10A/s, 3K
lqs01b.Quench.100706192958.147	8	12580	10					LOST DATA
lqs01b.Quench.100707115337.655	9	12456	10	-0.0077	6.04	2.8325	2.8918	quench at 12.5kA, 10A/s, 3K
lqs01b.Quench.100707142035.181	10	12799	10	-0.0036	5.42	3.0125	3.1391	quench at 12.8 kA, 10 A/s, 3K
lqs01b.Quench.100713100328.285	11	12631	10	-0.0022	5.19	2.914	3.0028	quench at 12.6kA, 10 A/s, 3K
lqs01b.Quench.100713115749.326	12	12489	10	-0.0034	5.35	3.050	3.1485	quench at 12.5kA, 10A/s, 3K
lqs01b.Quench.100713141614.164	-	1305	200	-0.0143	0.26	3.011	3.0616	Trip at 1.3 kA, 200 A/s, 3K
lqs01b.Quench.100713143514.875	13	12536	10	-0.0160	7.34	3.022	3.1077	quench at 12.5 kA, 10A/s, 3K
lqs01b.Quench.100713165150.989	14	12593	10	-0.0041	5.49	2.855	2.9528	quench at 12.6kA, 10 A/s, 3K
lqs01b.Quench.100713181329.249	-	1396	200	-0.0155	0.39	2.913	3.0057	quench at 1400A, 10A/s, 3K (spike induced)
lqs01b.Quench.100713182143.427	15	12794	50	-0.0041	5.43	2.907	2.9764	quench at 12.8 kA, 50 A/s, 3K
lqs01b.Quench.100714093431.589	-	1260	200	-0.0600	0.5	2.939	2.9986	quench at 1292, 200 A/s, 3K (spike induced)
lqs01b.Quench.100714094749.729	16	12784	50	-0.0050	5.01	2.993	3.1219	quench at 12.8 kA, 50 A/s (200A/s up to 3kA), 3K
lqs01b.Quench.100714113433.052	17	12643	50	-0.0020	5.1	2.986	3.0842	quench at 12.6 kA, 50 A/s, 3K
lqs01b.Quench.100714134144.706	-	1365	200	-0.0526	0.36	2.987	3.0514	Spike trip at 1.3kA, 200 A/s, 3K
lqs01b.Quench.100714134846.461	18	12297	100	-0.0566	-	3.029	3.156	quench at 12.4 kA, 100 A/s, 3K

lqs01b.Quench.100715094651.829	19	12684	20	-0.0027	5.26	2.966	3.0624	quench at 12.7kA, 20A/s, 3K
lqs01b.Quench.100715111525.668	20	12602	10	-0.0035	5.2	4.552	4.5591	quench at 12.6kA, 10A/s, 4.5K
lqs01b.Quench.100715134010.141	21	12632	10	-0.0036	5.22	4.546	4.5502	quench at 12.6 kA, 10A/s, 4.5K544E-03
lqs01b.Quench.100715145900.575	22	12629	10	-0.0035	5.17	4.533	4.5359	quench at 12.6kA, 10A/s, 4.5K
lqs01b.Quench.100721170326.135	23	12370	50	-0.0025	4.97	4.600	4.6021	quench at 12.4 kA, 50 A/s, 4.5K
lqs01b.Quench.100722094047.765	24	12174	100	-0.0043	5.1	4.513	4.5273	quench at 12.1kA, 100A/s, 4.5K
lqs01b.Quench.100722111211.782	25	10249	150	-0.0017	4.5	4.521	4.5384	quench at 10.2kA, 150 A/s, 4.5K
lqs01b.Quench.100722122947.831	26	3209	200	-0.0300	-	4.509	4.517	quench at 3.3kA, 200 A/s, 4.5K
lqs01b.Quench.100722123849.273	27	11404	125	-0.0024	4.74	4.542	4.558	quench at 11.4kA, 125 A/s, 4.5K
lqs01b.Quench.100722145513.918		6164	50	0.0004	3.52	4.490	4.499	Trip at 6 kA, AQD leads detected trip, 4.5K
lqs01b.Quench.100722151540.869	28	12589	20	-0.0036	5.26	4.532	4.569	quench at 12.6kA, 20A/s, 4.5K
lqs01b.Quench.100722164824.864	29	8528	175	-0.0024	4.25	4.531	4.543	quench at 8.5kA, 175 A/s, 4.5K
lqs01b.Quench.100722173901.154	30	12185	75	-0.0045	<6.27	4.536	4.612	quench at 12.2kA, 75 A/s, 4.5K
lqs01b.Quench.100727160924.701	31	12688	10	-0.0024	5.2	4.070	4.070	quench at 12.6 kA, 10A/s, 4K
lqs01b.Quench.100727181939.638	32	12528	50	-0.0042	5.4	4.010	4.010	quench at 12.4kA, 50 A/s, 4.0K
lqs01b.Quench.100727203922.181	33	12702	10	-0.0028	5.33	3.600	3.600	quench at 12.7kA, 10A/s, 3.6K
lqs01b.Quench.100728112945.464	34	12739	50	-0.0400	-	3.481	3.5632	quench at 12.7 kA, 50 A/s, 3.5K
lqs01b.Quench.100728144436.404	35	12552	10	-0.0017	5.2	2.528	2.6655	quench at 12.5 kA, 10A/s, 2.5K
lqs01b.Quench.100728170114.693	36	12599	50	-0.0078	6.14	2.491	2.6483	quench at 12.6kA, 50 A/s, 2.5K
lqs01b.Quench.100729102205.273	37	12704	10	-0.0032	5.54	1.923	1.9309	quench at 12.7 kA, 10A/s, 1.9K
lqs01b.Quench.100729131844.559	38	12952	10	-0.0059	6.03	1.923	1.9174	quench at 12.9kA, 10A/s, 1.9K
lqs01b.Quench.100730092512.668	39	12744	10	-0.0055	5.92	1.923	1.9193	quench at 12.7 kA, 10A/s, 1.9K
lqs01b.Quench.100730114246.473	40	11703	10	-0.0090	6.16	1.933	1.9286	quench at 11.7kA, 10 A/s, 1.9K
lqs01b.Quench.100731091606.655	41	12665	10					LOST DATA
lqs01b.Quench.100731115740.338	42	12705	50	-0.0025	5.64	1.912	1.9292	quench at 12.6kA, 50 A/s, 1.9K
lqs01b.Quench.100731132209.841	43	12651	10	-0.0055	5.33	4.545	4.5575	quench at 12.6 kA, 10 A/s, 4.5K
2nd Thermal cycle								
lqs01b.Quench.100818172321.023	44	11728	10	-0.0048	5.05	4.632	4.6294	10 A/s above 10kA, 11720 A quench detected by AQD coil.
lqs01b.Quench.100823122648.494	45	12592	10	-0.0038	5.3	4.598	4.6023	10 A/s ramp rate.
lqs01b.Quench.100823144616.555	46	12589	10	-0.0038	5.3	4.600	4.5987	10 A/s ramp to quench.
lqs01b.Quench.100824094757.691	47	12577	10	-0.0035	5.24	4.617	4.6153	10 A/s ramp rate.
lqs01b.Quench.100826102425.760	48	12593	20	-0.0057	0.17	4.522	4.5142	ramped up for magnetic measurements a little too soon - LL was only at 15 cm, and a quench was detected.

**Table 2: LQS01b Quench History with parameters for the first two quenching segments**

File	#	I (A)	dI/dt (A/sec)	t <sub>quench</sub> (sec)	QDC	1 <sup>st</sup> Vtap seg	t <sub>rise</sub> (sec)	2 <sup>nd</sup> Vtap seg	t <sub>rise</sub>	T (K) Magn.
1st Thermal cycle										
lqs01b.Quench.100701171803.664		1011	0	0.0003	HcoilHcoil					4.583
lqs01b.Quench.100701182228.266		3008	0	-0.3043	HcoilHcoil	7a3_7a2	-0.1367	7a2_7a1	-0.1350	4.593
lqs01b.Quench.100701184950.756		3005	0	-0.0155	HcoilHcoil	9a8_9a7	-0.0158	6b2_6b1	-0.0157	4.589
lqs01b.Quench.100701192317.411	1	10783	10	-0.0132	HcoilHcoil	7a8_7a7	-0.0120	7a5_7a4	-0.0055	4.601
lqs01b.Quench.100702132040.726	2	11817	10	-0.0112	HcoilHcoil	8a7_8a8	-0.0071	8a6_8a7	-0.0057	4.587
lqs01b.Quench.100702155725.885	3	12390	10	-0.0046	HcoilHcoil	8b4_8b3	-0.0072	8b3_8b2	-0.0072	4.538
lqs01b.Quench.100702173828.982	4	12450	10	-0.0029	HcoilHcoil	6a11_6a12	-0.0048	6a4_6a5	-0.0003	4.545
lqs01b.Quench.100706111139.252	5	12265	10	-0.0032	HcoilHcoil	6a11_6a12	-0.0049	6a4_6a5	-0.0020	4.620
lqs01b.Quench.100706143411.872	-	3149	50	-0.0127	HcoilHcoil	7a11_7a10	-0.0132	7b5_7b6	-0.0130	3.004
lqs01b.Quench.100706145001.138	6	12484	10	-0.0028	HcoilHcoil	6a11_6a12	-0.0041	6a4_6a5	-0.0017	2.987
lqs01b.Quench.100706174001.714	7	10959	10	-0.0080	HcoilHcoil	8a7_8a8	-0.0097	8a4_8a5	-0.0045	3.007
lqs01b.Quench.100706192958.147	8	12580	10							
lqs01b.Quench.100707115337.655	9	12456	10	-0.0077	HcoilHcoil	9a8_9a7	-0.0114	6b4_6b3	-0.0060	2.862
lqs01b.Quench.100707142035.181	10	12799	10	-0.0036	HcoilHcoil	6a11_6a12	-0.0052	9a8_9a7	-0.0034	3.076
lqs01b.Quench.100713100328.285	11	12631	10	-0.0022	HcoilHcoil	6a11_6a12	-0.0039	6a4_6a5	-0.0031	2.958
lqs01b.Quench.100713115749.326	12	12489	10	-0.0034	HcoilHcoil	6a11_6a12	-0.0055	6a4_6a5	-0.0001	3.099
lqs01b.Quench.100713141614.164	-	1305	200	-0.0143	HcoilHcoil	6b4_6b3	-0.0172	6a2_6a3	-0.0154	3.036
lqs01b.Quench.100713143514.875	13	12536	10	-0.0160	HcoilHcoil	6a11_6a12	-0.0056	6a4_6a5	-0.0003	3.065
lqs01b.Quench.100713165150.989	14	12593	10	-0.0041	HcoilHcoil	6a11_6a12	-0.0053	6a4_6a5	-0.0003	2.904
lqs01b.Quench.100713181329.249	-	1396	200	-0.0155	HcoilHcoil	6b4_6b3	-0.0155	6a11_6a12	-0.0153	2.959
lqs01b.Quench.100713182143.427	15	12794	50	-0.0041	HcoilHcoil	6a11_6a12	-0.0048	6a4_6a5	-0.0001	2.942
lqs01b.Quench.100714093431.589	-	1260	200	-0.0600	HcoilHcoil	6a11_6a12	-0.0598	6a1_6a2	-0.0596	2.969
lqs01b.Quench.100714094749.729	16	12784	50	-0.0050	HcoilHcoil	6a11_6a12	-0.0042	6a4_6a5	-0.0011	3.057
lqs01b.Quench.100714113433.052	17	12643	50	-0.0020	HcoilHcoil	6a11_6a12	-0.0039	6a4_6a6	-0.0013	3.035
lqs01b.Quench.100714134144.706	-	1365	200	-0.0526	WcoilIdot	6b5_6b4	-0.0462	6a11_6a12	-0.0216	3.019

lqs01b.Quench.100714134846.461	18	12297	100	-0.0566	HcoilHcoil	8b2_8b3	-0.0023	8a2_8a3	-0.0023	3.092
lqs01b.Quench.100715094651.829	19	12684	20	-0.0027	HcoilHcoil	6a11_6a12	-0.0041	6a4_6a5	-0.0025	3.014
lqs01b.Quench.100715111525.668	20	12602	10	-0.0035	HcoilHcoil	8b5_8b4	-0.0056	8b4_8b3	-0.0052	4.555
lqs01b.Quench.100715134010.141	21	12632	10	-0.0036	HcoilHcoil	8b5_8b4	-0.0053	8b6_8b5	-0.0049	4.548
lqs01b.Quench.100715145900.575	22	12629	10	-0.0035	HcoilHcoil	8b5_8b4	-0.0053	8b4_8b3	-0.0042	4.534
lqs01b.Quench.100721170326.135	23	12370	50	-0.0025	HcoilHcoil	9a3_9a2	-0.0044	9b2_9b3	-0.0021	4.601
lqs01b.Quench.100722094047.765	24	12174	100	-0.0043	HcoilHcoil	9a3_9a2	-0.007	9a2_9a1	-0.0064	4.520
lqs01b.Quench.100722111211.782	25	10249	150	-0.0017	HcoilHcoil	6a2_6a3	-0.0033	6b3_6b2	-0.0028	4.530
lqs01b.Quench.100722122947.831	26	3209	200	-0.0300	HcoilHcoil	6a2_6a3	-0.0295	6b3_6b2	-0.0291	4.513
lqs01b.Quench.100722123849.273	27	11404	125	-0.0024	HcoilHcoil	6a2_6a3	-0.0028	6b3_6b2	-0.0028	4.550
lqs01b.Quench.100722145513.918		6164	50	0.0004	WcoilGnd	9b1b_9b2b	-0.0003	6a2_6a3	-0.0001	4.495
lqs01b.Quench.100722151540.869	28	12589	20	-0.0036	HcoilHcoil	8b5_8b4	-0.005	8b4_8b3	-0.0036	4.550
lqs01b.Quench.100722164824.864	29	8528	175	-0.0024	HcoilHcoil	6a2_6a3	-0.0036	6b3_6b2	-0.0030	4.537
lqs01b.Quench.100722173901.154	30	12185	75	-0.0045	HcoilHcoil	9a3_9a2	-0.0044	9b2_9b3	-0.0035	4.574
lqs01b.Quench.100727160924.701	31	12688	10	-0.0024	HcoilHcoil	6a11_6a12	-0.0036	6a4_6a5	-0.0025	4.070
lqs01b.Quench.100727181939.638	32	12528	50	-0.0042	HcoilHcoil	6a11_6a12	-0.0042	6a4_6a5	-0.0025	4.010
lqs01b.Quench.100727203922.181	33	12702	10	-0.0028	HcoilHcoil	6a11_6a12	-0.0041	6a4_6a5	-0.0025	3.600
lqs01b.Quench.100728112945.464	34	12739	50	-0.0400	HcoilHcoil	6a11_6a12	-0.0039	6a4_6a5	-0.0001	3.522
lqs01b.Quench.100728144436.404	35	12552	10	-0.0017	HcoilHcoil	6a2_6a3	-0.0031	6b3_6b2	-0.0020	2.597
lqs01b.Quench.100728170114.693	36	12599	50	-0.0078	HcoilHcoil	9b4_9b5	-0.0078	9b3_9b4	-0.0001	2.570
lqs01b.Quench.100729102205.273	37	12704	10	-0.0032	HcoilHcoil	6a11_6a12	-0.0052	6a4_6a5	-0.0034	1.927
lqs01b.Quench.100729131844.559	38	12952	10	-0.0059	HcoilHcoil	9b4_9b5	-0.0075	9b3_9b4	-0.0021	1.920
lqs01b.Quench.100730092512.668	39	12744	10	-0.0055	HcoilHcoil	9b4_9b5	-0.0082	9b3_9b4	-0.0023	1.921
lqs01b.Quench.100730114246.473	40	11703	10	-0.0090	HcoilHcoil	9a3_9a2	-0.0113	9b2_9b3	-0.0110	1.931
lqs01b.Quench.100731091606.655	41	12665	10							
lqs01b.Quench.100731115740.338	42	12705	50	-0.0025	HcoilHcoil	9a8_9a6	-0.0042	9a5_9a4	-0.0015	1.921
lqs01b.Quench.100731132209.841	43	12651	10	-0.0055	HcoilHcoil	8b5_8b4	-0.0055	8b4_8b3	-0.0051	4.551
2nd Thermal cycle										
lqs01b.Quench.100818172321.023	44	11728	10	-0.0048	HcoilHcoil	9a13_9a12	-0.0048	9a5_9a4	-0.0025	4.631
lqs01b.Quench.100823122648.494	45	12592	10	-0.0038	HcoilHcoil	8b5_8b4	-0.0043	8b4_8b3	-0.0027	4.600
lqs01b.Quench.100823144616.555	46	12589	10	-0.0038	HcoilHcoil	8b5_8b4	-0.0042	8b4_8b3	-0.0025	4.599
lqs01b.Quench.100824094757.691	47	12577	10	-0.0035	HcoilHcoil	8b5_8b4	-0.0048	8b4_8b3	-0.0031	4.616
lqs01b.Quench.100826102425.760	48	12593	20	-0.0057	WcoilIdot	8b5_8b4	-0.0057	8b4_8b3	-0.0056	4.518

## 6. Temperature Dependence

Temperature dependence study was performed at ramp rates of 10 A/s and 50 A/s. Maximum quench currents at each temperature are shown in Fig. 11. The shallow slope of the temperature dependence, the large variations of the quench current and the temperature-dependent location of the quenches at temperatures 3 K and below, show that the limited stability of the conductor affected LQS01b performance below 4.5 K.

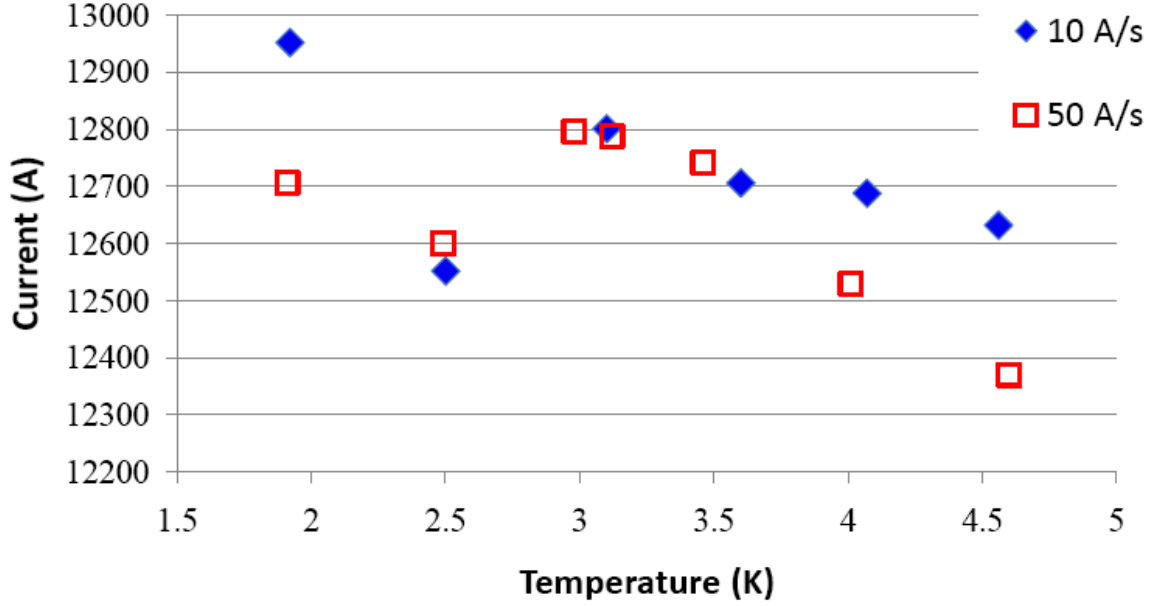


Fig. 11 Quench current temperature dependence

Temperature dependence was also investigated for the plateau quenches at 4.5 K. RTD readings from the fast-scribe data scanners were used for the best temperature estimates. Temperature dependence for 4.5 K plateau quenches at 10 A/s ramp rate is shown in Fig. 12. Temperatures shown on the plot are obtained after averaging magnet top and bottom temperatures. Slope of  $\sim 700$  A/K estimated from the linear fit to data is consistent with  $\Delta I/\Delta T \sim 850$  A/K computed from the model.

## 7. Quench Locations

Voltage drop measurements across the voltage tap segments at 300 K were used to check the length of these segments. The segments and their lengths are listed in Table 3.

Most training quenches developed in the straight sections of the inner and outer layer pole-turn segments **A7-A8**, **A11-A12** and **B4-B5**. These segments are about 200 cm long and in most quenches no longitudinal quench propagation to adjacent segments was observed. As a consequence we cannot locate precisely the origin of these quenches using voltage tap information. Location of all training quenches is shown in Fig. 13. Quenches at ramp rates 50 A/s and more, not shown in this figure, developed in the mid-plane blocks of the inner or outer coil layers.

For further localization of quenches we used the quench antenna instrumented in the warm bore. The “KEK” quench antenna consists of three stationary coils segments each 35 cm long and separated by 10.5 cm long couplings. The probe was positioned in the bore of the magnet so that the second



antenna coil **C2** was about in the middle of magnet, and **C1** towards the Lead End. Quench antenna location in the bore and with respect to the long straight section segments **A7-A8** and **A11-A12** is shown in Fig. 14. All training quenches with available quench antenna information are listed in Table 4 that shows also the time difference between the quench-start signal in the quench antenna (QA) and in the voltage taps. Quench antenna coil **C3** was detecting all quenches in the inner layer pole-turn segment of coil #6 (**A11-A12**) and both **C2** and **C3** almost at the same time were detecting most quenches in the outer layer pole-turn segment of coil #8 (**B4-B5**).

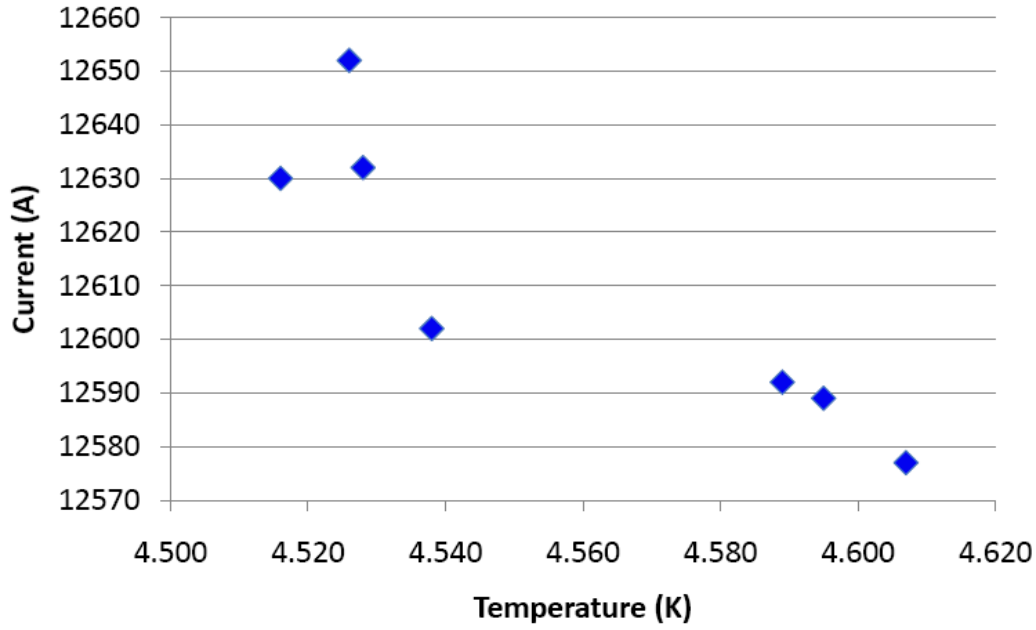


Fig. 12 Temperature dependence of plateau quenches at 4.5 K and a ramp rate of 10 A/s

Table 3. Voltage tap segments in LQS01a/b

Segment	length (cm)	Segment	length (cm)
<b>A1-A2</b>	<b>10.2</b>	<b>A11-A12</b>	<b>204.3</b>
<b>A2-A3</b>	<b>7009.1</b>	<b>A12-A13</b>	<b>30.7</b>
<b>A3-A4</b>	<b>1233.3</b>	<b>A13-B7</b>	<b>32.9</b>
<b>A4-A5</b>	<b>2448.8</b>	<b>B7-B6</b>	<b>283.6</b>
<b>A5-A6</b>	<b>40.8</b>	<b>B6-B5</b>	<b>18.1</b>
<b>A6-A7</b>	<b>30.7</b>	<b>B5-B4</b>	<b>283.6</b>
<b>A7-A8</b>	<b>204.3</b>	<b>B4-B3</b>	<b>3655.6</b>
<b>A8-A9</b>	<b>37.5</b>	<b>B3-B2</b>	<b>5542.8</b>
<b>A9-A10</b>	<b>12.6</b>	<b>B2-B1</b>	<b>10.2</b>
<b>A10-A11</b>	<b>37.5</b>		

We also used circuit-board (PCB) based quench antenna located at the end of the magnet. Location and orientation of PCB quench antennas are shown in Fig. 15. Due to high noise level PCB quench antenna in the above described configuration was not useful for determination of the quench location. Only in few quenches clear signals were detected in PCB (see Table 4).

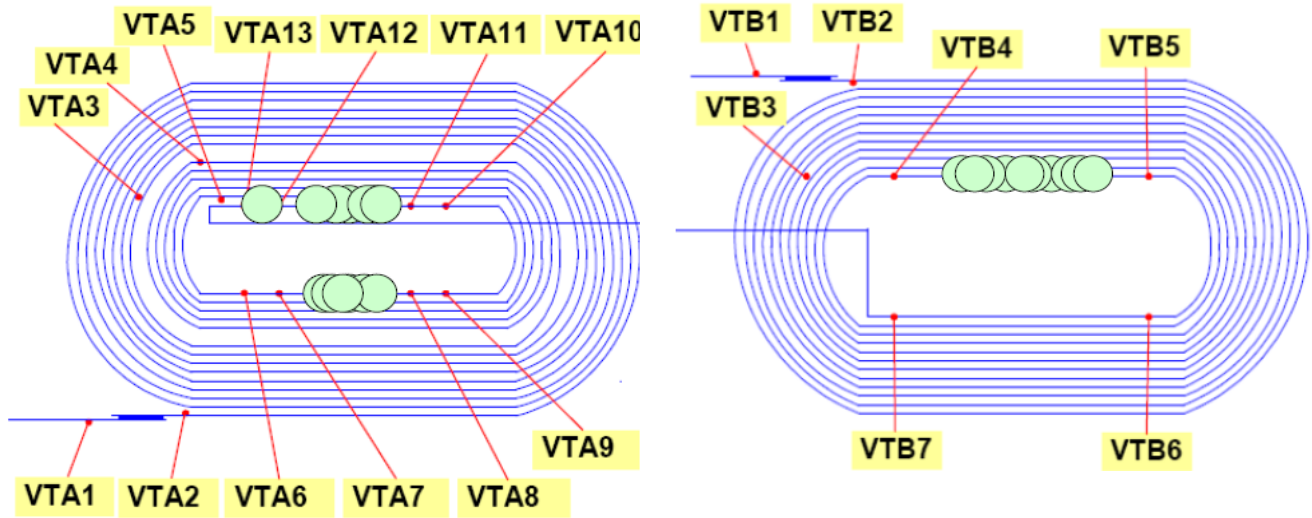


Fig. 13. Location of the training quenches in the inner (left) and outer (right) coils. Quenches in multi-turn segments A2-A3 or B2-B3 are not shown.

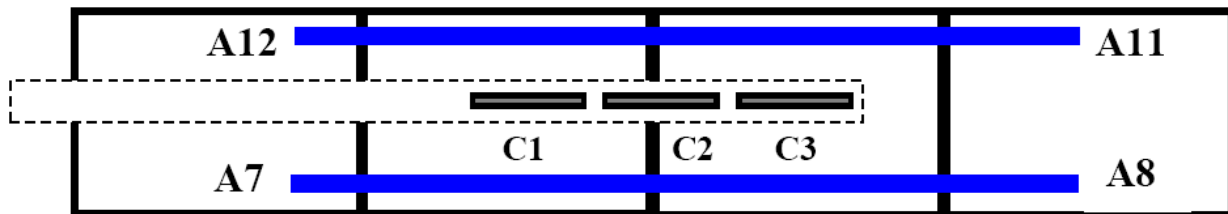


Fig. 14. KEK quench antenna location in the magnetic measurement warm bore.

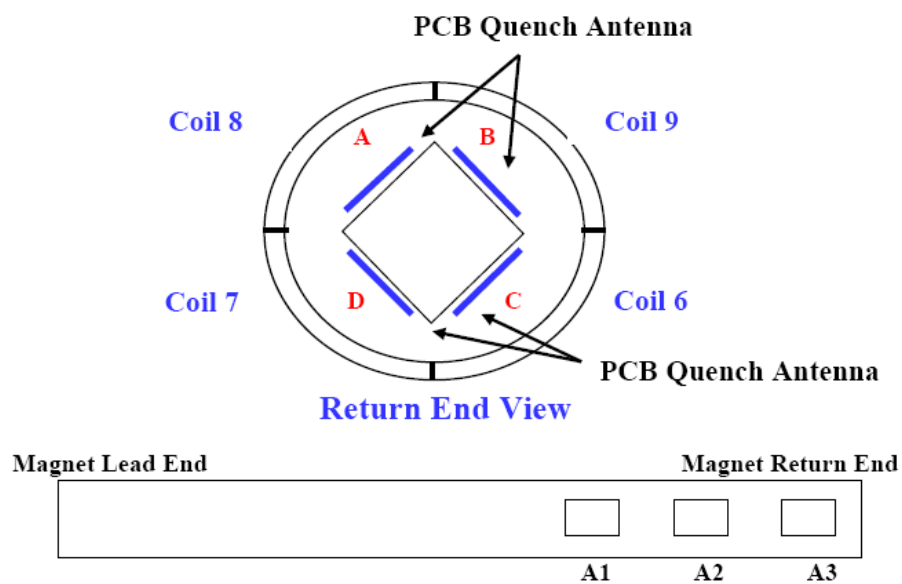


Fig. 15. PCB quench antenna location in the magnetic measurement warm bore.

**Table 4. Quenches with the quench antenna information**

#	I (A)	Ramp Rate	T (K)	Coil	Segment	QA	T(QA), ms	Tq-T(QA), ms
4	12454	10	4.54	6	a11_a12	C3	-5.6	0.2
5	12267	10	4.62	6	a11_a12	C3	-4	-1.6
6	12485	10	3	6	a11_a12	C3	-4.8	0.1
7	10960	10	3	8	a7_a8	C2	-10.2	-0.2
9	12457	10	2.9	9	a8_a7	C1	-6.2	-5.2
16	12788	50	3.12	6	a11_a12	C3	-5	0.3
19	12684	20	3.06	6	a11_a12	C3	-5	0
20	12602	10	4.56	8	b5_b4	C2/C3	-4.3	-1.3
21	12632	10	4.56	8	b5_b4	C2/C3	-5	-0.3
22	12630	10	4.56	8	b5_b4	C2	-4.8	-0.5
23	12370	50	4.60	9	a3_a2	PCB/B1	-4.6	0.2
24	12172	100	4.53	9	a3_a2	PCB/B1	-5.6	-1.4
26	3319	200	4.52	6	a2_a3	PCB/D2	-26.6	-3.1
30	12218	75	4.61	9	a3_a2	PCB/B1	-4.7	0.4
31	12688	10	4.07	6	a11_a12	C3	-4.5	0.1
32	12530	50	4.01	6	a11_a12	C3	-4.2	-0.5
33	12706	10	3.6	6	a11_a12	C3	-4.8	0.1
34	12742	50	3.48	6	a11_a12	C3	-4.5	-0.1
35	12552	10	2.64/2.36	6	a2_a3	C3	-3.2	0.1
36	12600	50	2.62/2.34	9	b4_b5	C3	-9.1	0.6
37	12702	10	1.92	6	a11_a12	C3	-4.2	-1
38	12952	10	1.92	9	b4_b5	C3	-7.9	0.4
39	12743	10	1.92	9	b4_b5	C3	-8.7	0.5
40	11705	10	1.93	9	a3_a2	C3	-10.8	-0.5
42	12706	50	1.91	9	a8_a6	C3	-3.7	-1.4
43	12652	10	4.5	8	b5_b4	C2/C3	-5.8	0.3
44	11726	10	4.6	9	a13_a12	C1	-4.8	0
45	12592	10	4.55	8	b4_b5	C2/C3	-5.9	0.2

## 8. Strain Gauge Data

The LQS01b mechanical behavior during cool-down, test, and warm-up of first and second thermal cycle were monitored with strain gauges mounted on support structure components and coils. The shell was instrumented with half-bridge strain gauges (see Fig. 16) placed on each segment (“S1” to “S4” from the lead end), and distributed on four mid-planes (“T” top, “R” right, “B” bottom, and “L” left). The gauges measured both the azimuthal (“T”) and axial (“Z”) strain and were all thermally compensated by gauges mounted on aluminum elements.

Each of the four LQS01 coils (“C”), coil #6-#7-#8-#9, was instrumented with full bridge azimuthal (“T”) and axial (“Z”) gauges thermally compensated and mounted along four axial locations (“1” to “4” from the lead end) of the inner-layer poles (see Fig. 17).

Each axial rod was equipped with two half-bridge gauges mounted close to the end plate (lead end), in opposite azimuthal locations to compensate for bending effects (see Fig. 18). The total number of gauges mounted on the LQS01 magnet amounts to 56 gauges.

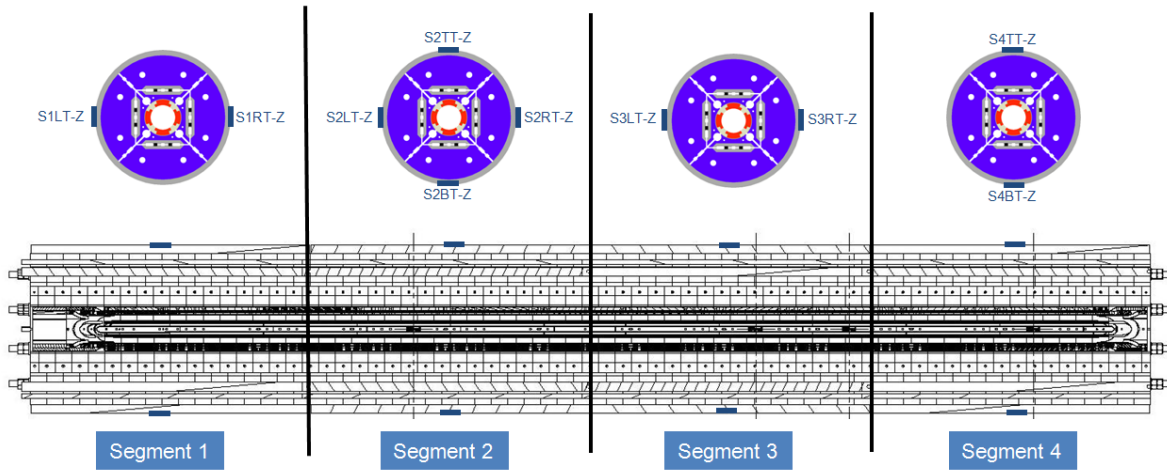


Fig. 16. Locations of the shell strain gauges (blue markers).

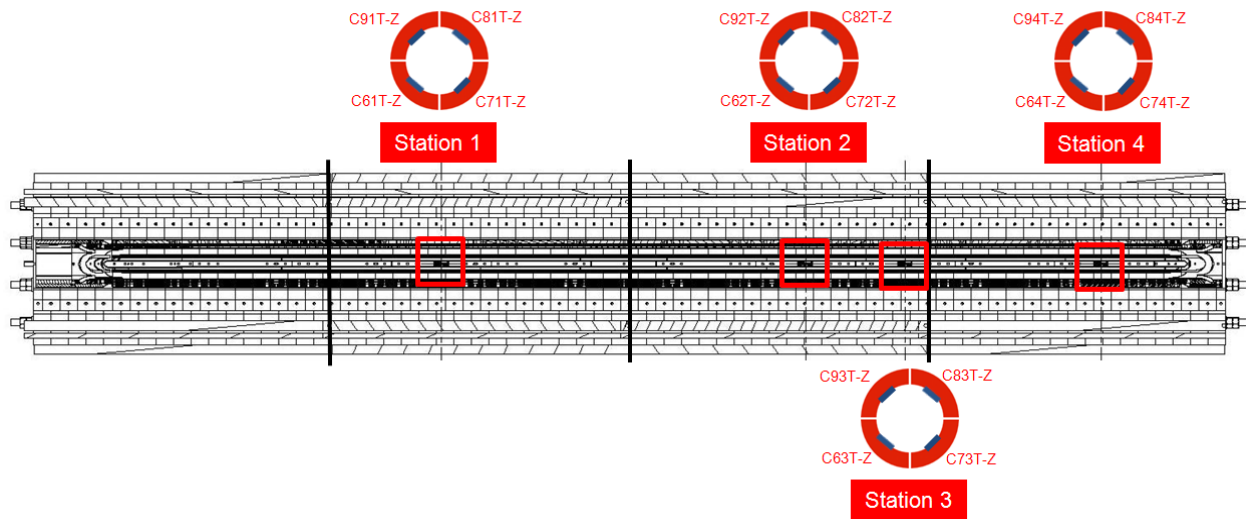


Fig. 17. Locations of the coil strain gauges (blue markers).

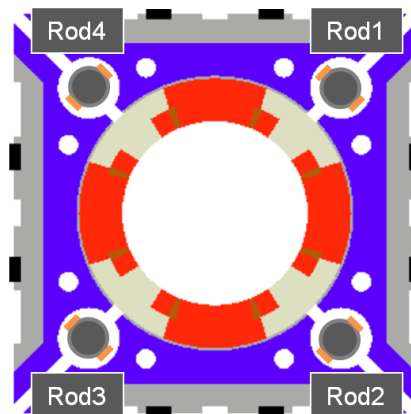


Fig. 18. Locations of the axial rod strain gauges (orange markers).

The plots in Fig. 33-48 show the strain gauge measurements taken during cool-down (as a function of data point), excitation (as a function of current squared  $I^2$ ), and warm-up (as a function of data point) of the first thermal cycle. The plots in Fig. 49-78 show the strain gauge measurements taken during cool-down (as a function of data point), excitation (as a function of current squared  $I^2$ ), and warm-up (as a function of data point) of the second thermal cycle.

The data are compared with the predictions of a 3D finite element model (described in [3]) of the entire magnet geometry. According to the finite element model, the 293 K and 4.3 K stresses chosen as target values for the shell and rods provide a coil pre-load sufficient to avoid separation between the turns and the Ti-alloy pole pieces up to a gradient of 250-260 T/m. At 4.5 K, the shell reached a tension of  $+200 \pm 10$  MPa, about 50 MPa more than in LQS01a, while the rod was tensioned to  $+240 \pm 10$  MPa ( $+200 \pm 10$  MPa in LQS01a). As a result of the structure modifications and the choice of a higher stress target, the pole pre-load after cool-down went from  $-25 \pm 20$  MPa in LQS01a to  $-130 \pm 30$  MPa in LQS01b, and no separation was observed between coil and pole during excitation.

It is important to point out that, in term of variation of coil pre-load during cool-down, LQS01b exhibited the same discrepancy with numerical expectation as LQS01a. A clear explanation for this behavior has not been found yet, and the data cannot be reproduced by finite element models. A possible cause, still under investigation, may reside on an error in the temperature compensation.

## 8.1 Cool-down first thermal cycle

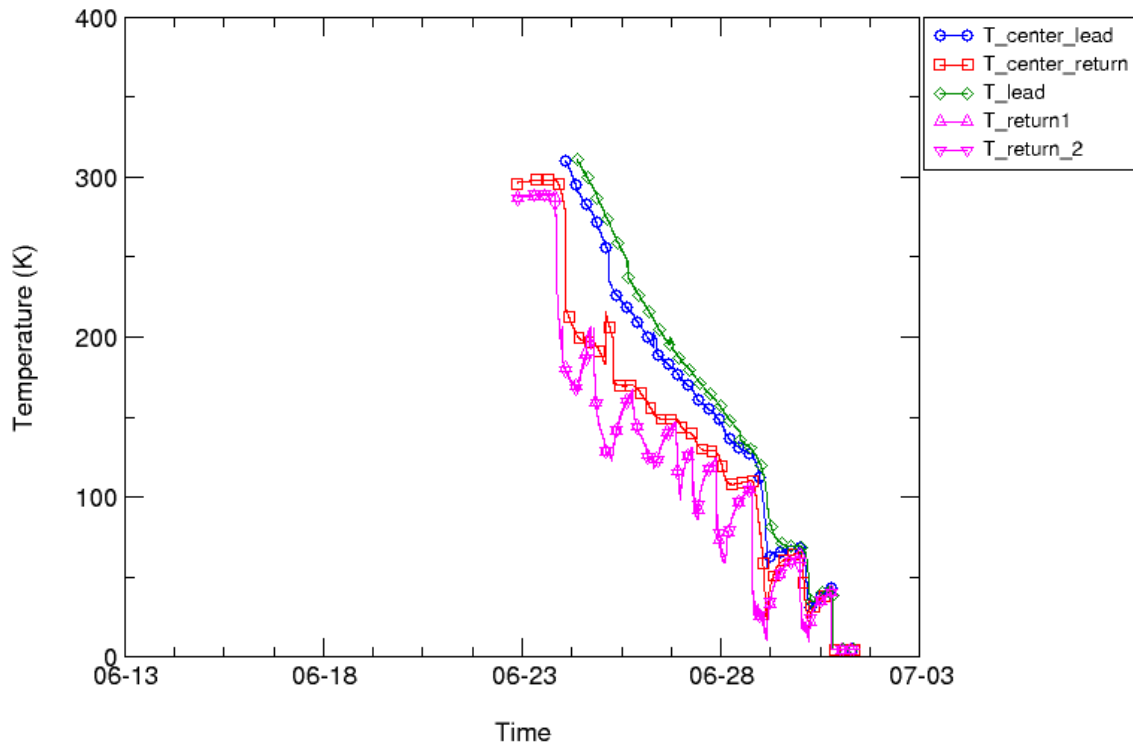


Fig. 19. Temperature of the shell measured during cool-down vs. time.

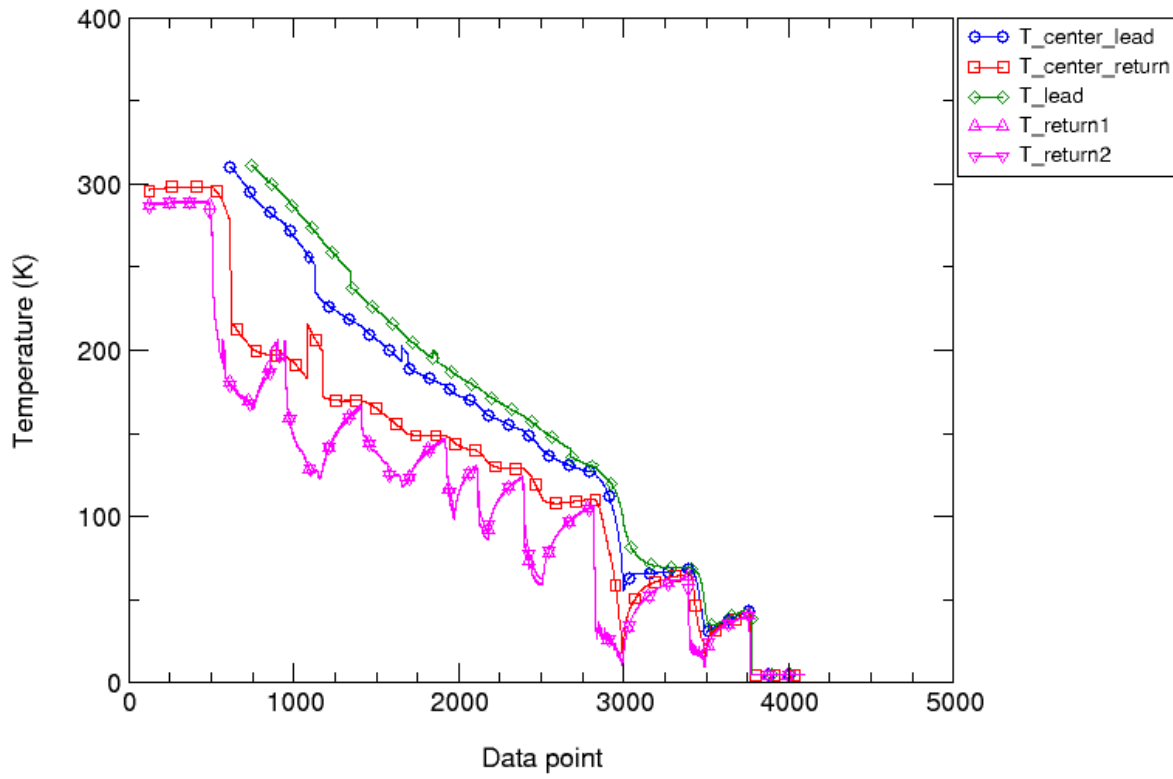


Fig. 20. Temperature of the shell measured during cool-down vs. data point.

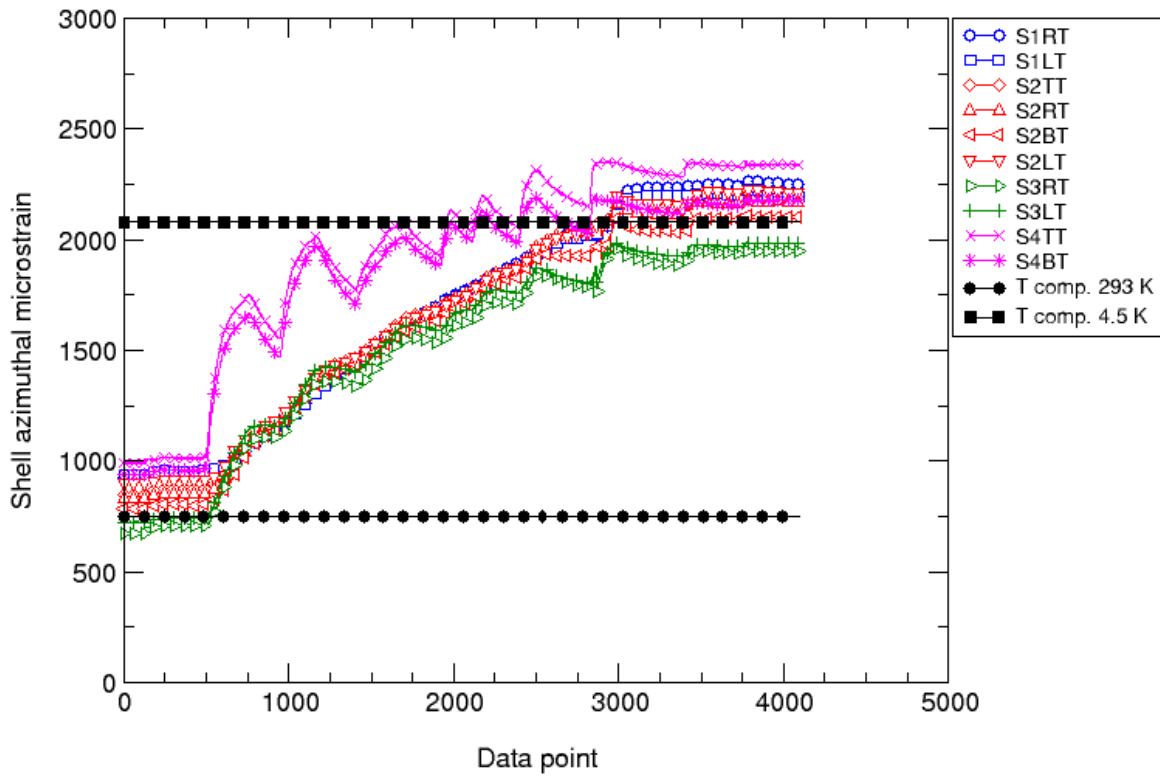


Fig. 21. Azimuthal microstrain in the shell during cool-down: values measured (colored markers) and computed (black markers) from a 3D finite element model.

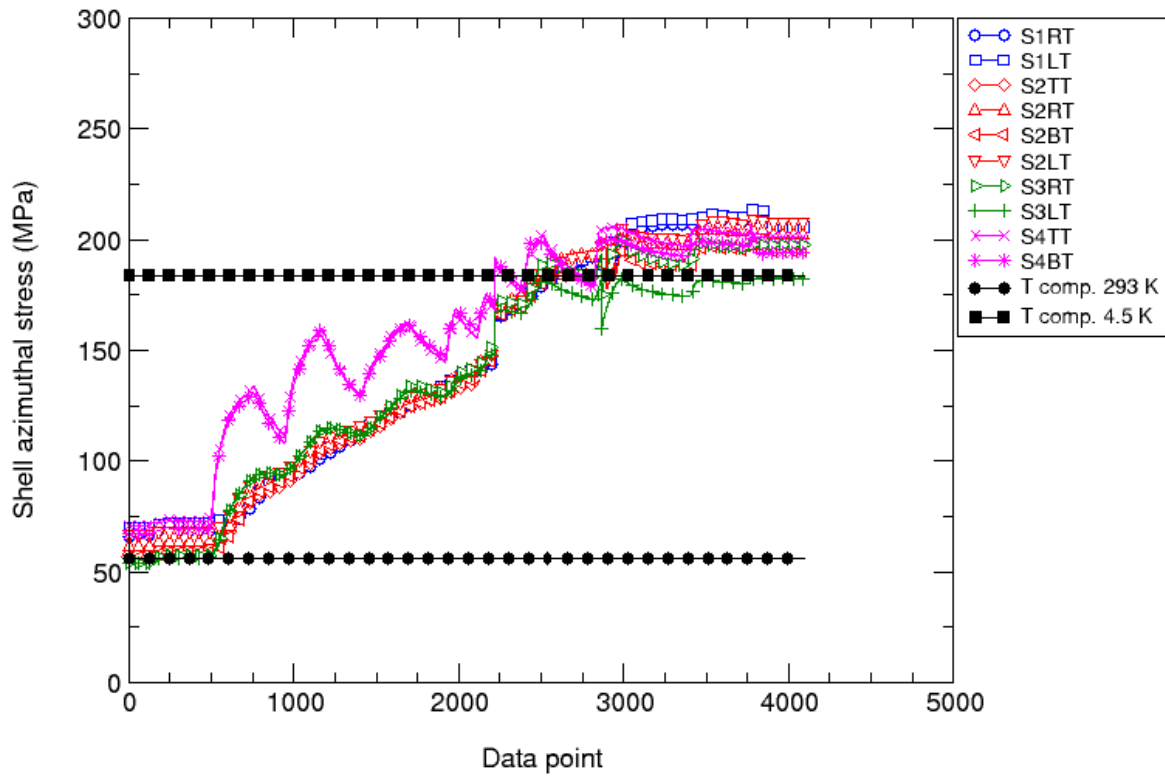


Fig. 22. Azimuthal stress (MPa) in the shell during cool-down: values measured (colored markers) and computed (black markers) from a 3D finite element model.

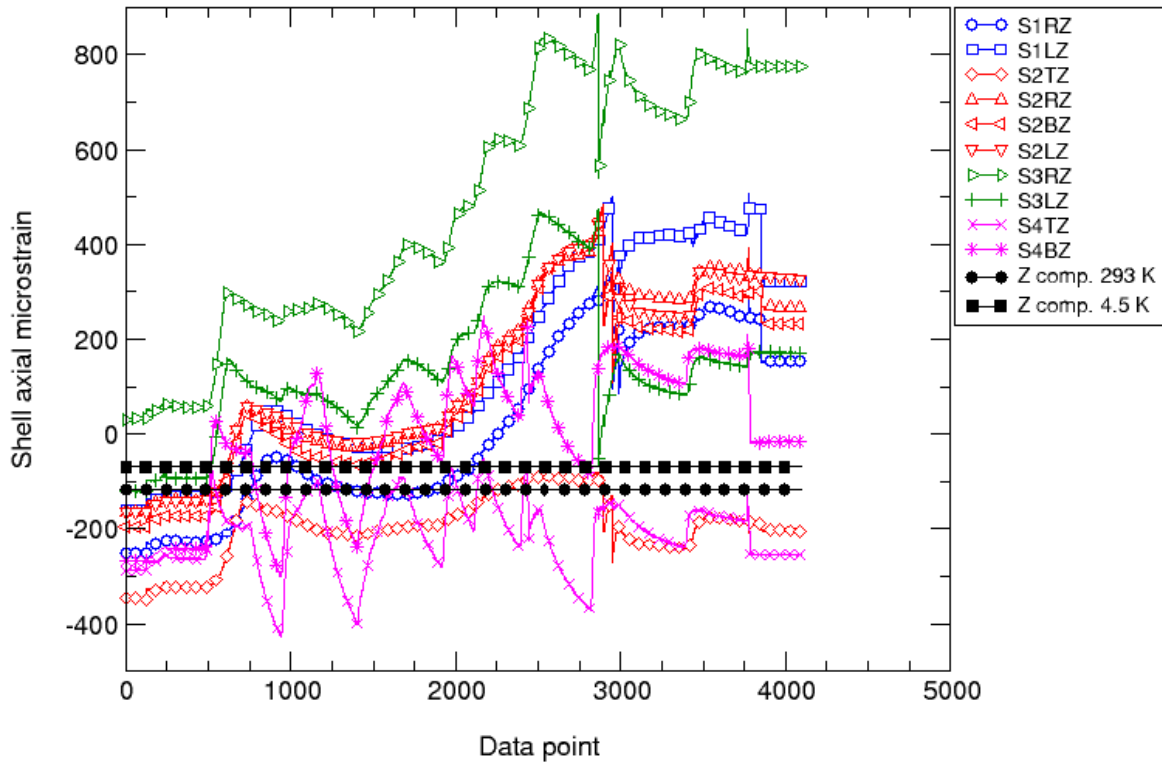


Fig. 23. Axial microstrain in the shell during cool-down: values measured (colored markers) and computed (black markers) from a 3D finite element model.

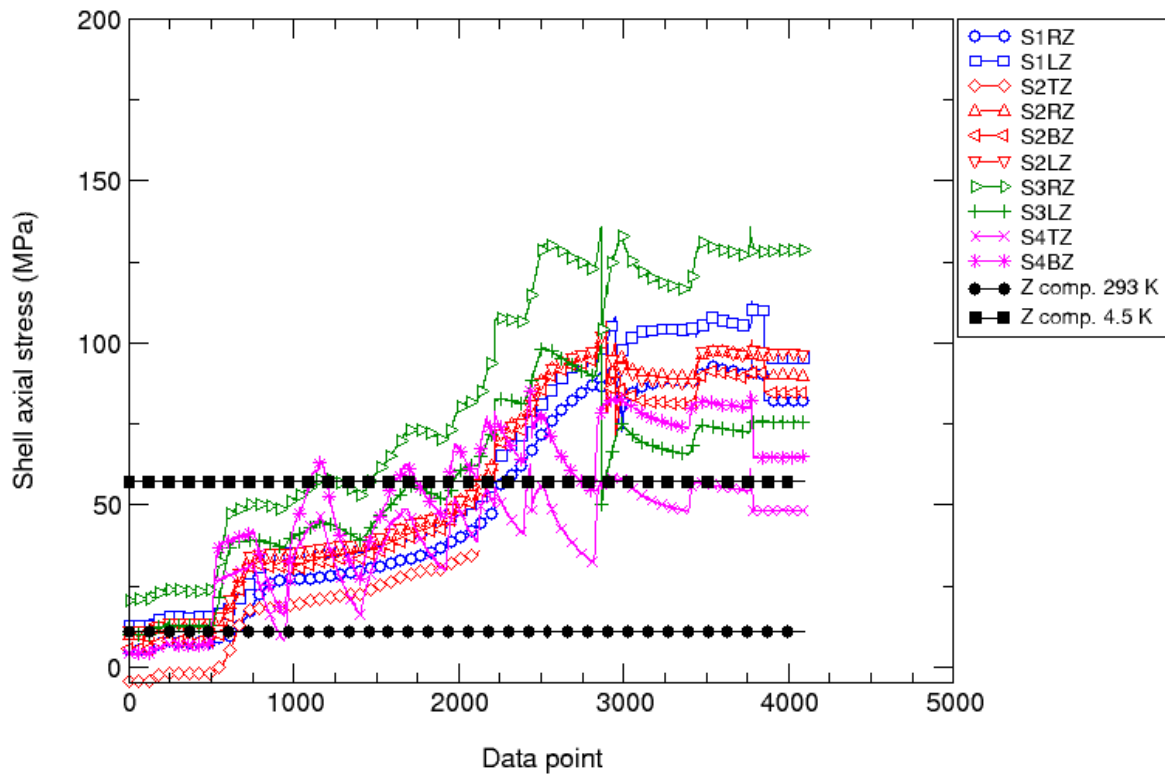


Fig. 24. Axial stress (MPa) in the shell during cool-down: values measured (colored markers) and computed (black markers) from a 3D finite element model.

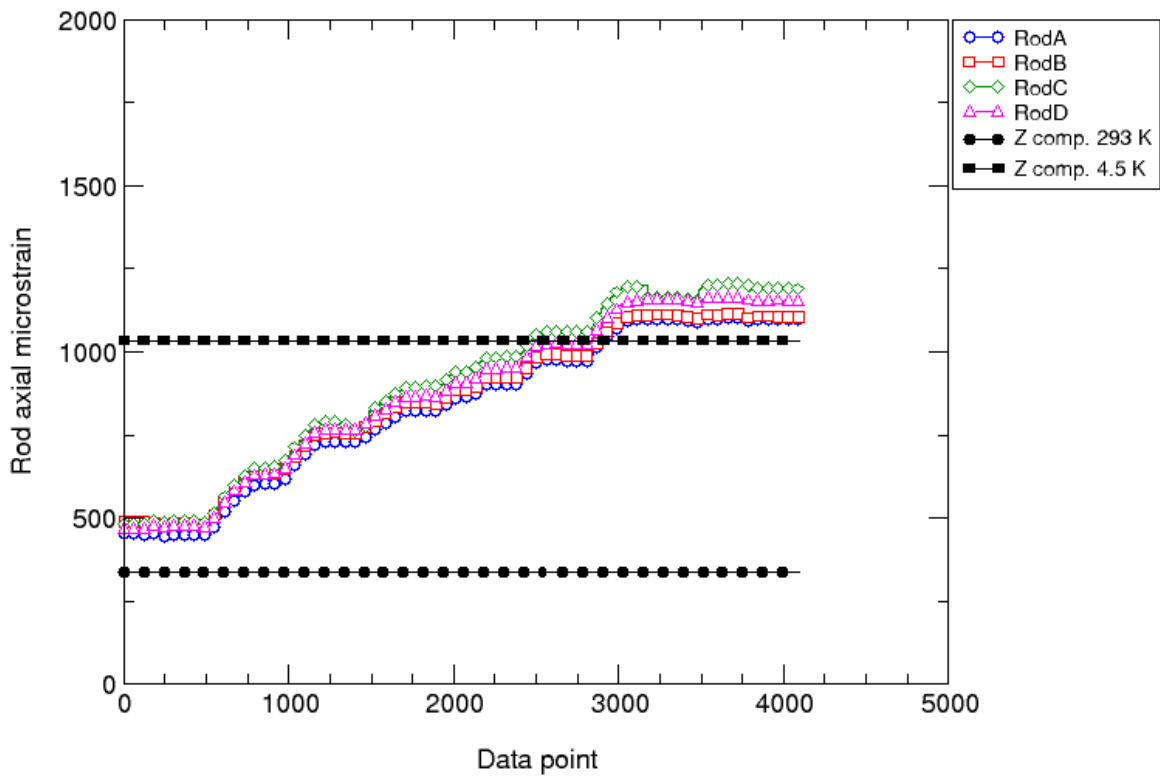


Fig. 25. Axial microstrain in the rods during cool-down: values measured (colored markers) and computed (black markers) from a 3D finite element model.



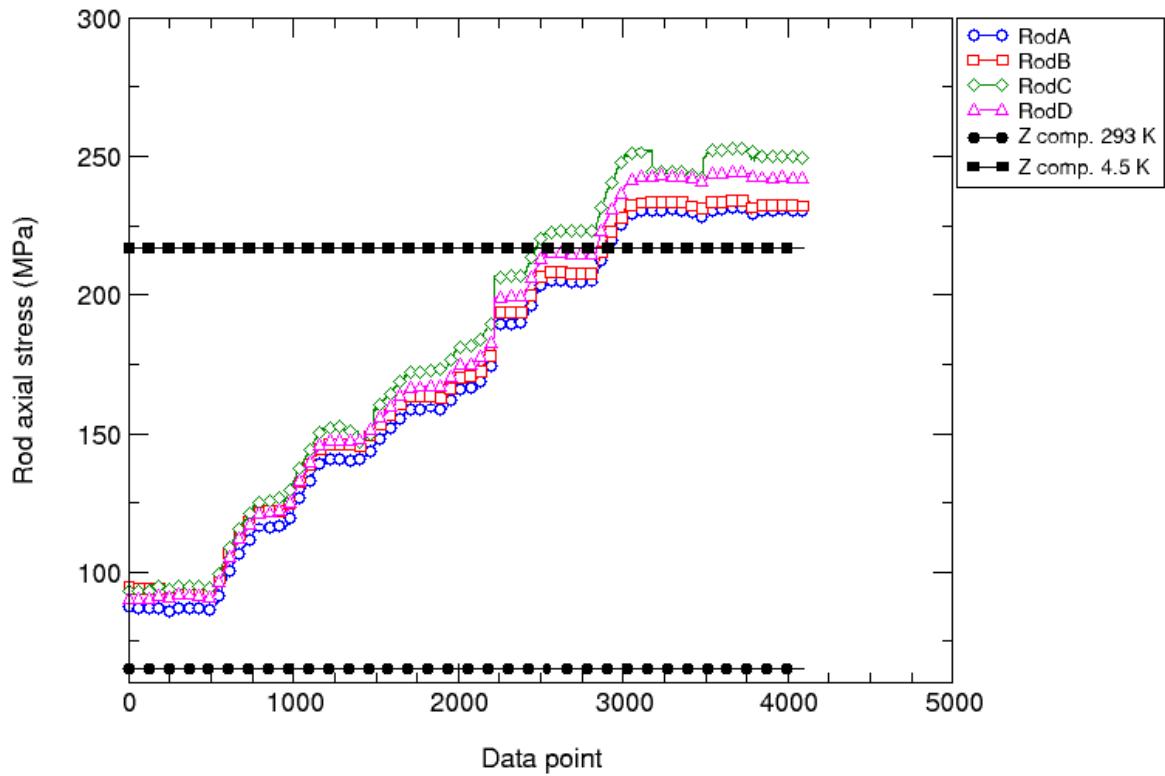


Fig. 26. Axial stress (MPa) in the rods during cool-down: values measured (colored markers) and computed (black markers) from a 3D finite element model.

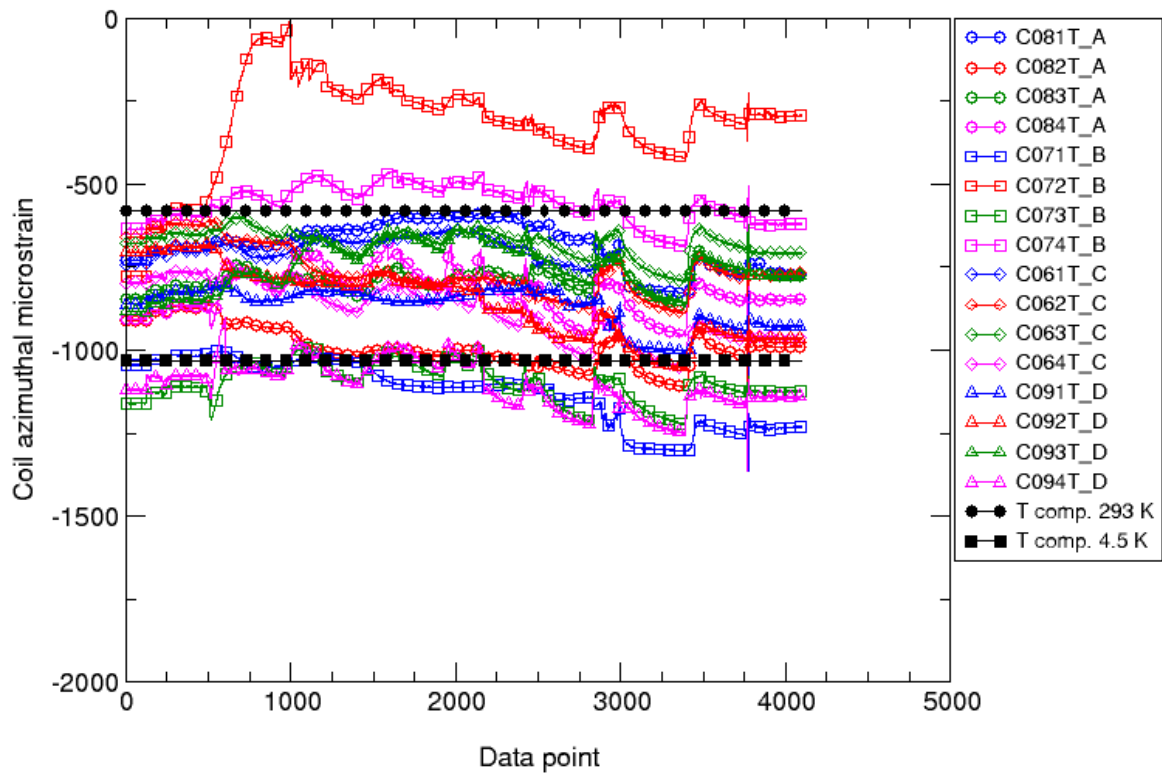


Fig. 27. Azimuthal microstrain in the coil poles during cool-down: values measured (colored markers) and computed (black markers) from a 3D finite element model.

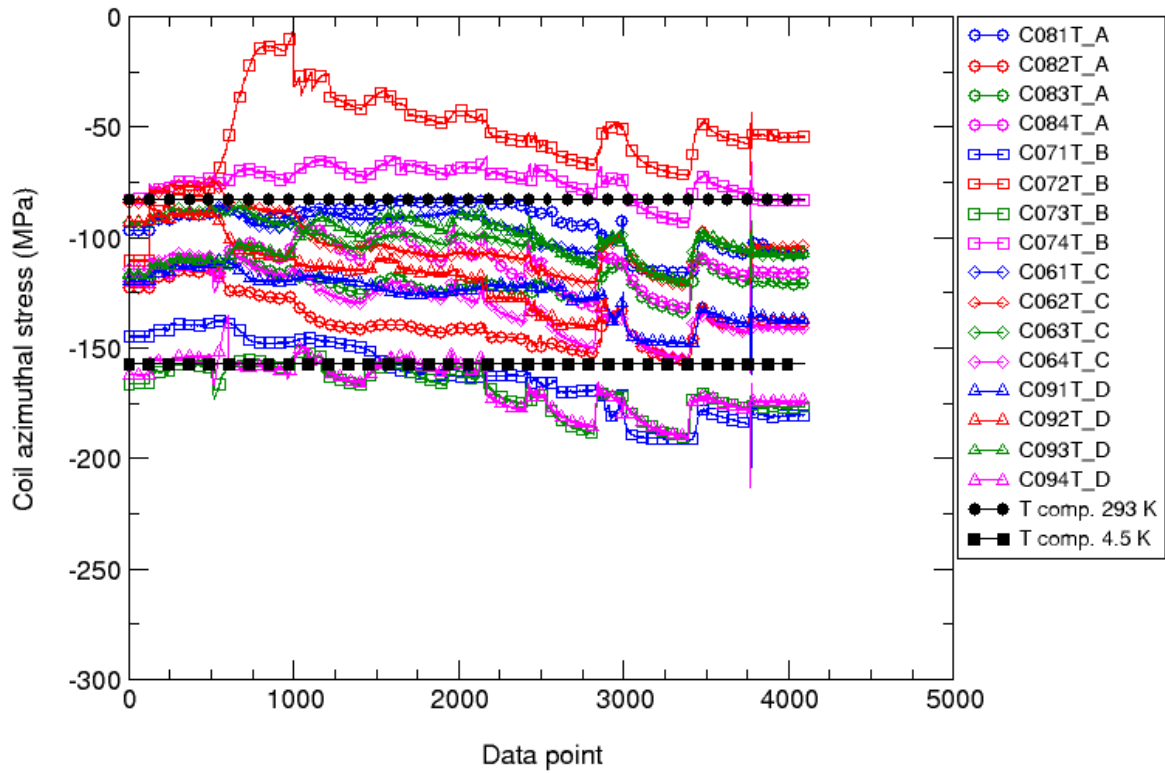


Fig. 28. Azimuthal stress (MPa) in the coil poles during cool-down: values measured (colored markers) and computed (black markers) from a 3D finite element model.

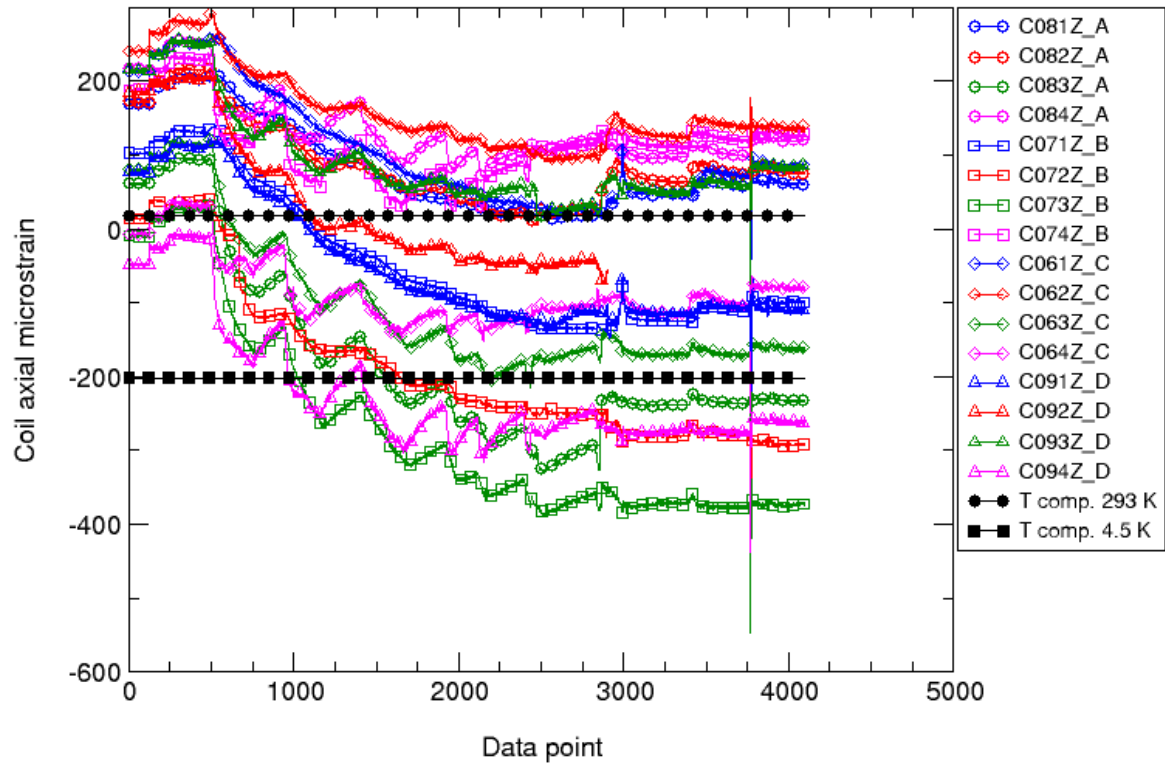


Fig. 29. Axial microstrain in the coil poles during cool-down: values measured (colored markers) and computed (black markers) from a 3D finite element model.

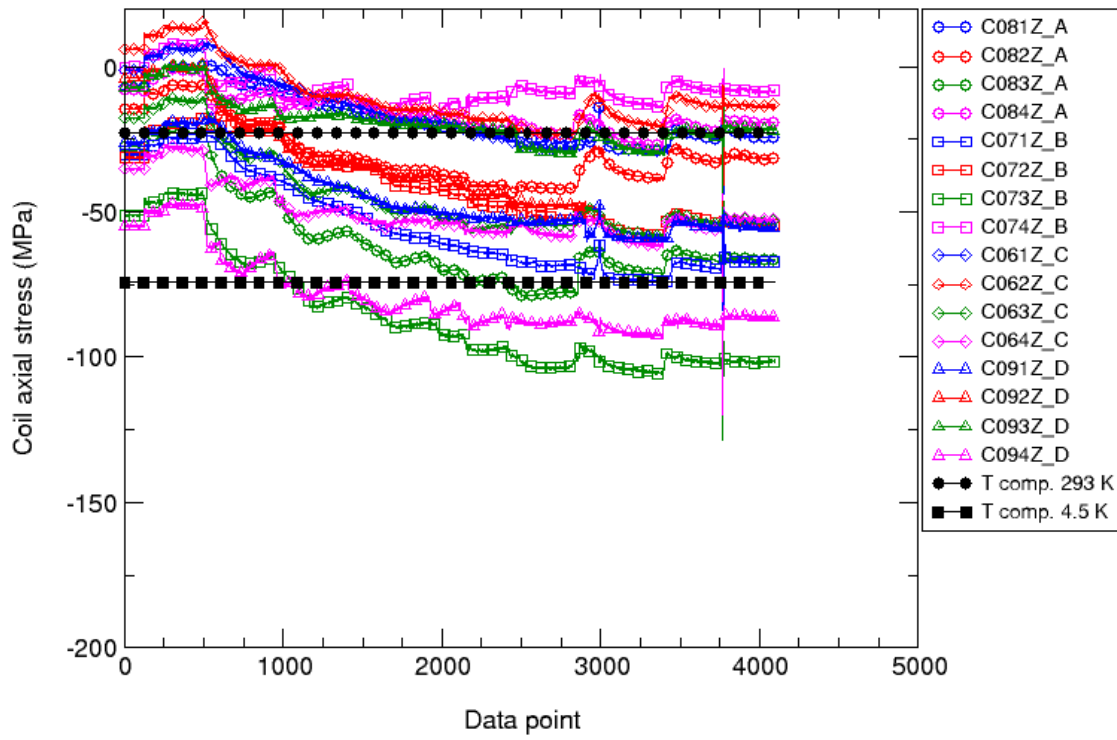


Fig. 30. Axial stress (MPa) in the coil poles during cool-down: values measured (colored markers) and computed (black markers) from a 3D finite element model.

## 8.2 Excitation first thermal cycle

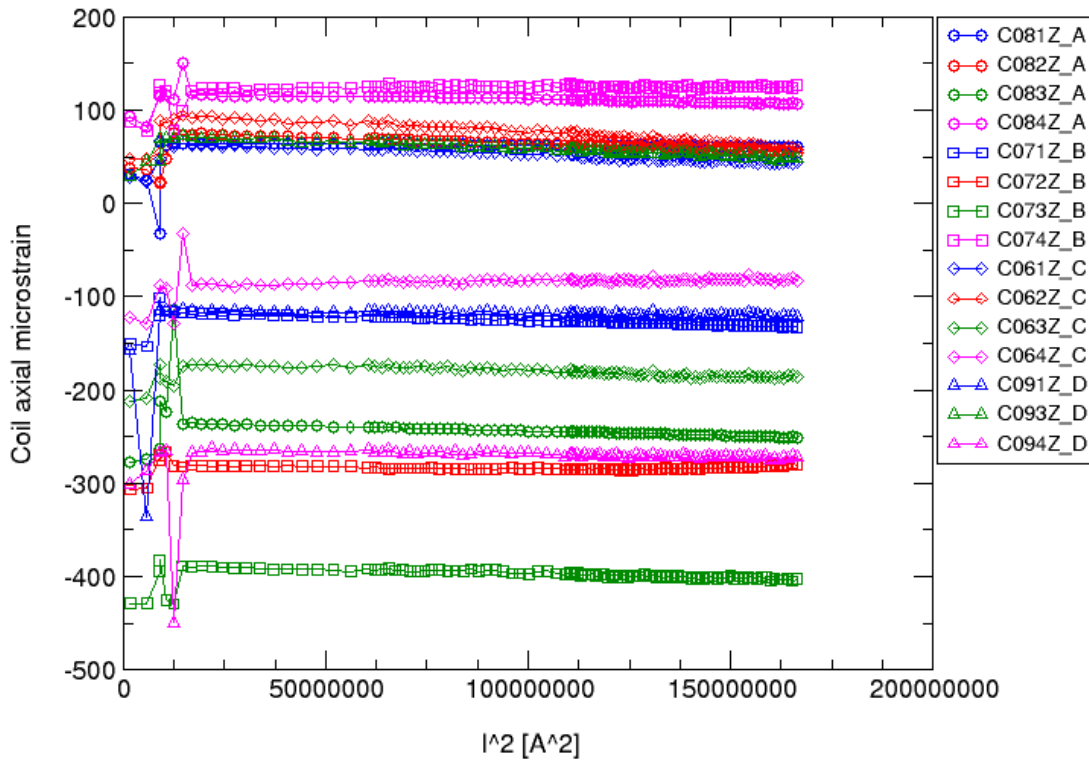


Fig. 31. Axial strain in the coil poles (all stations) vs.  $I^2$  ( $A^2$ ) for quench # 38 (12952 A).

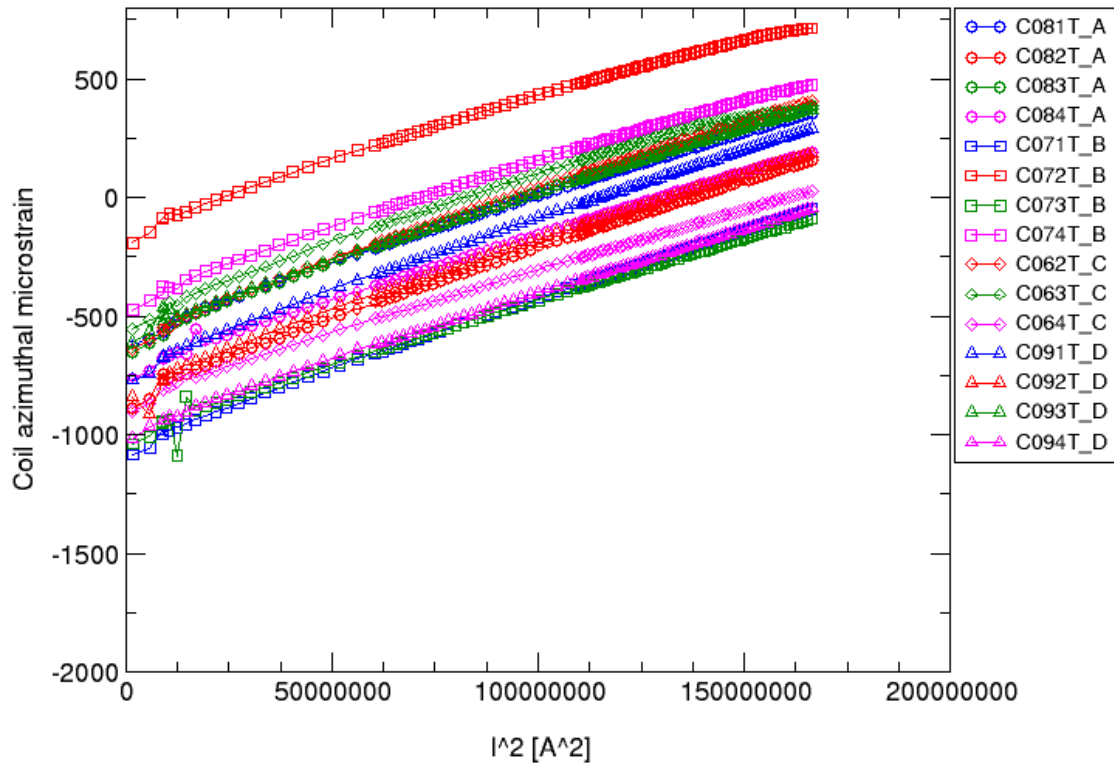


Fig. 32. Azimuthal strain in the coil poles (all stations) vs.  $I^2$  ( $A^2$ ) for quench # 38 (12952 A).

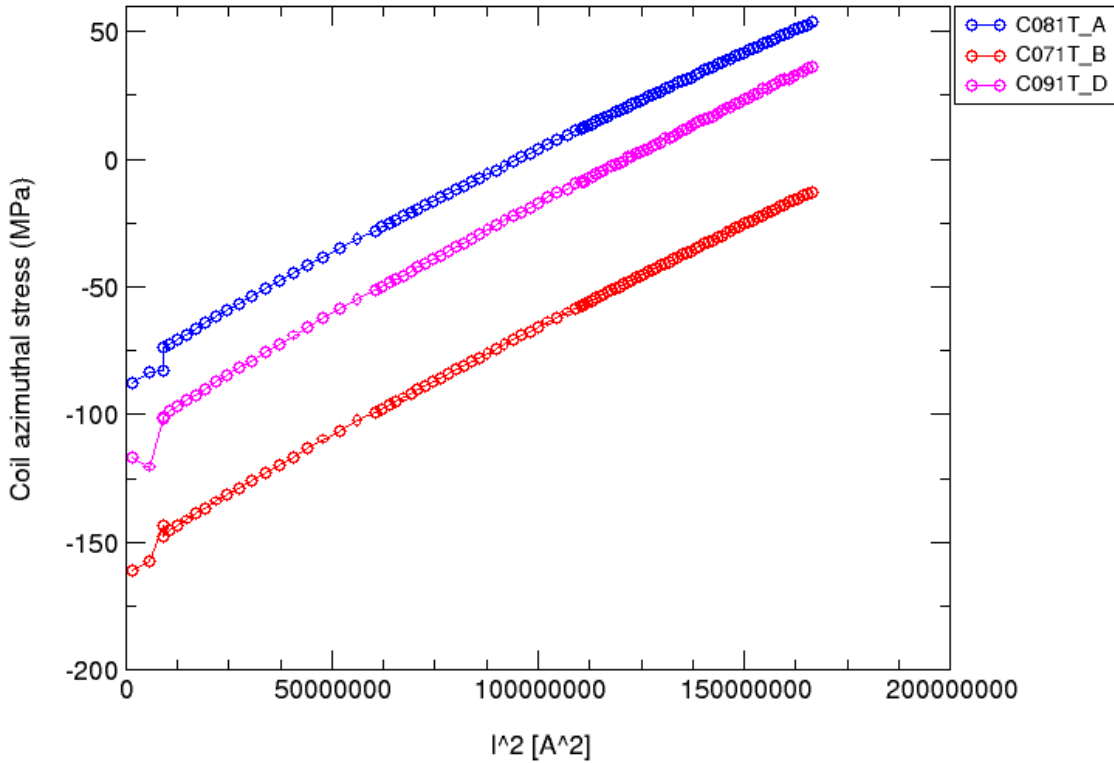


Fig. 33. Azimuthal stress (MPa) in the coil poles (station 1) vs.  $I^2$  ( $A^2$ ) for quench # 38 (12952 A).

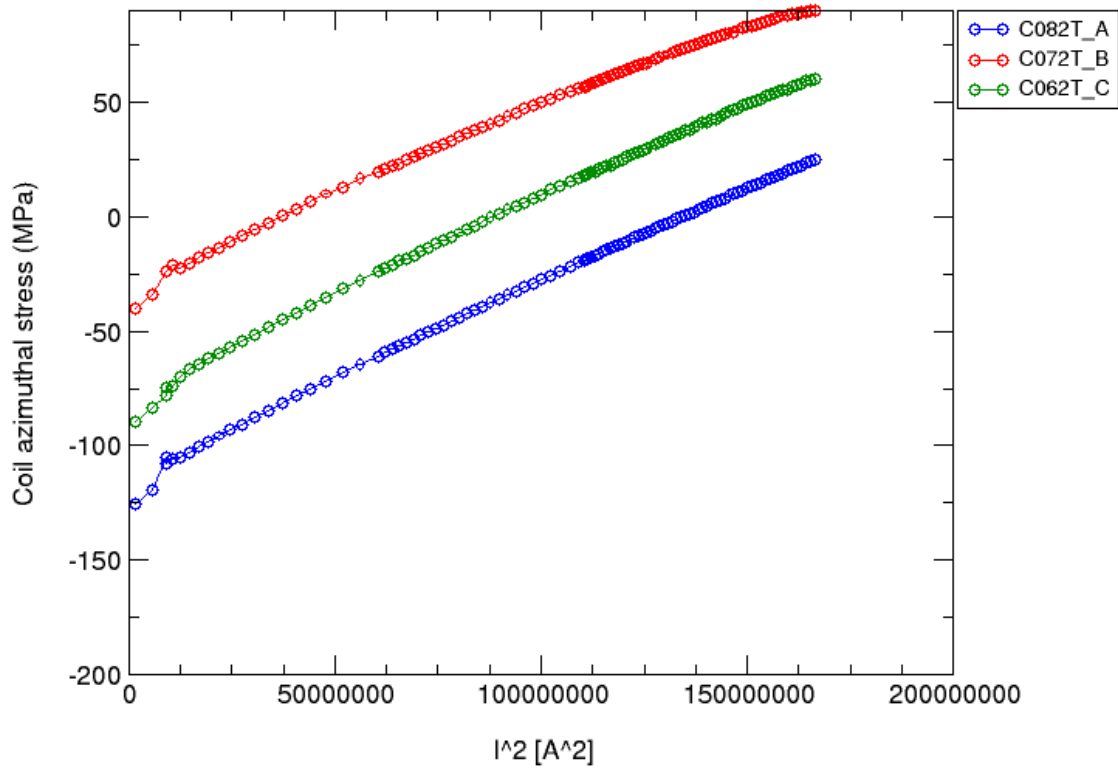


Fig. 34. Azimuthal stress (MPa) in the coil poles (station 2) vs.  $I^2$  (A<sup>2</sup>) for quench # 38 (12952 A).

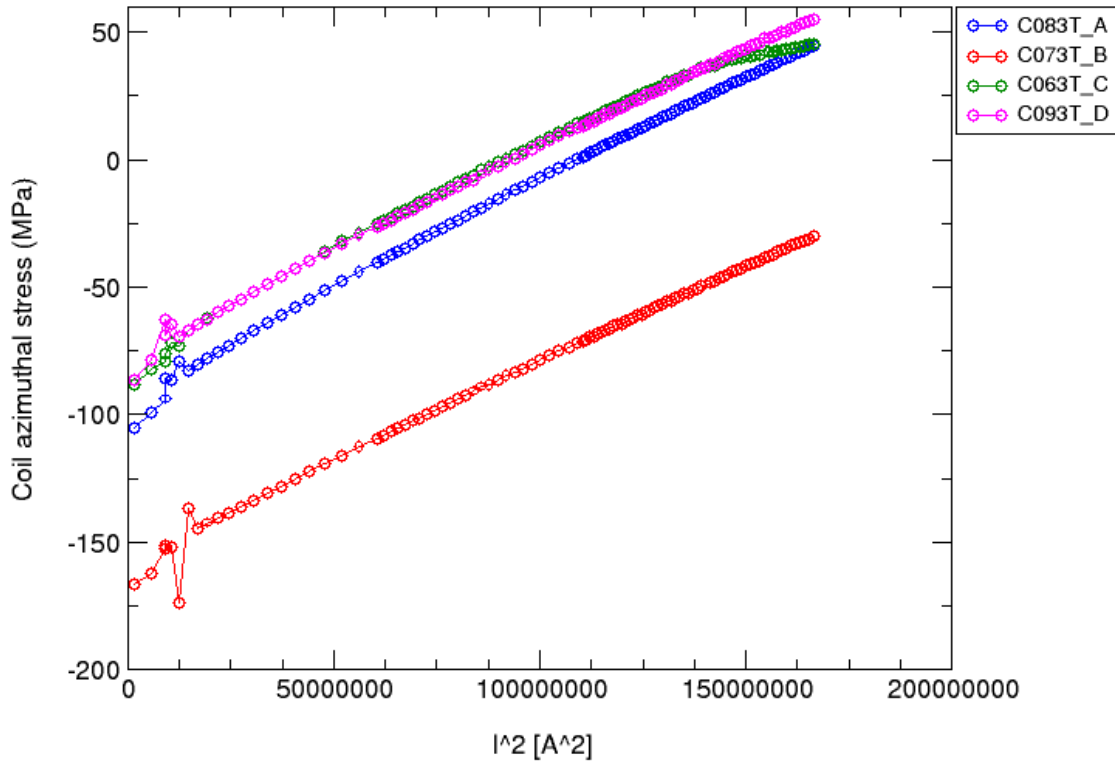


Fig. 35. Azimuthal stress (MPa) in the coil poles (station 3) vs.  $I^2$  (A<sup>2</sup>) for quench # 38 (12952 A).

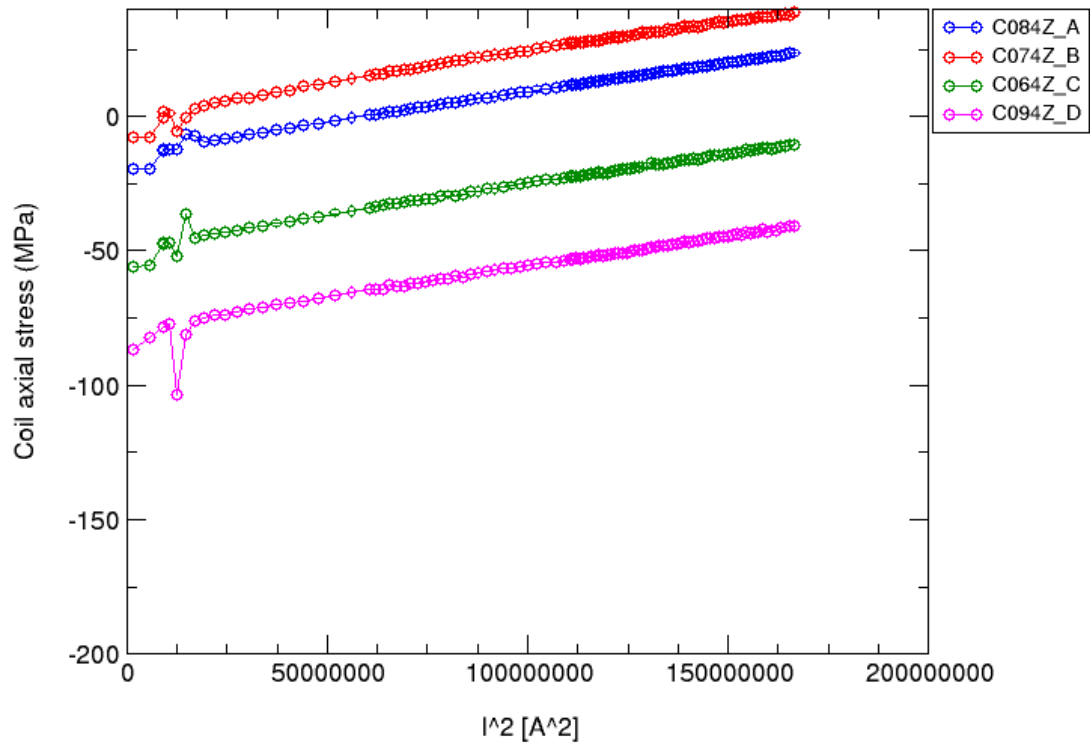


Fig. 36. Azimuthal stress (MPa) in the coil poles (station 4) vs.  $I^2$  (A<sup>2</sup>) for quench # 38 (12952 A).

### 8.3 Warm-up first thermal cycle

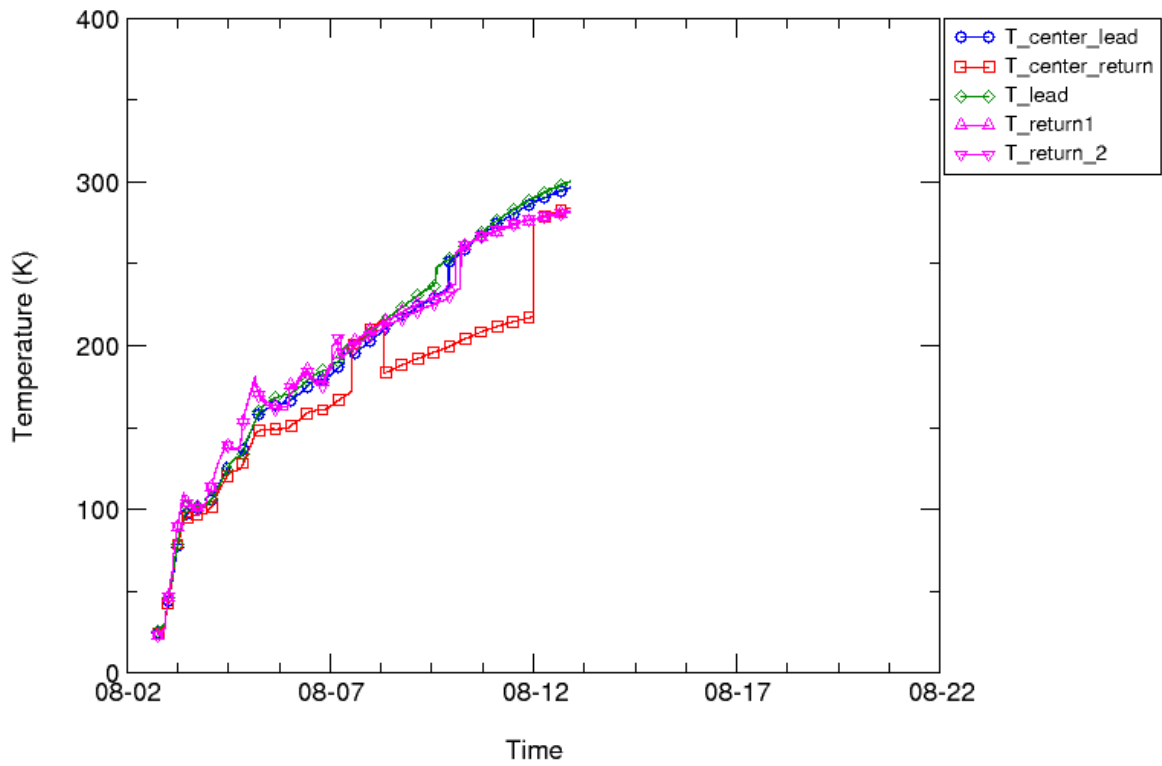


Fig. 37. Temperature of the shell measured during warm-up vs. time.

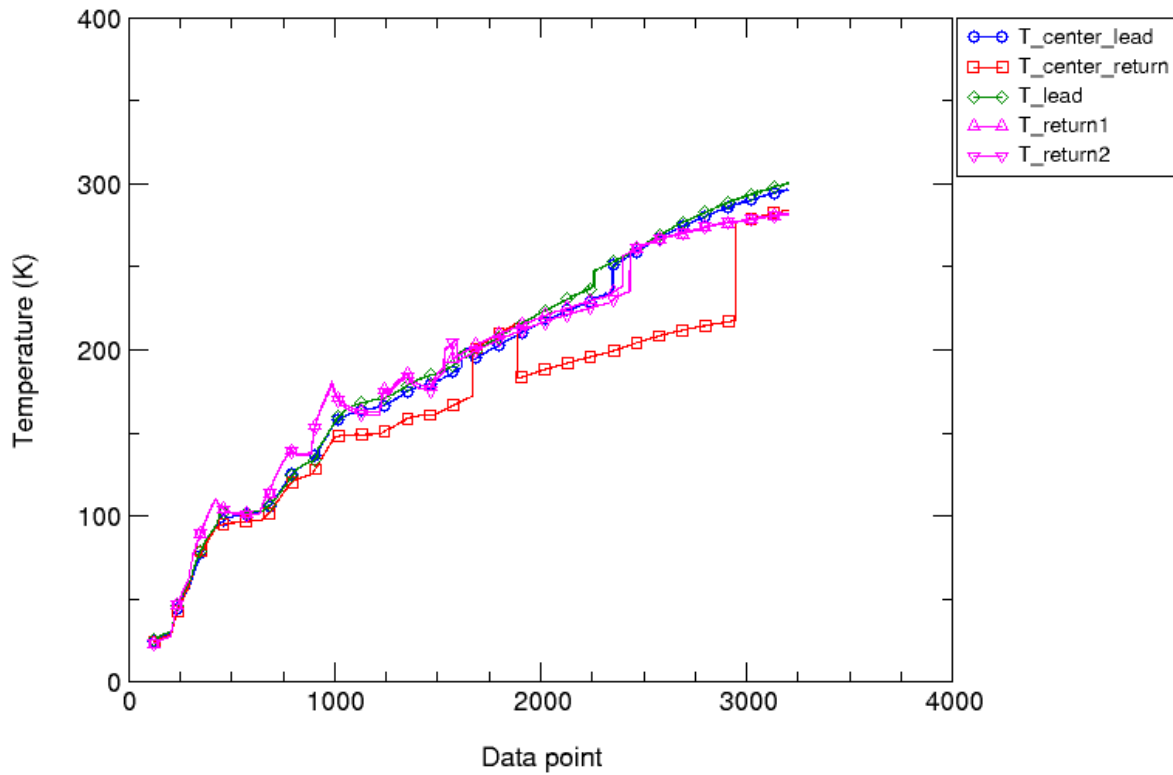


Fig. 38. Temperature of the shell measured during warm-up vs. data point.

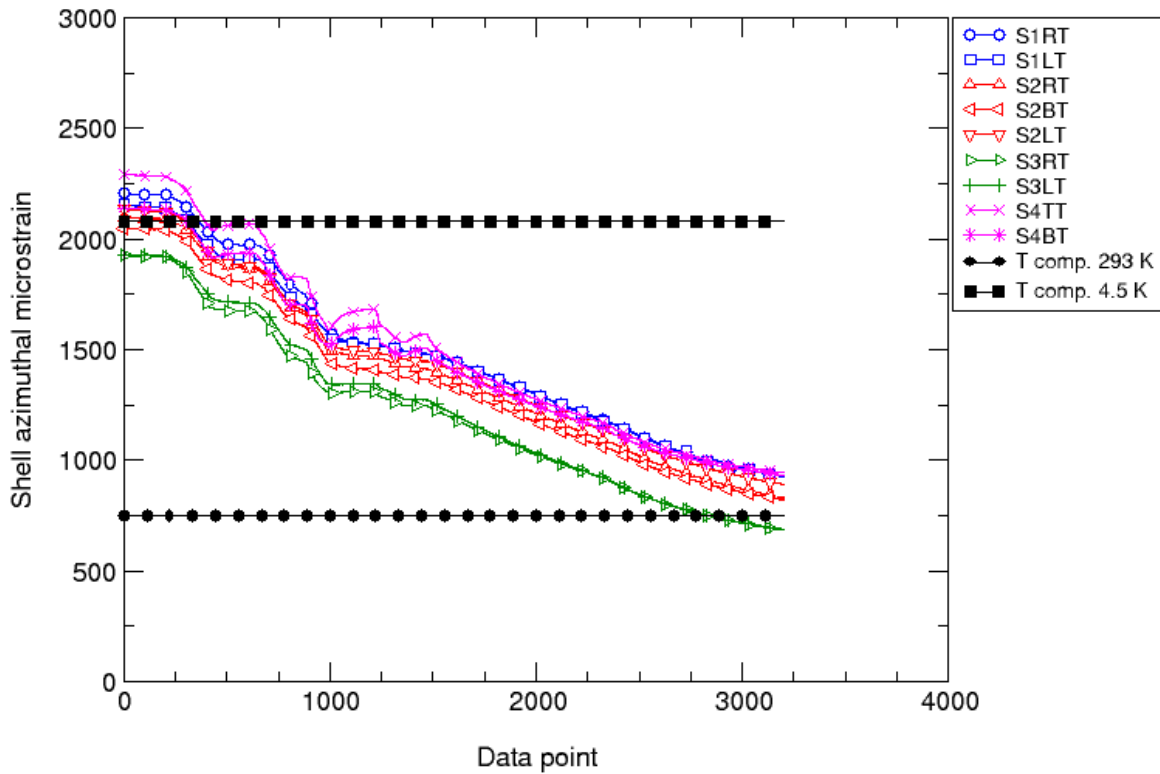


Fig. 39. Azimuthal microstrain in the shell during warm-up: values measured (colored markers) and computed (black markers) from a 3D finite element model.

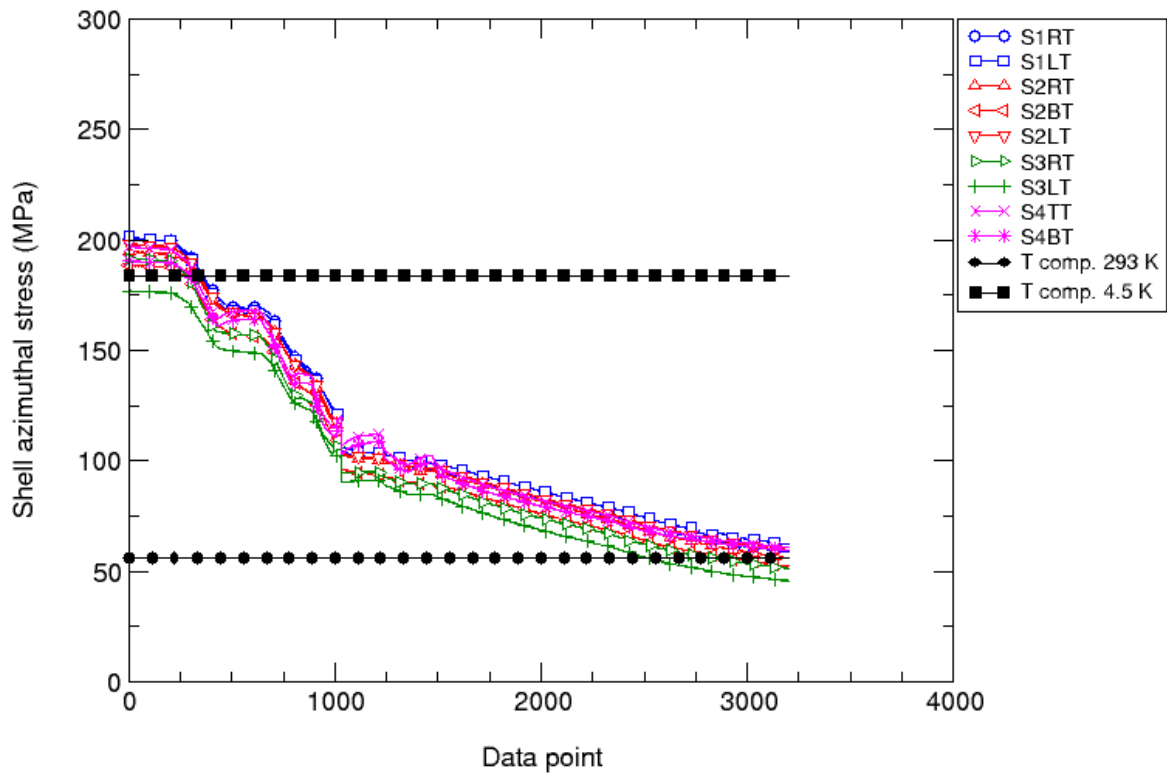


Fig. 40. Azimuthal stress (MPa) in the shell during warm-up: values measured (colored markers) and computed (black markers) from a 3D finite element model.

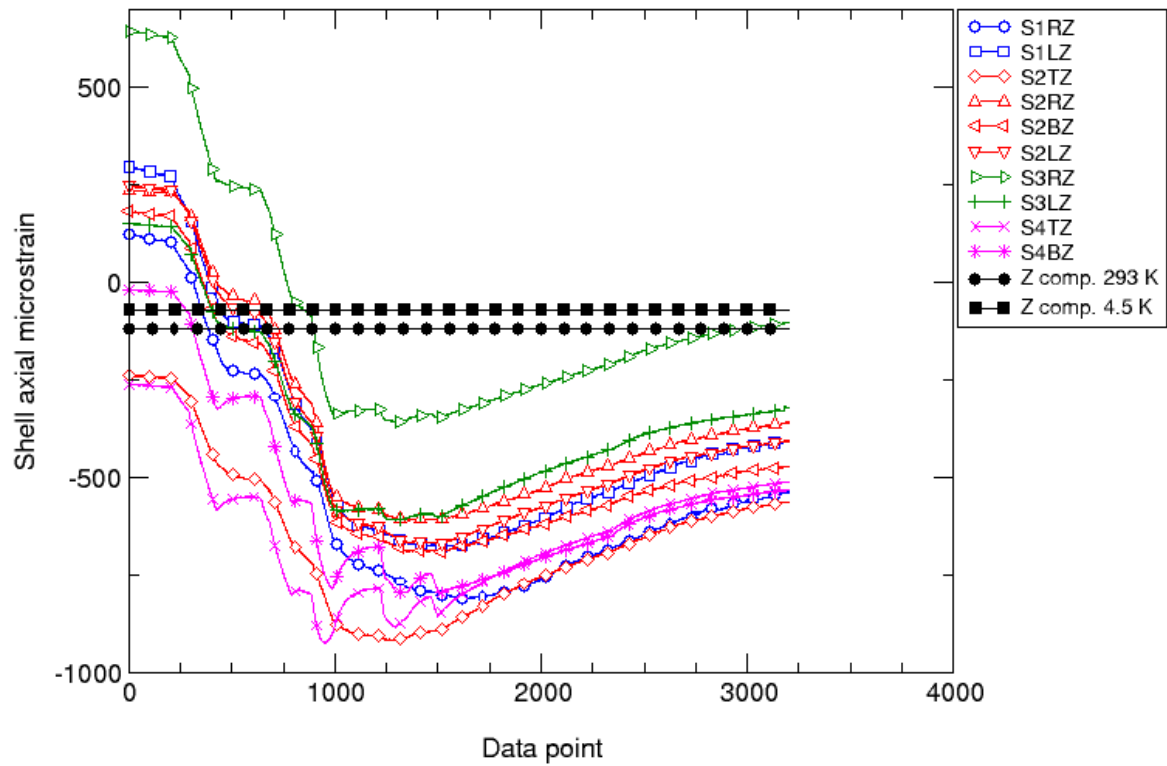


Fig. 41. Axial microstrain in the shell during warm-up: values measured (colored markers) and computed (black markers) from a 3D finite element model.



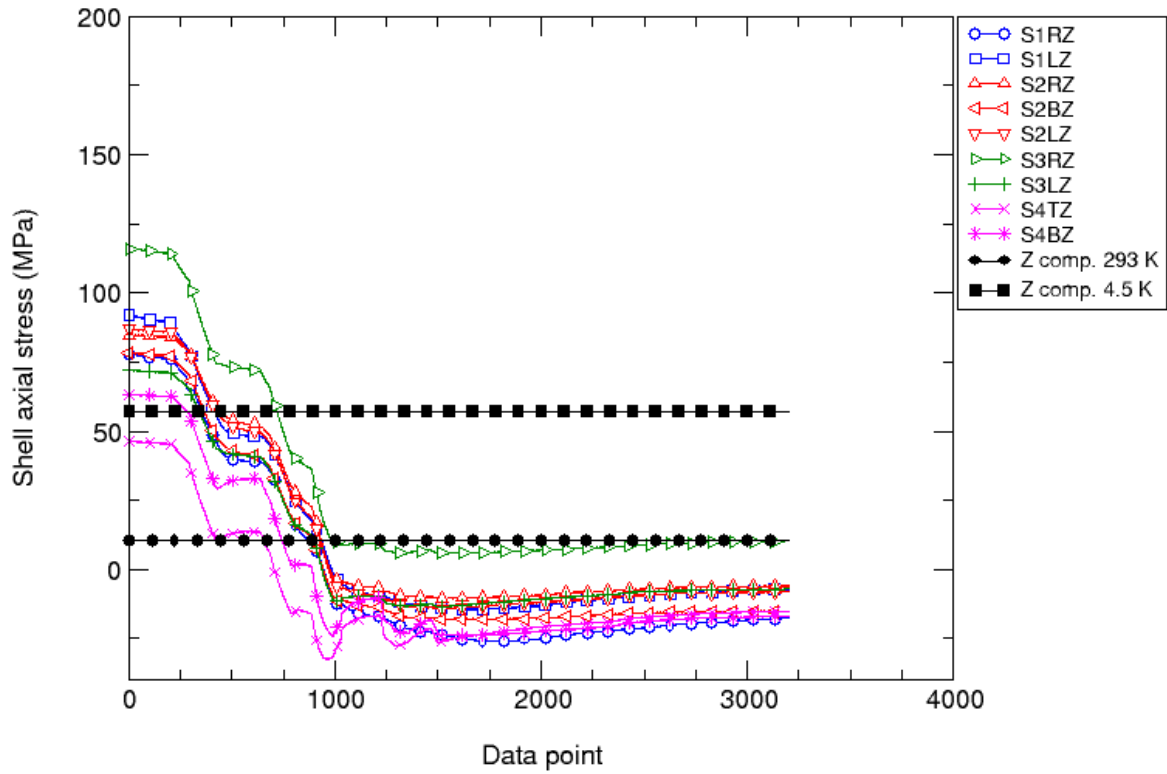


Fig. 42. Axial stress (MPa) in the shell during warm-up: values measured (colored markers) and computed (black markers) from a 3D finite element model.

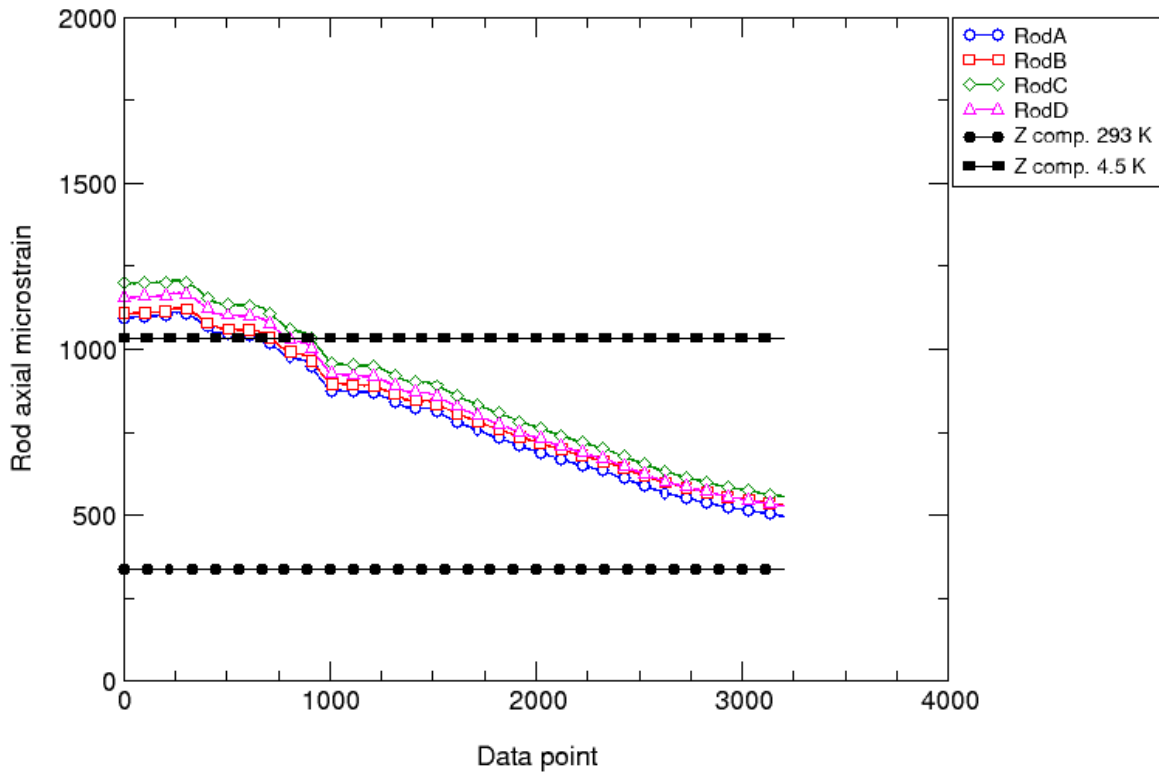


Fig. 43. Axial microstrain in the rods during warm-up: values measured (colored markers) and computed (black markers) from a 3D finite element model.

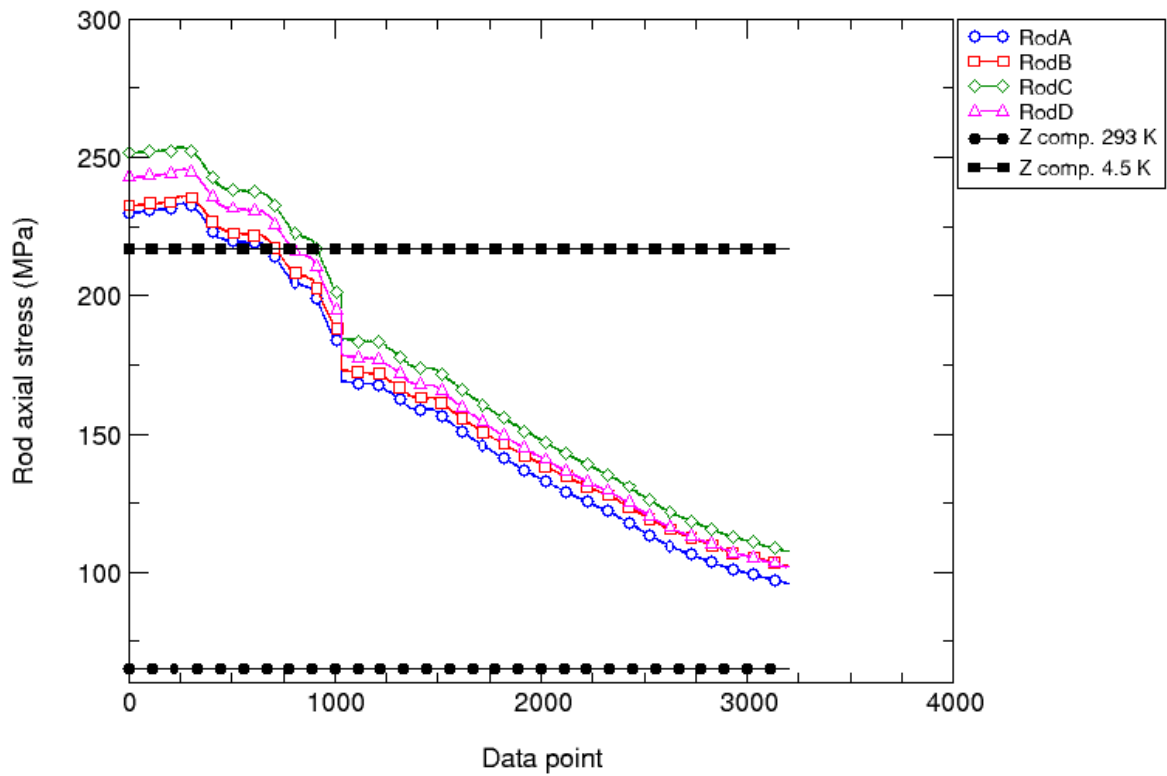


Fig. 44. Axial stress (MPa) in the rods during warm-up: values measured (colored markers) and computed (black markers) from a 3D finite element model.

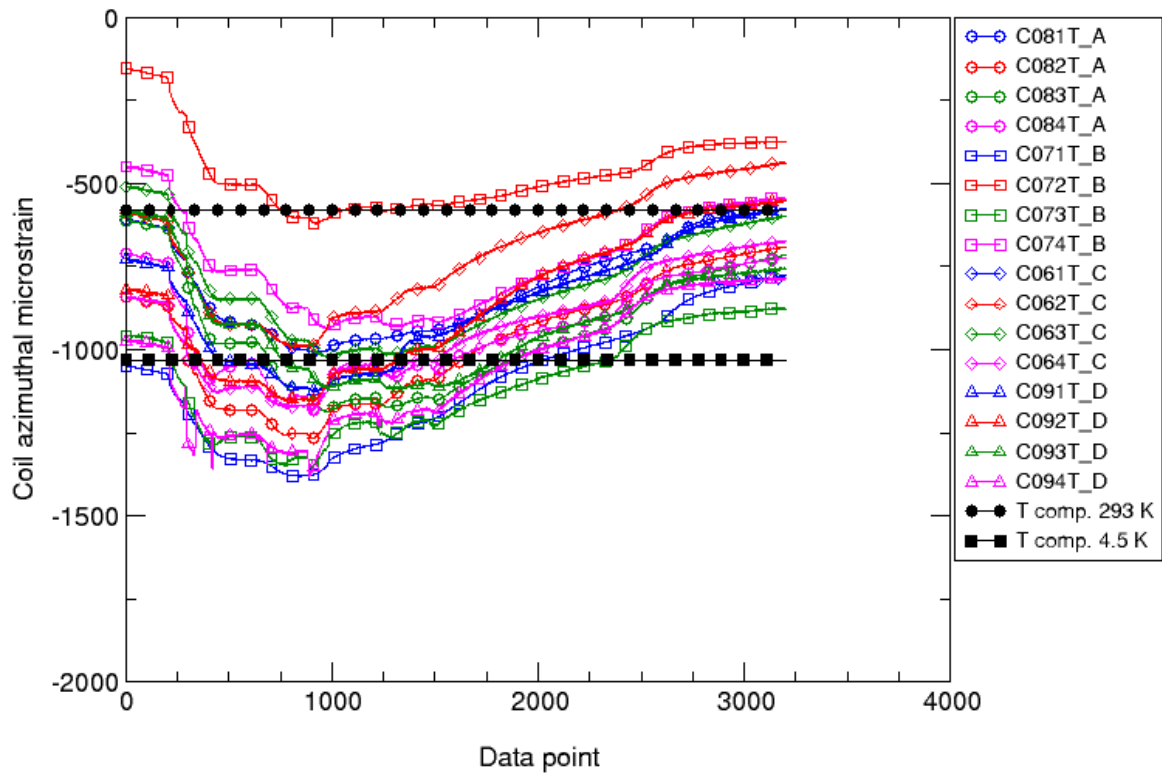


Fig. 45. Azimuthal microstrain in the coil poles during warm-up: values measured (colored markers) and computed (black markers) from a 3D finite element model.

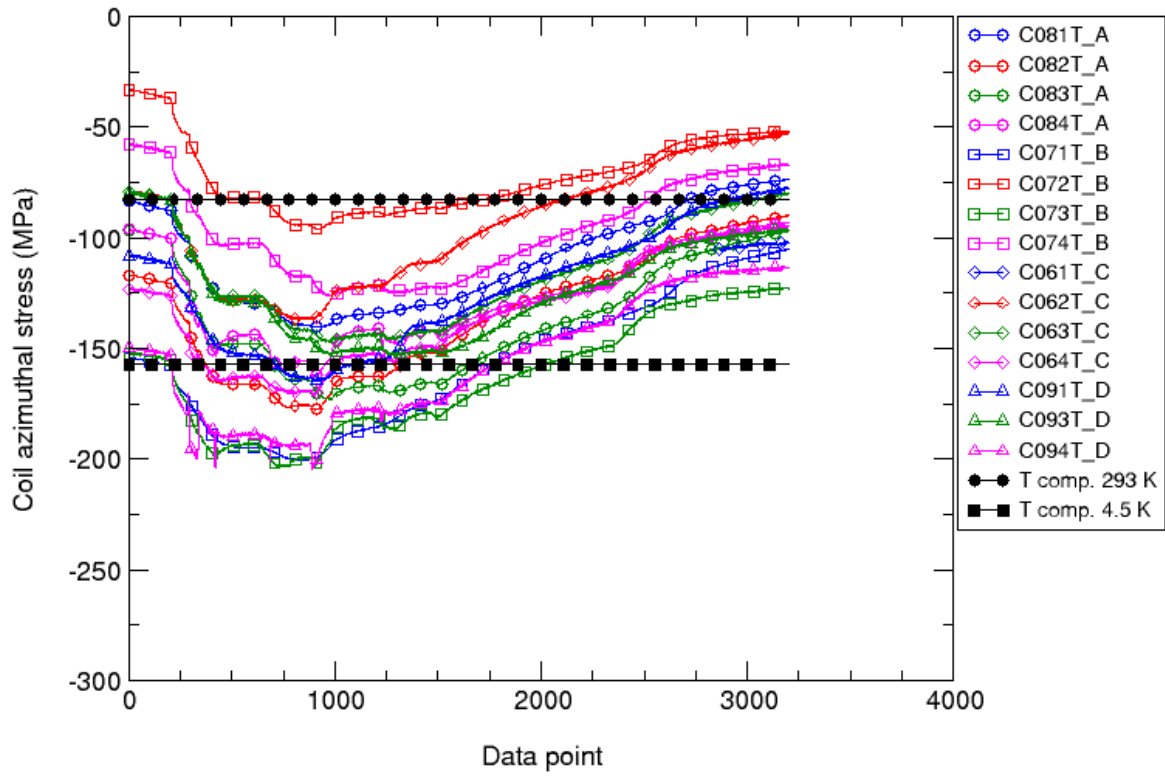


Fig. 46. Azimuthal stress (MPa) in the coil poles during warm-up: values measured (colored markers) and computed (black markers) from a 3D finite element model.

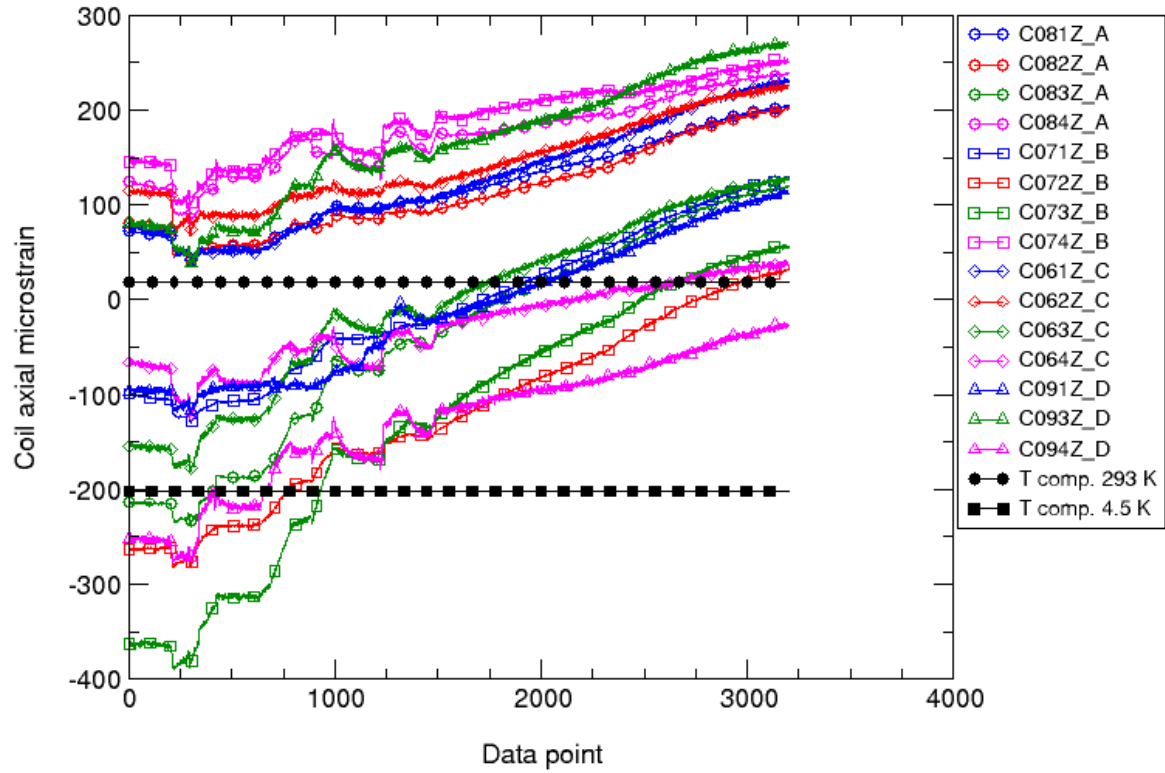


Fig. 47. Axial microstrain in the coil poles during warm-up: values measured (colored markers) and computed (black markers) from a 3D finite element model.

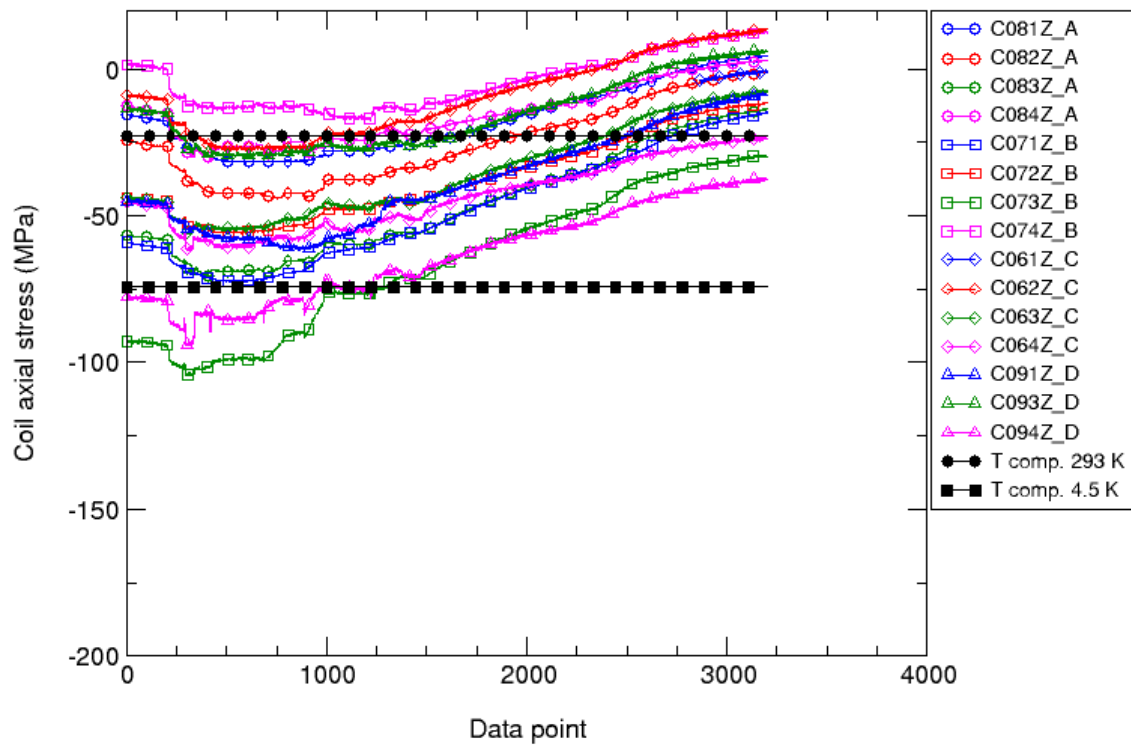


Fig. 48. Axial stress (MPa) in the coil poles during warm-up: values measured (colored markers) and computed (black markers) from a 3D finite element model.

#### 8.4 Cool-down second thermal cycle

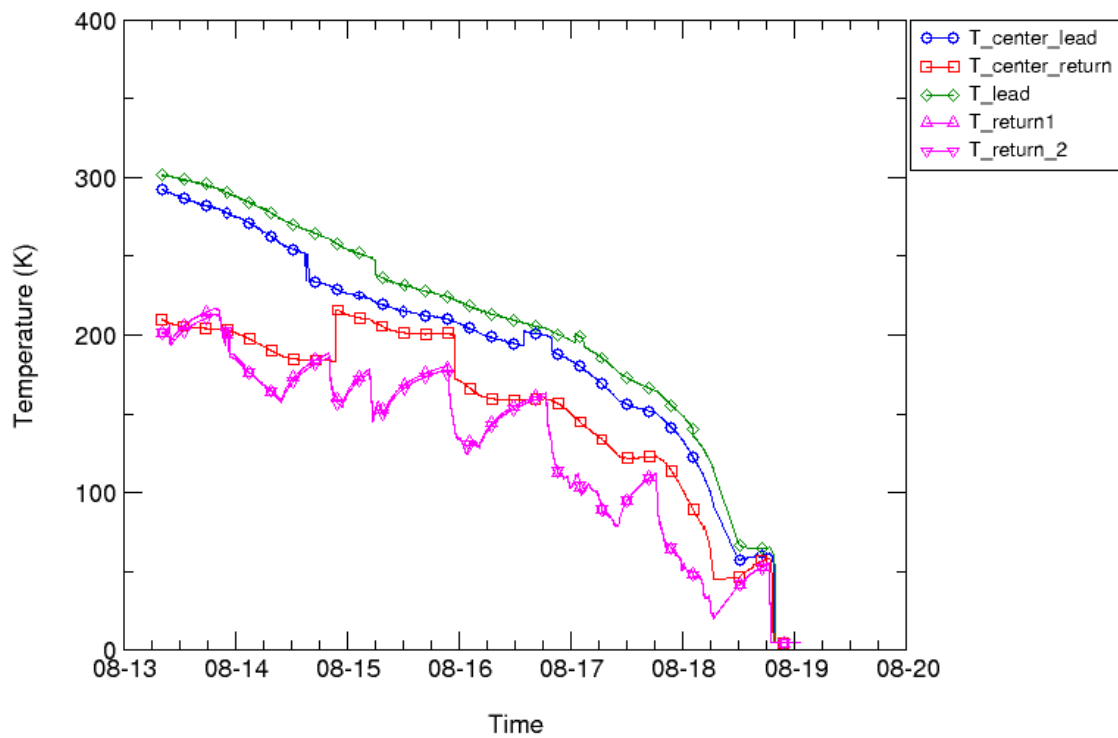


Fig. 49. Temperature of the shell measured during cool-down vs. time.

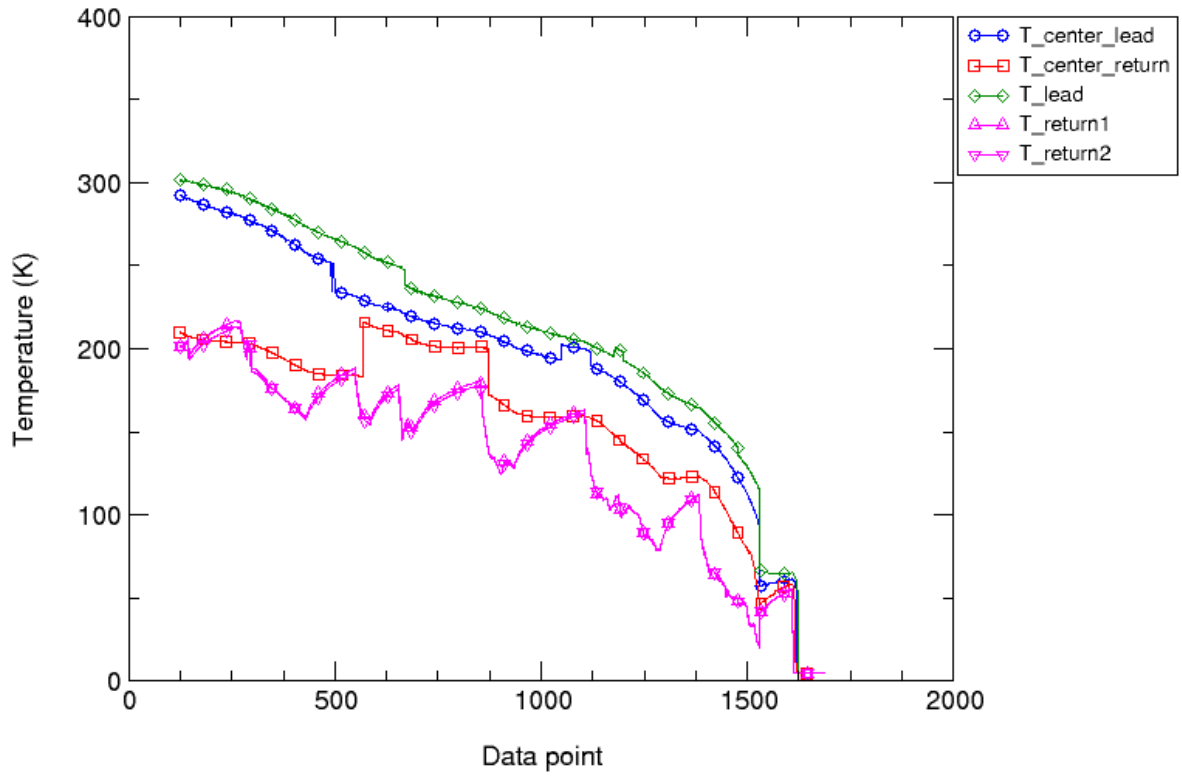


Fig. 50. Temperature of the shell measured during cool-down vs. data point.

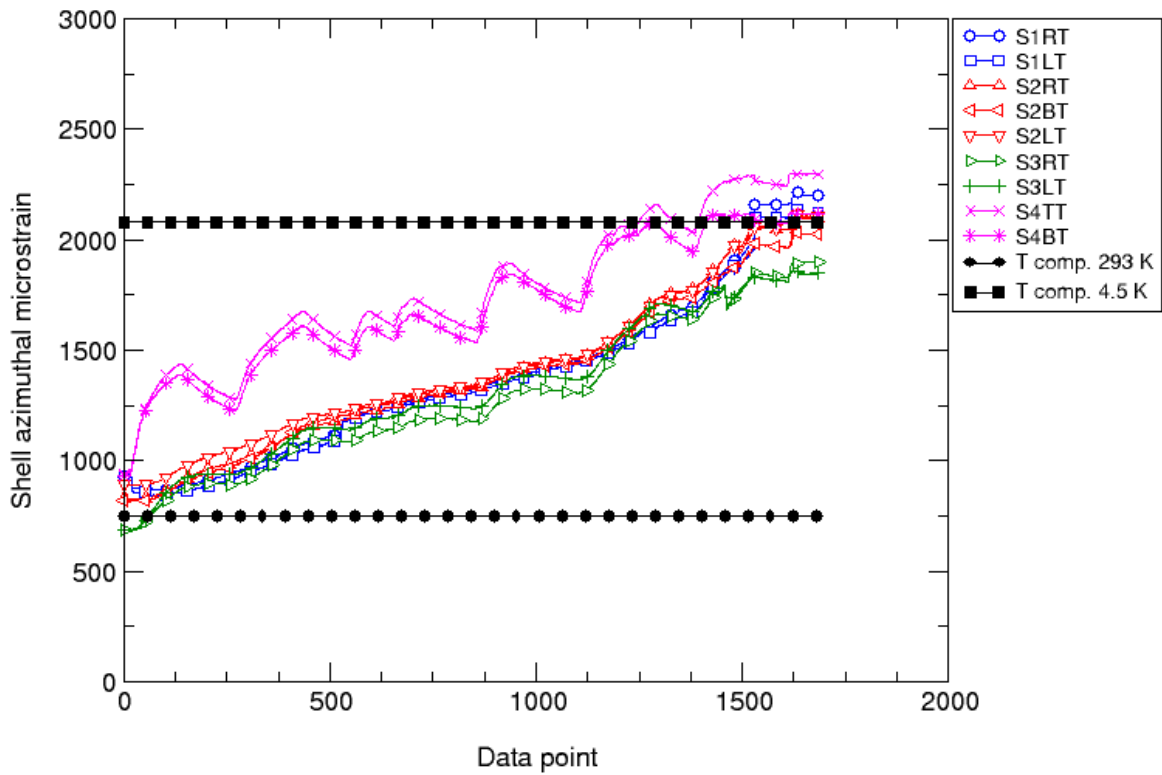


Fig. 51. Azimuthal microstrain in the shell during cool-down: values measured (colored markers) and computed (black markers) from a 3D finite element model.

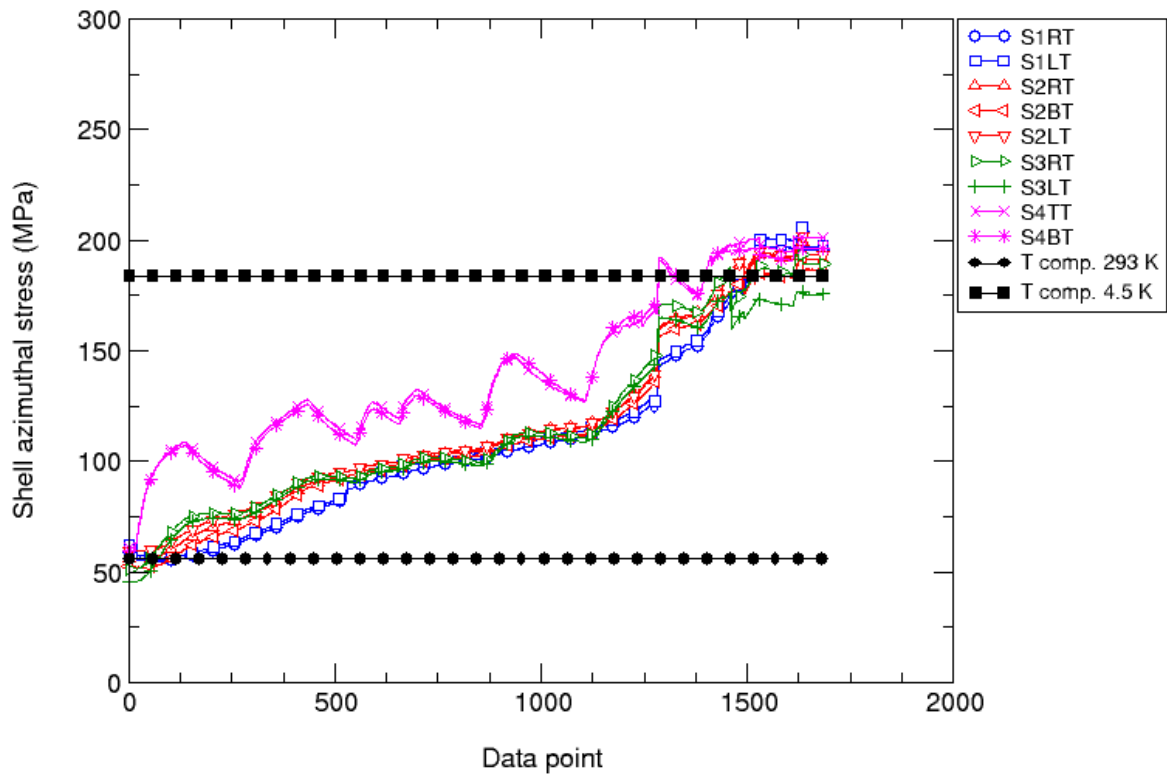


Fig. 52. Azimuthal stress (MPa) in the shell during cool-down: values measured (colored markers) and computed (black markers) from a 3D finite element model.

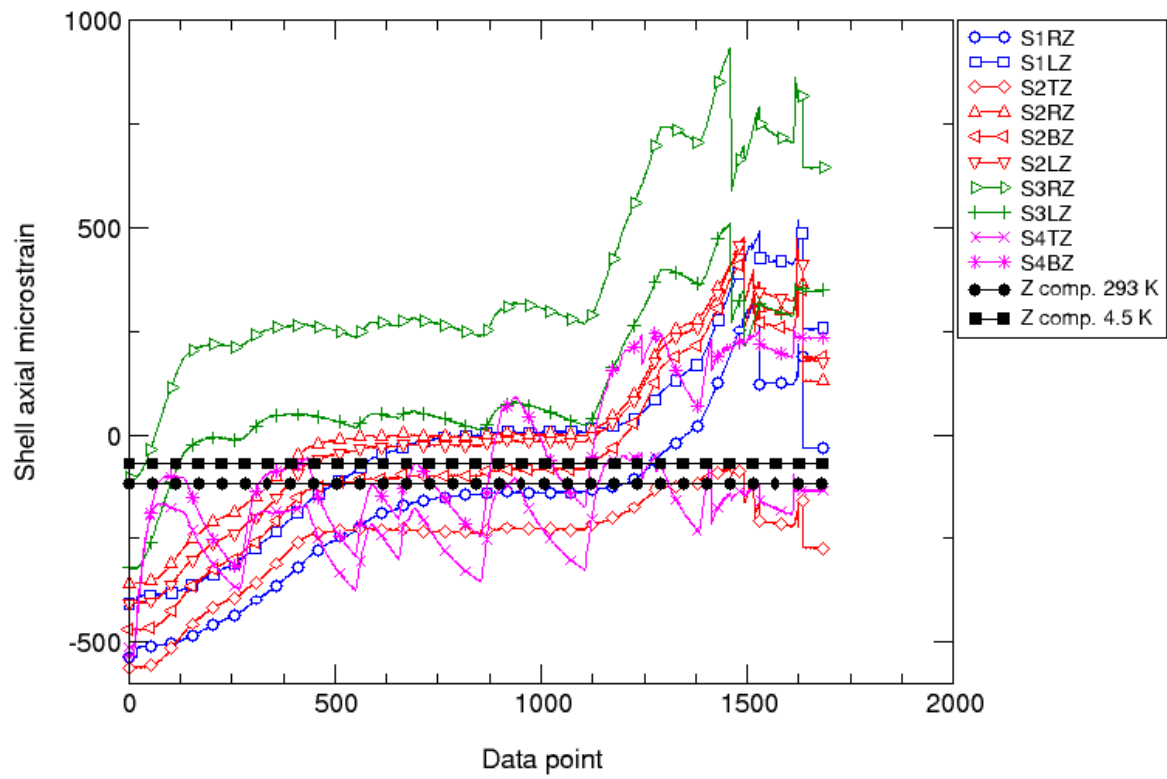


Fig. 53. Axial microstrain in the shell during cool-down: values measured (colored markers) and computed (black markers) from a 3D finite element model.

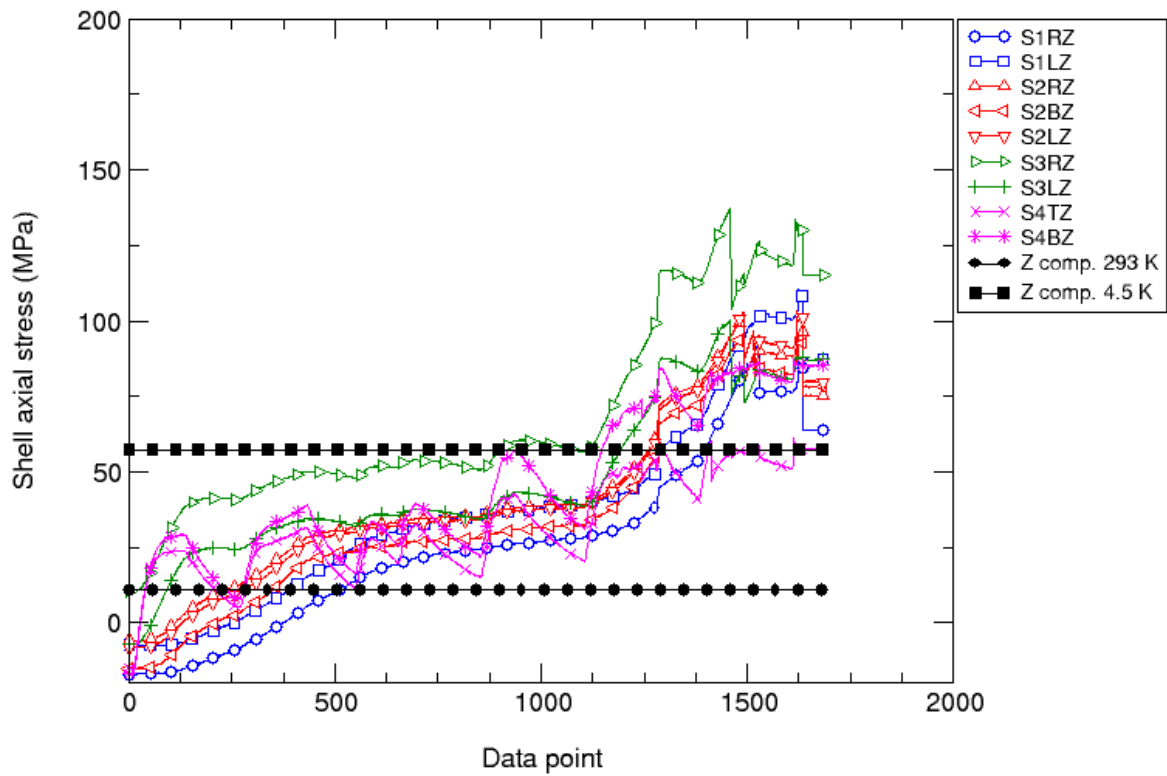


Fig. 54. Axial stress (MPa) in the shell during cool-down: values measured (colored markers) and computed (black markers) from a 3D finite element model.

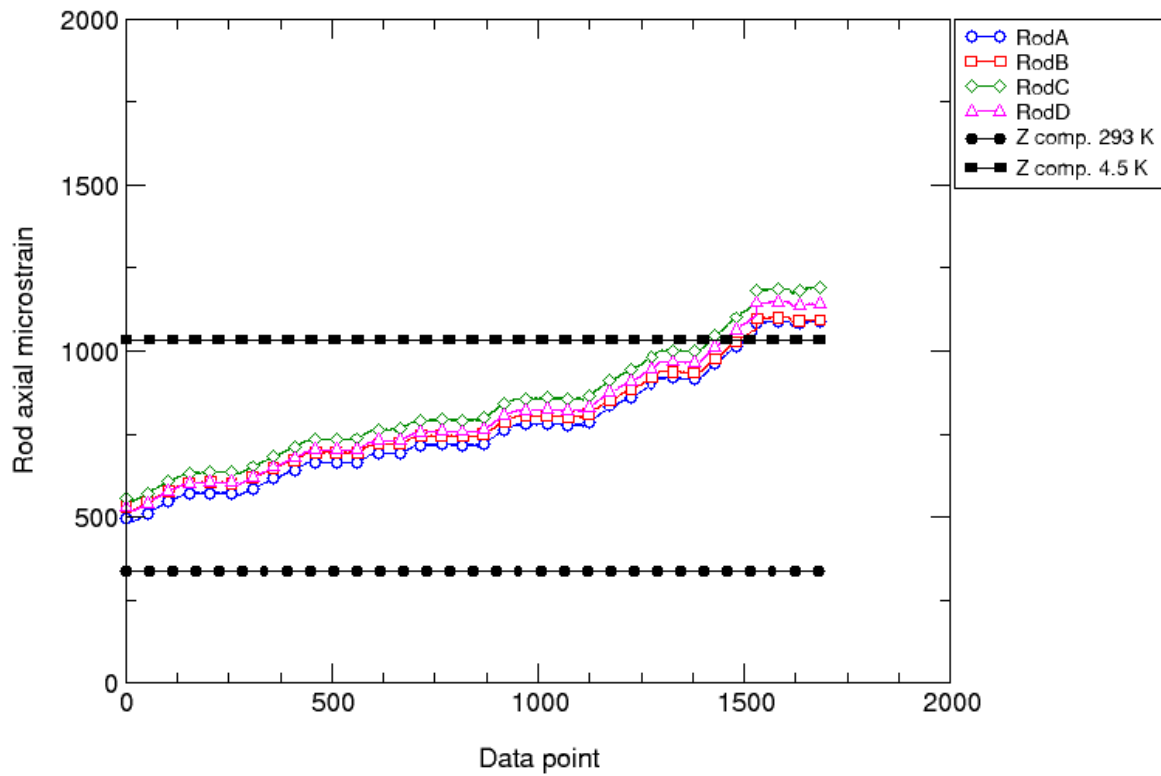


Fig. 55. Axial microstrain in the rods during cool-down: values measured (colored markers) and computed (black markers) from a 3D finite element model.

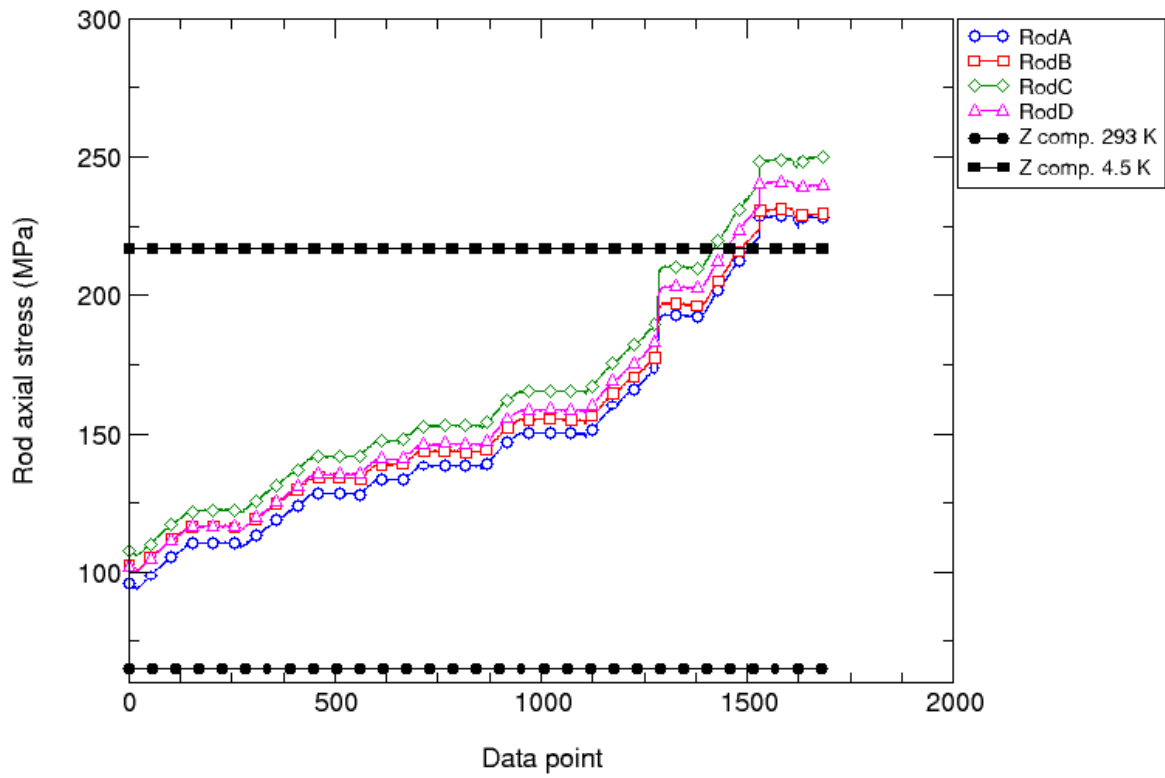


Fig. 56. Axial stress (MPa) in the rods during cool-down: values measured (colored markers) and computed (black markers) from a 3D finite element model.

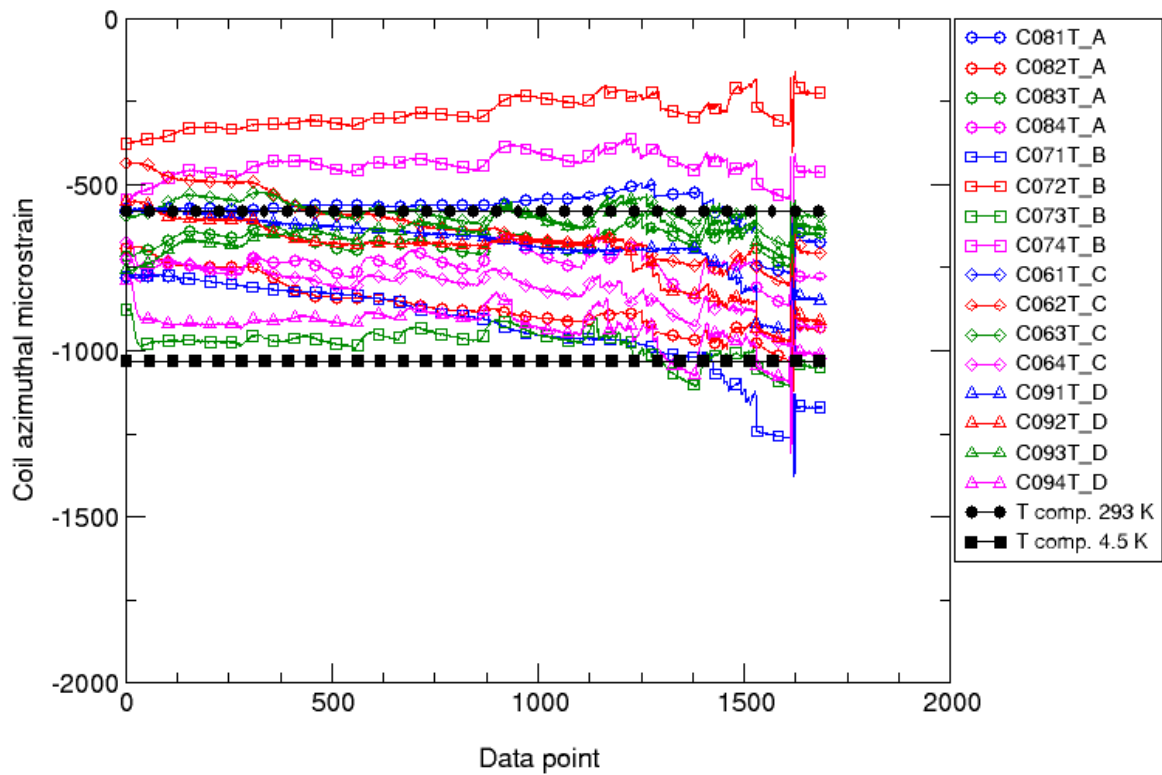


Fig. 57. Azimuthal microstrain in the coil poles during cool-down: values measured (colored markers) and computed (black markers) from a 3D finite element model.



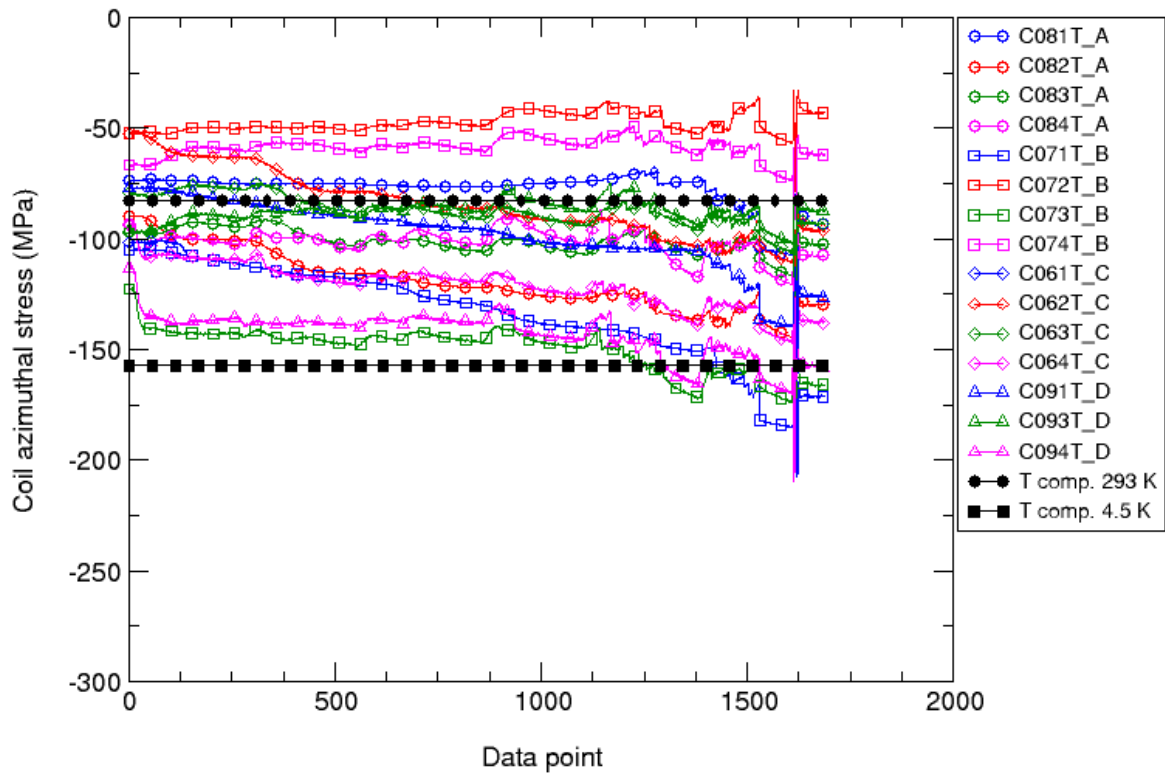


Fig. 58. Azimuthal stress (MPa) in the coil poles during cool-down: values measured (colored markers) and computed (black markers) from a 3D finite element model.

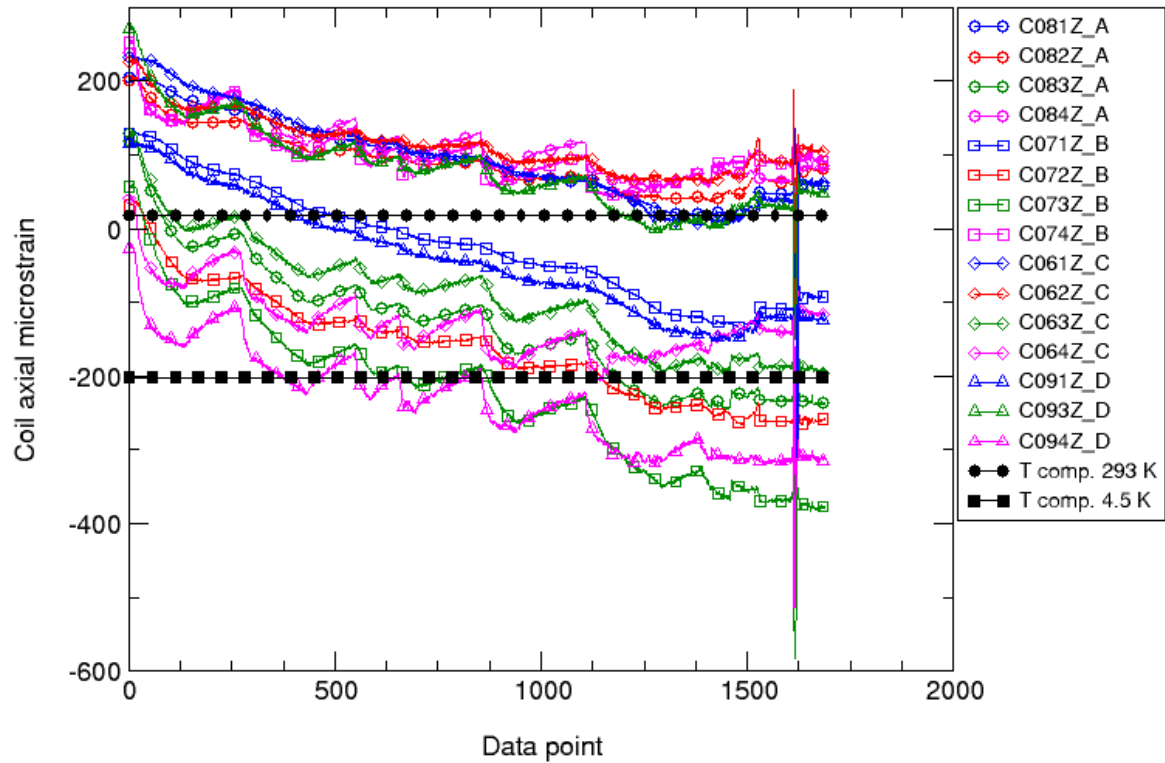


Fig. 59. Axial microstrain in the coil poles during cool-down: values measured (colored markers) and computed (black markers) from a 3D finite element model.

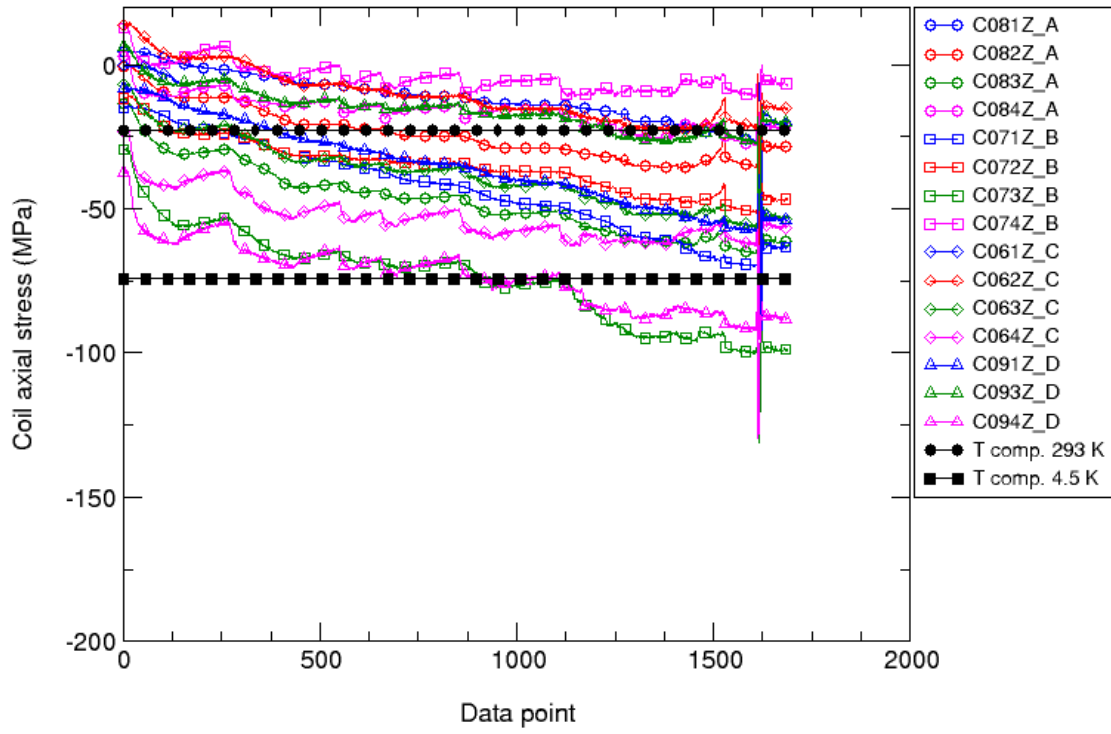


Fig. 60. Axial stress (MPa) in the coil poles during cool-down: values measured (colored markers) and computed (black markers) from a 3D finite element model.

## 8.5 Excitation second thermal cycle

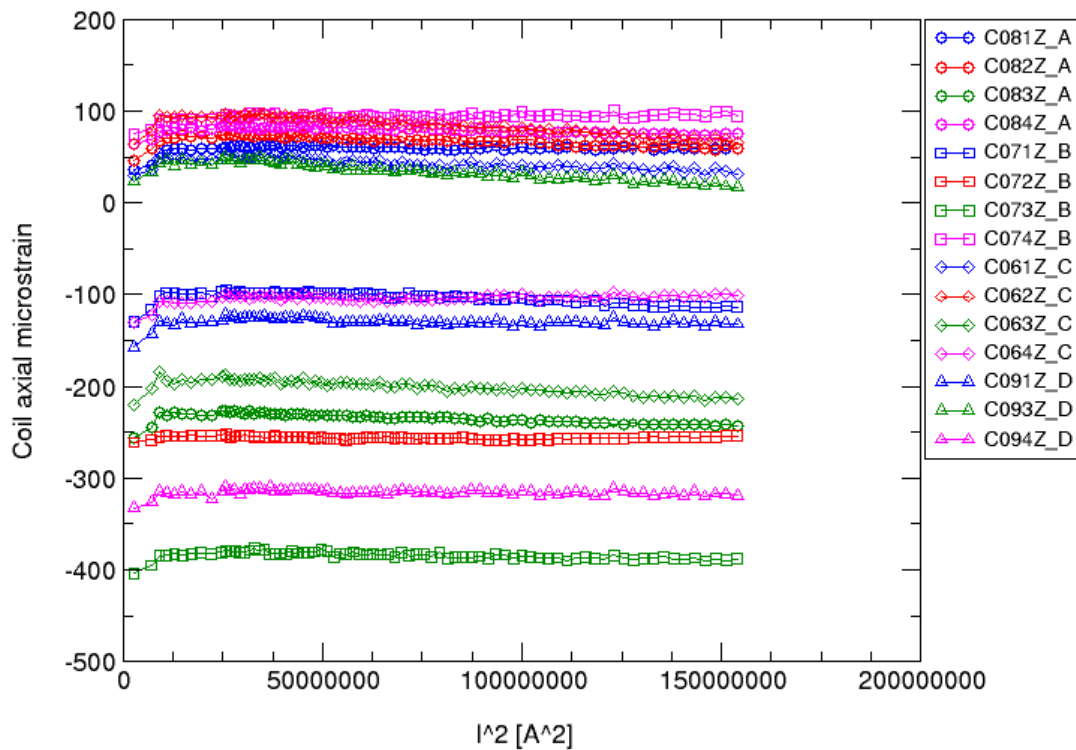


Fig. 61. Axial strain in the coil poles (all stations) vs.  $I^2$  (A<sup>2</sup>) for quench # 48 (12593 A).

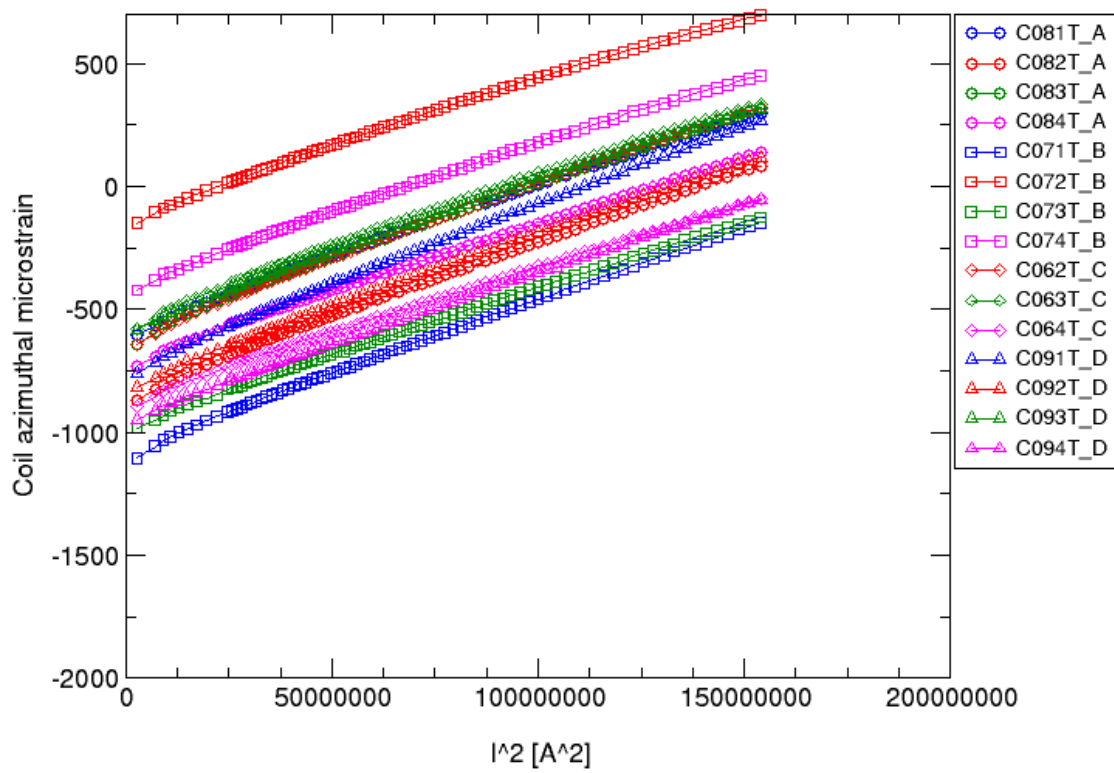


Fig. 62. Azimuthal strain in the coil poles (all stations) vs.  $I^2$  (A<sup>2</sup>) for quench # 48 (12593 A).

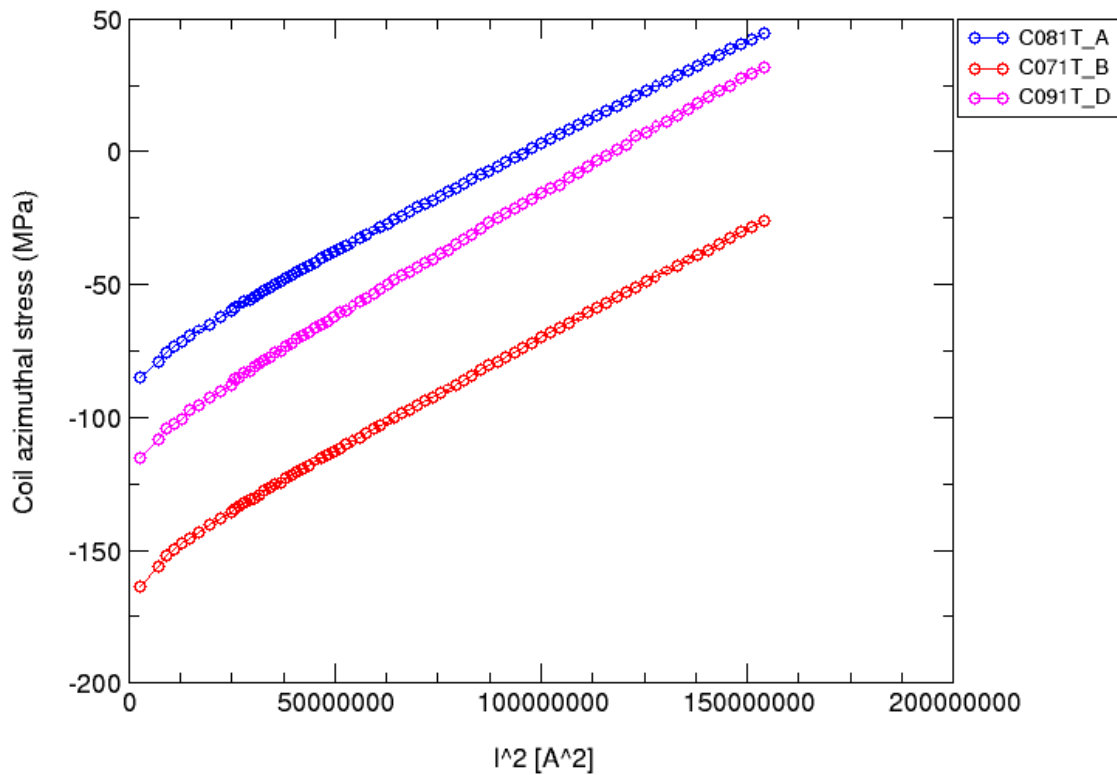


Fig. 63. Azimuthal stress (MPa) in the coil poles (station 1) vs.  $I^2$  (A<sup>2</sup>) for quench # 48 (12593 A).

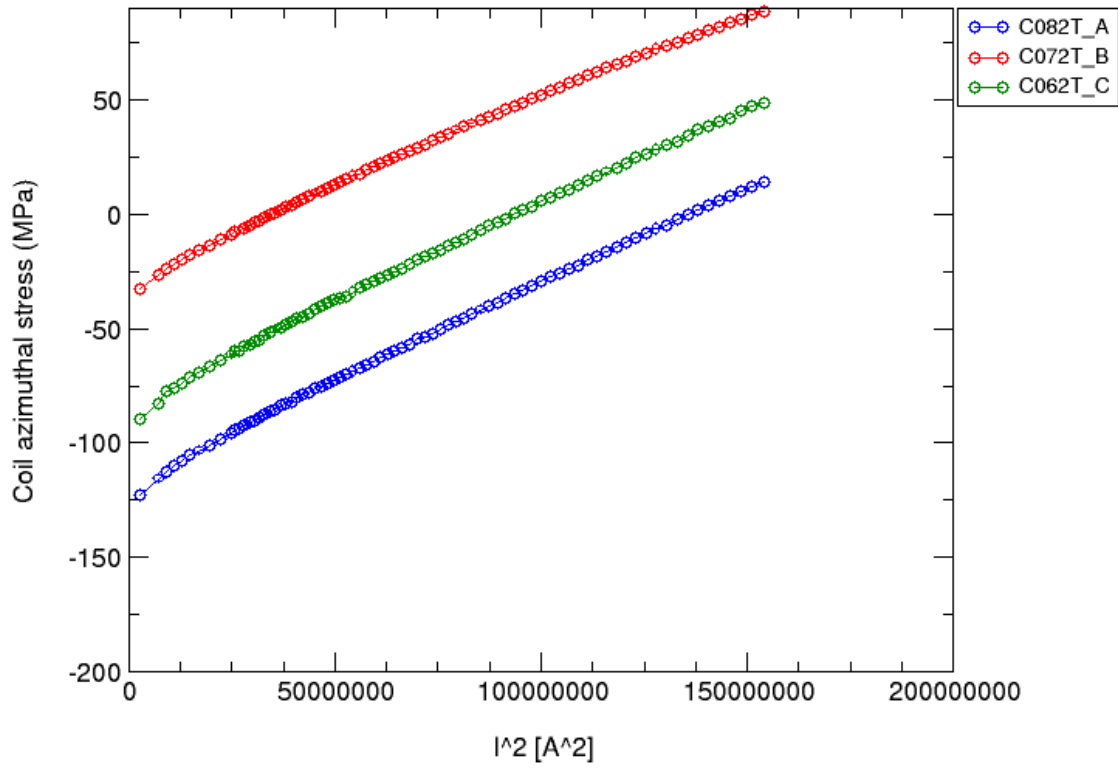


Fig. 64. Azimuthal stress (MPa) in the coil poles (station 2) vs.  $I^2$  (A<sup>2</sup>) for quench # 48 (12593 A).

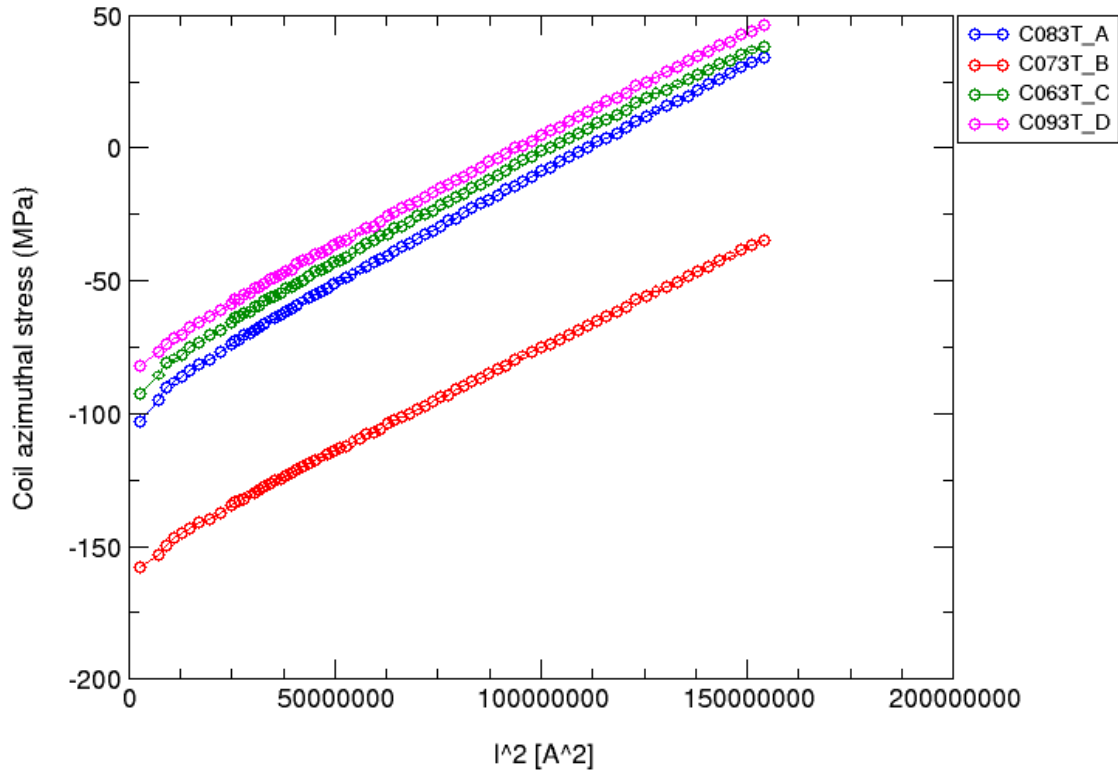


Fig. 65. Azimuthal stress (MPa) in the coil poles (station 3) vs.  $I^2$  (A<sup>2</sup>) for quench # 48 (12593 A).

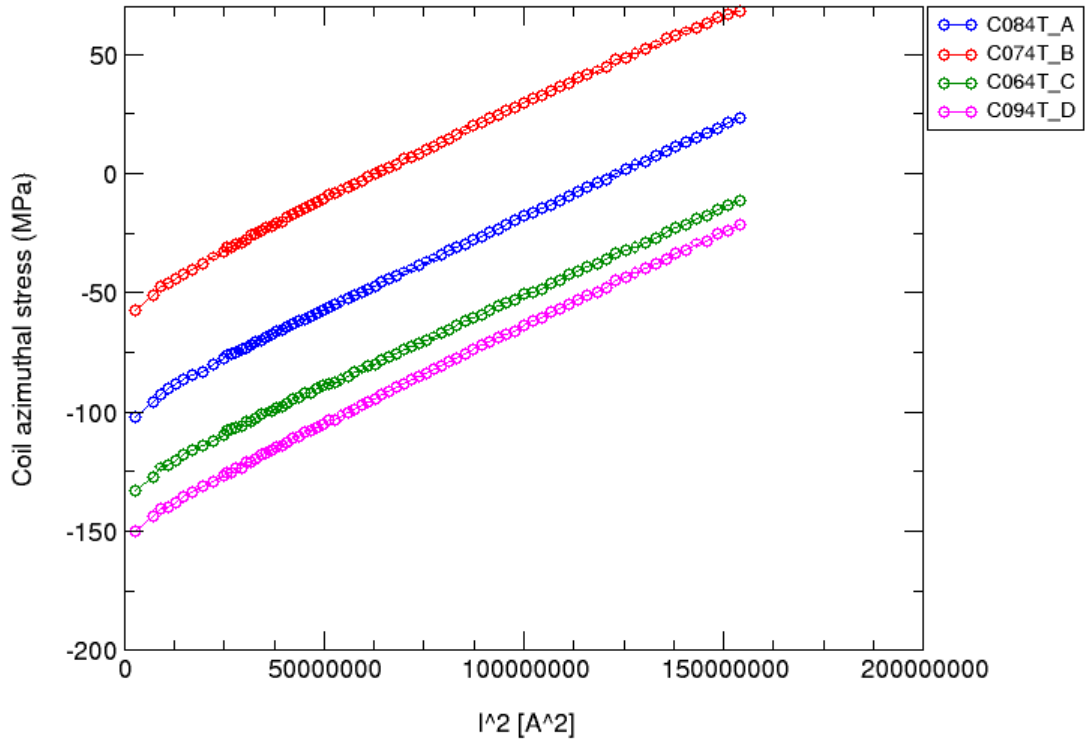


Fig. 66. Azimuthal stress (MPa) in the coil poles (station 4) vs.  $I^2$  (A<sup>2</sup>) for quench # 48 (12593 A).

## 8.6 Warm-up second thermal cycle

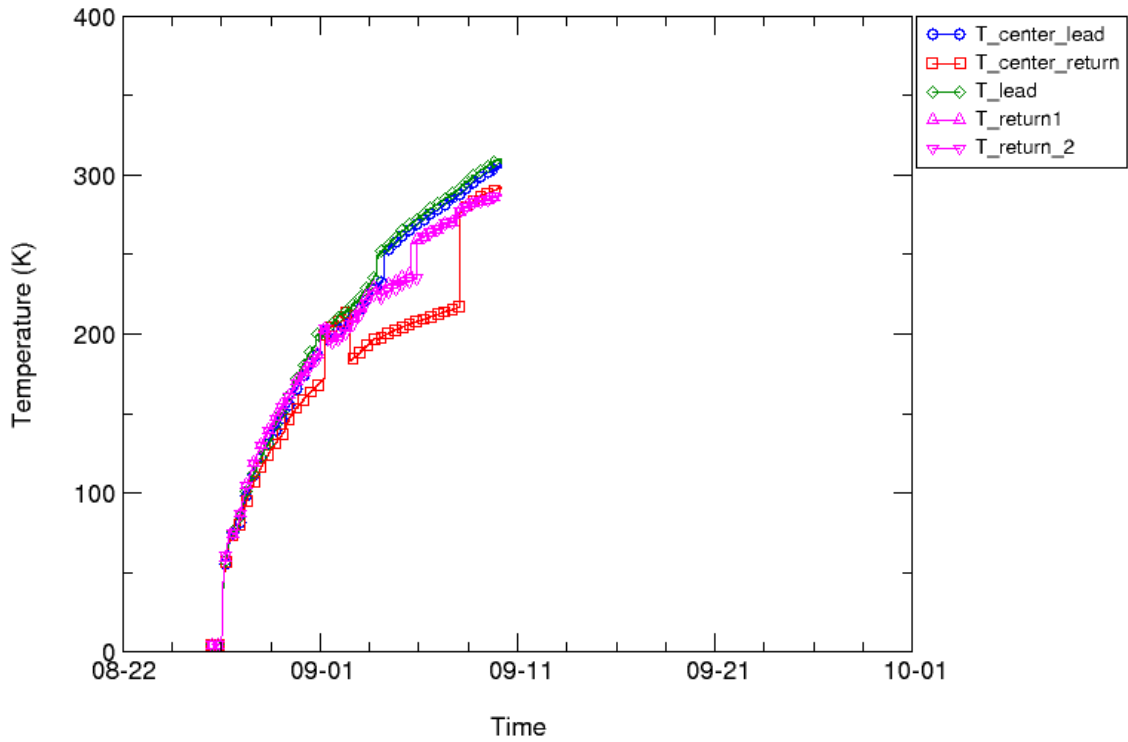


Fig. 67. Temperature of the shell measured during warm-up vs. time.

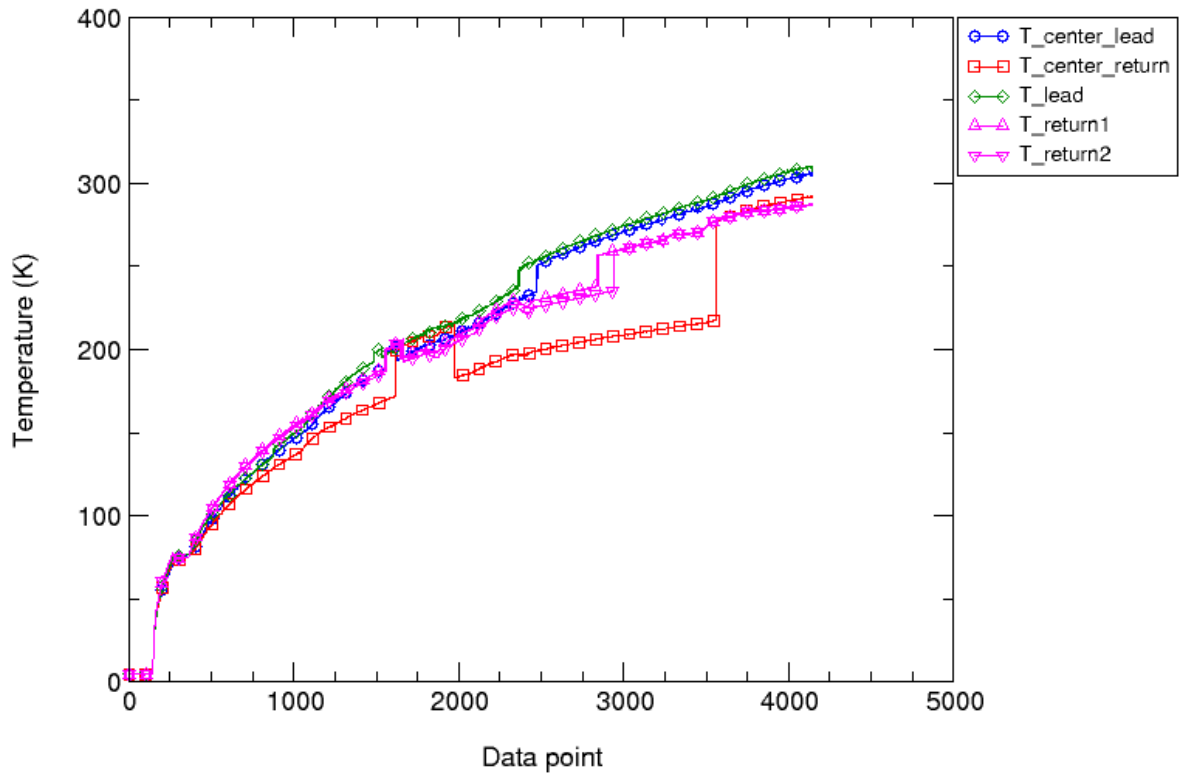


Fig. 68. Temperature of the shell measured during warm-up vs. data point.

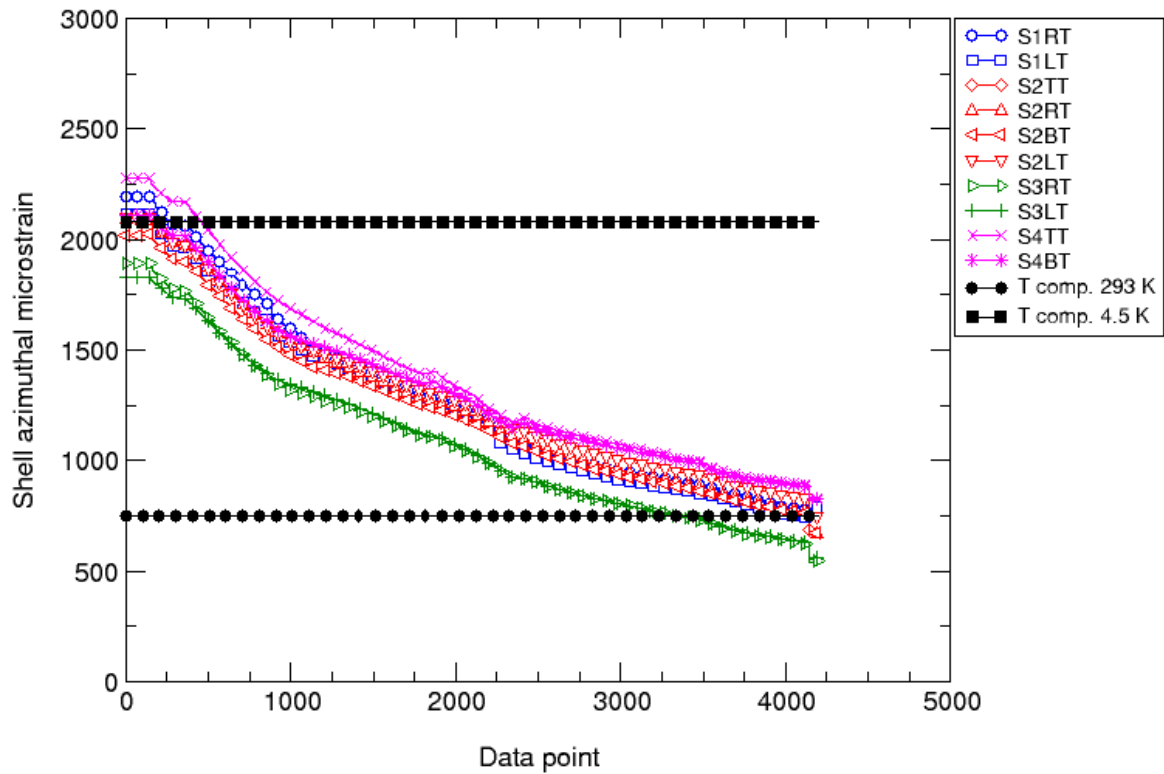


Fig. 69 Azimuthal microstrain in the shell during warm-up: values measured (colored markers) and computed (black markers) from a 3D finite element model.

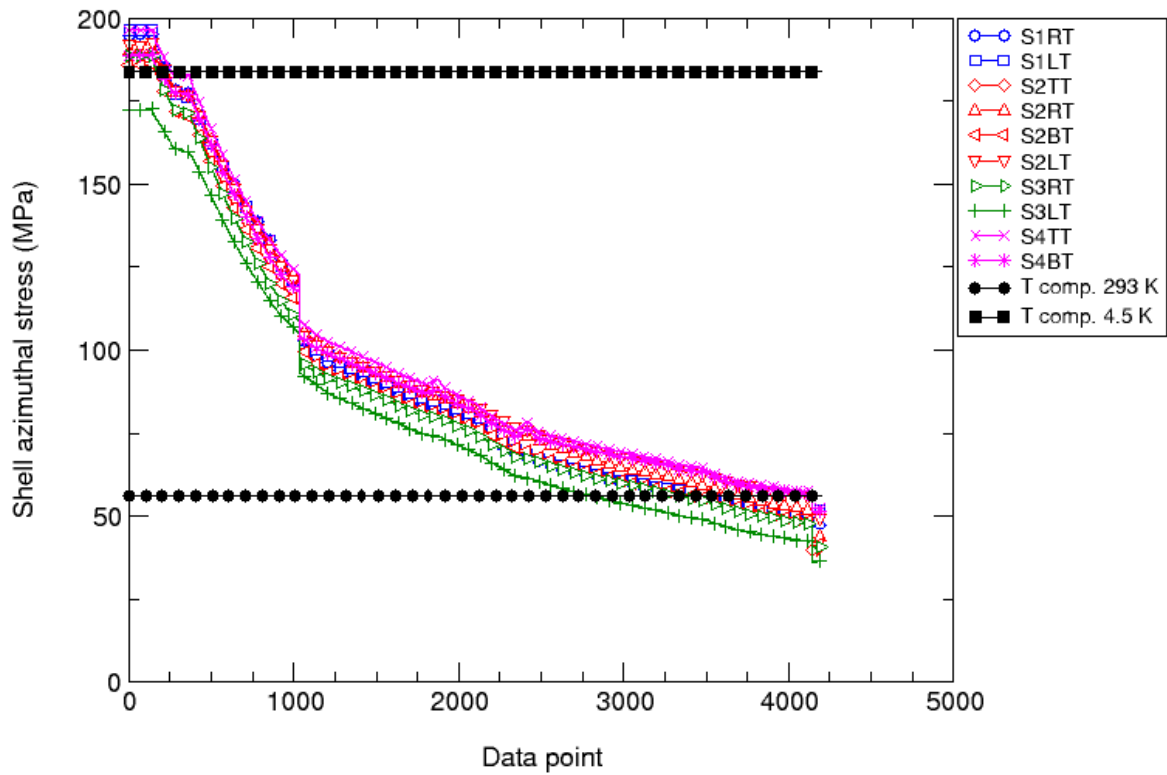


Fig. 70. Azimuthal stress (MPa) in the shell during warm-up: values measured (colored markers) and computed (black markers) from a 3D finite element model.

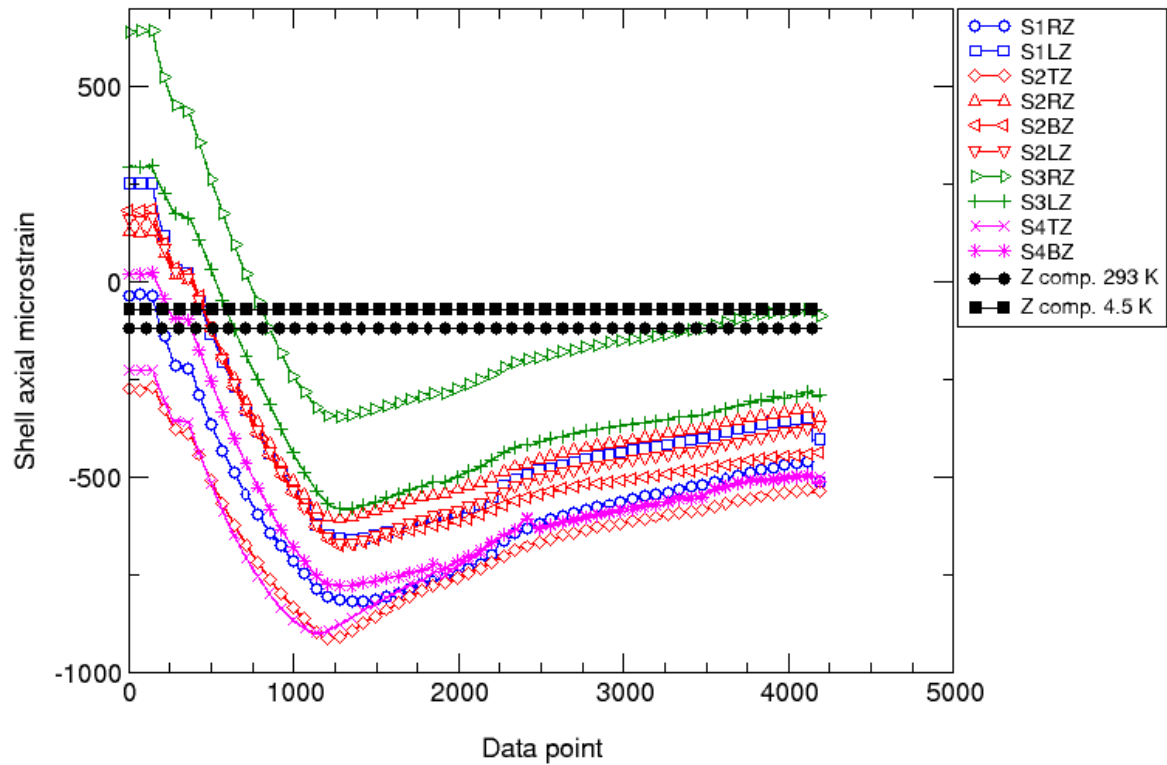


Fig. 71. Axial microstrain in the shell during warm-up: values measured (colored markers) and computed (black markers) from a 3D finite element model.

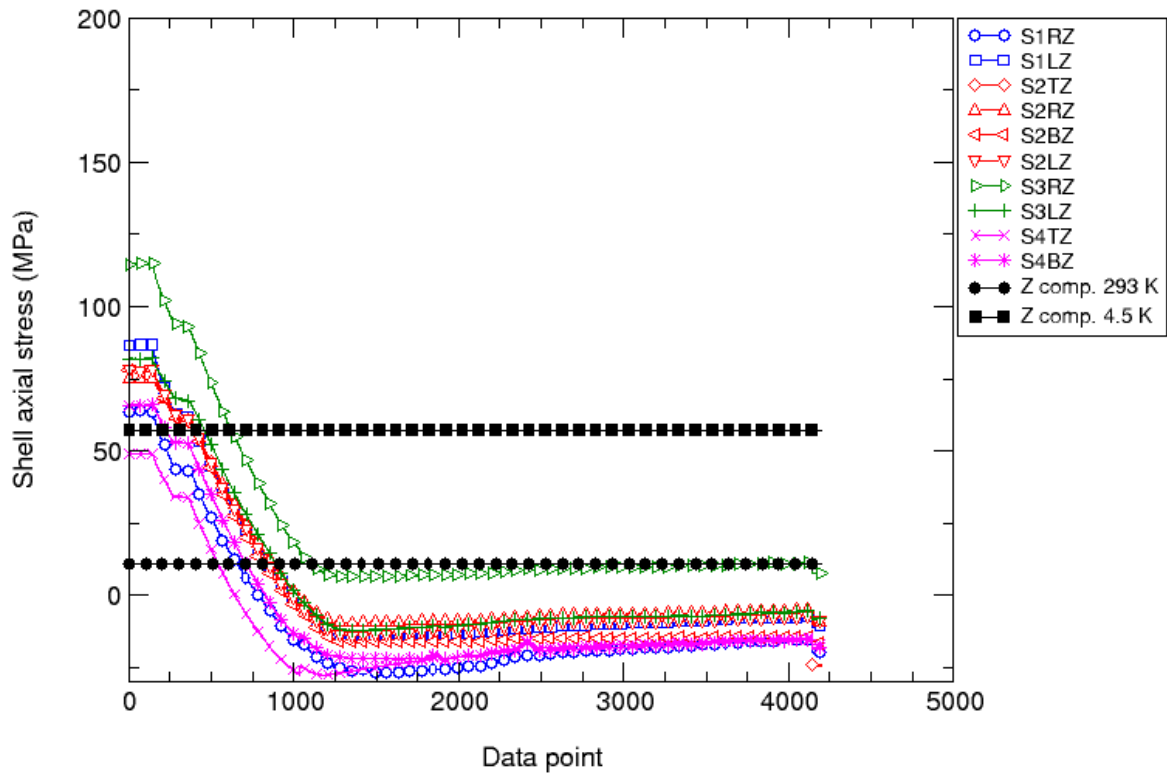


Fig. 72. Axial stress (MPa) in the shell during warm-up: values measured (colored markers) and computed (black markers) from a 3D finite element model.

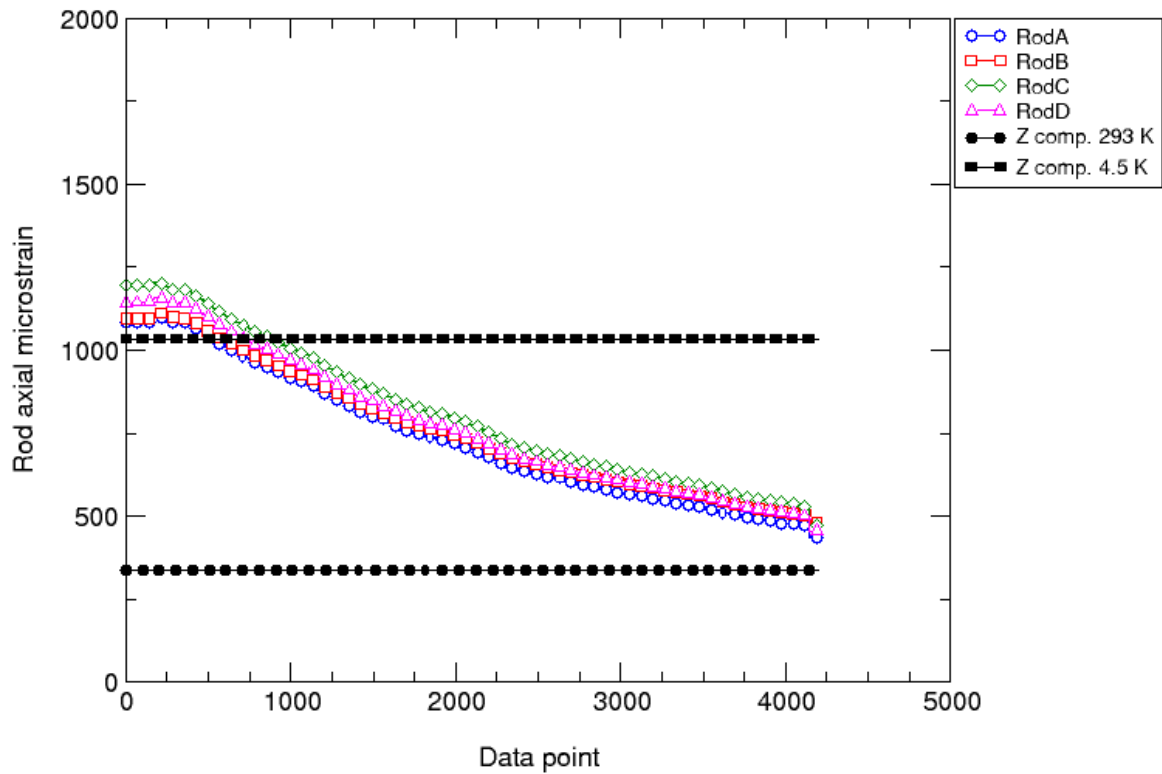


Fig. 73. Axial microstrain in the rods during warm-up: values measured (colored markers) and computed (black markers) from a 3D finite element model.



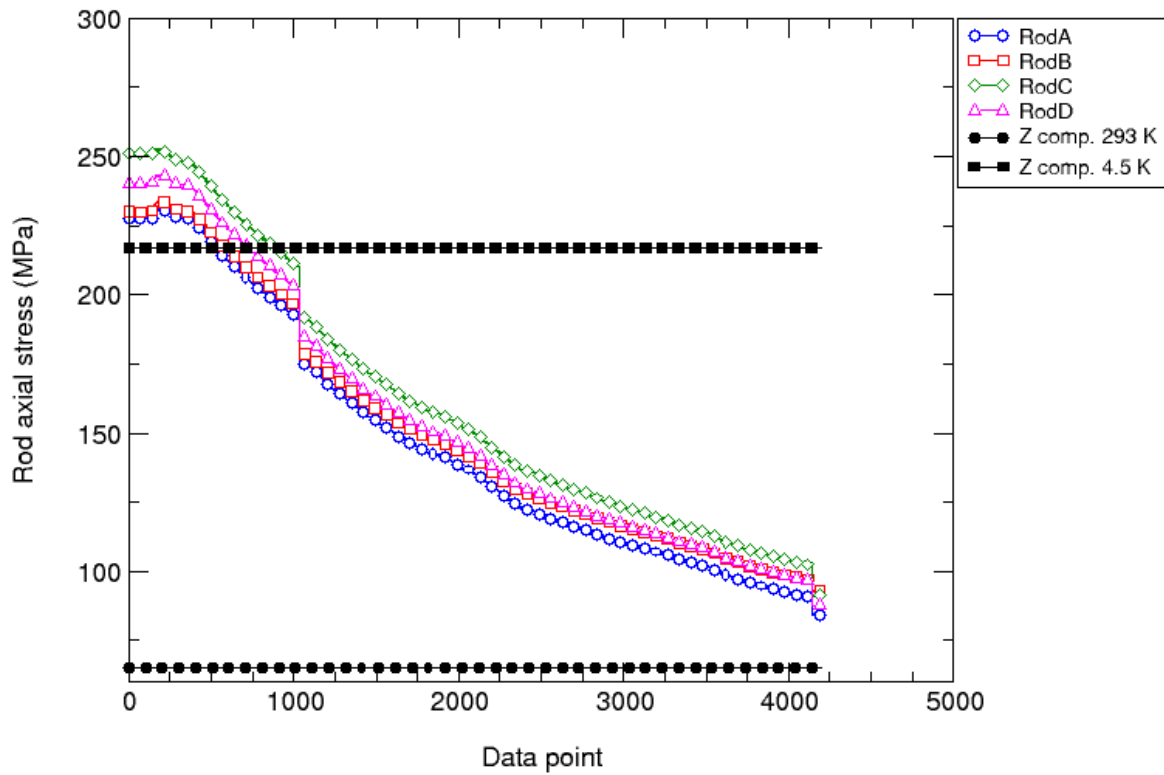


Fig. 74. Axial stress (MPa) in the rods during warm-up: values measured (colored markers) and computed (black markers) from a 3D finite element model.

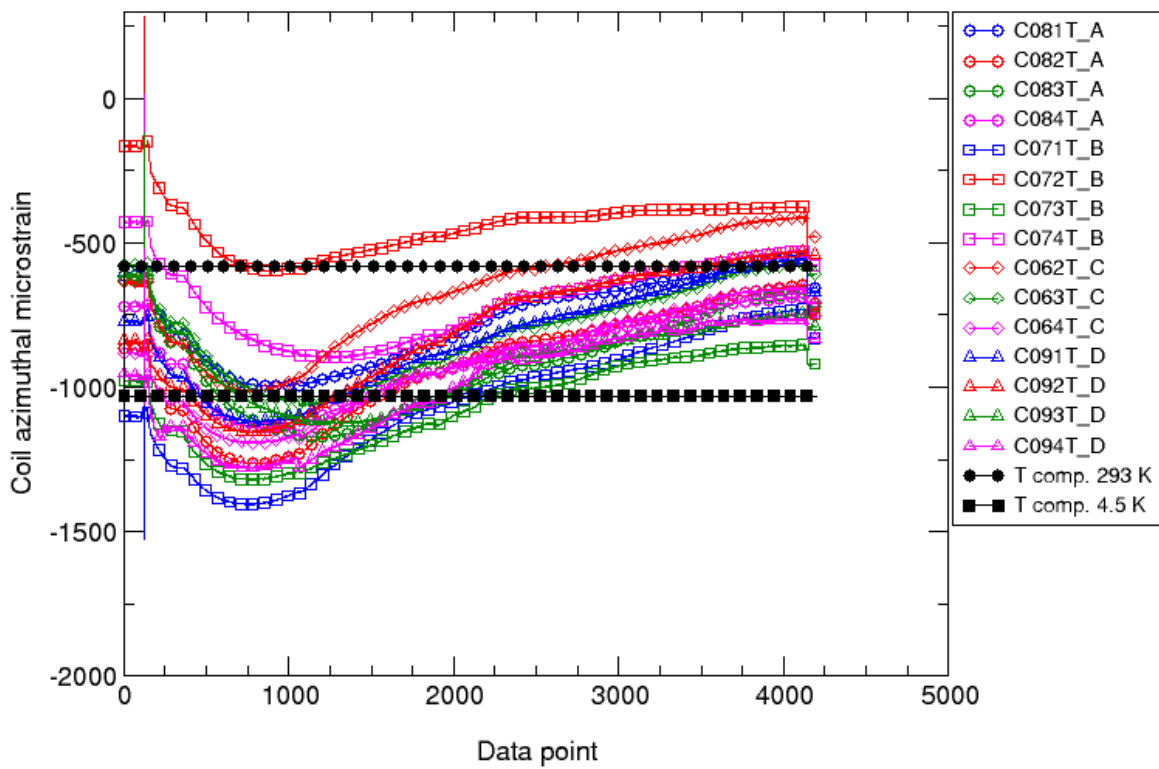


Fig. 75. Azimuthal microstrain in the coil poles during warm-up: values measured (colored markers) and computed (black markers) from a 3D finite element model.

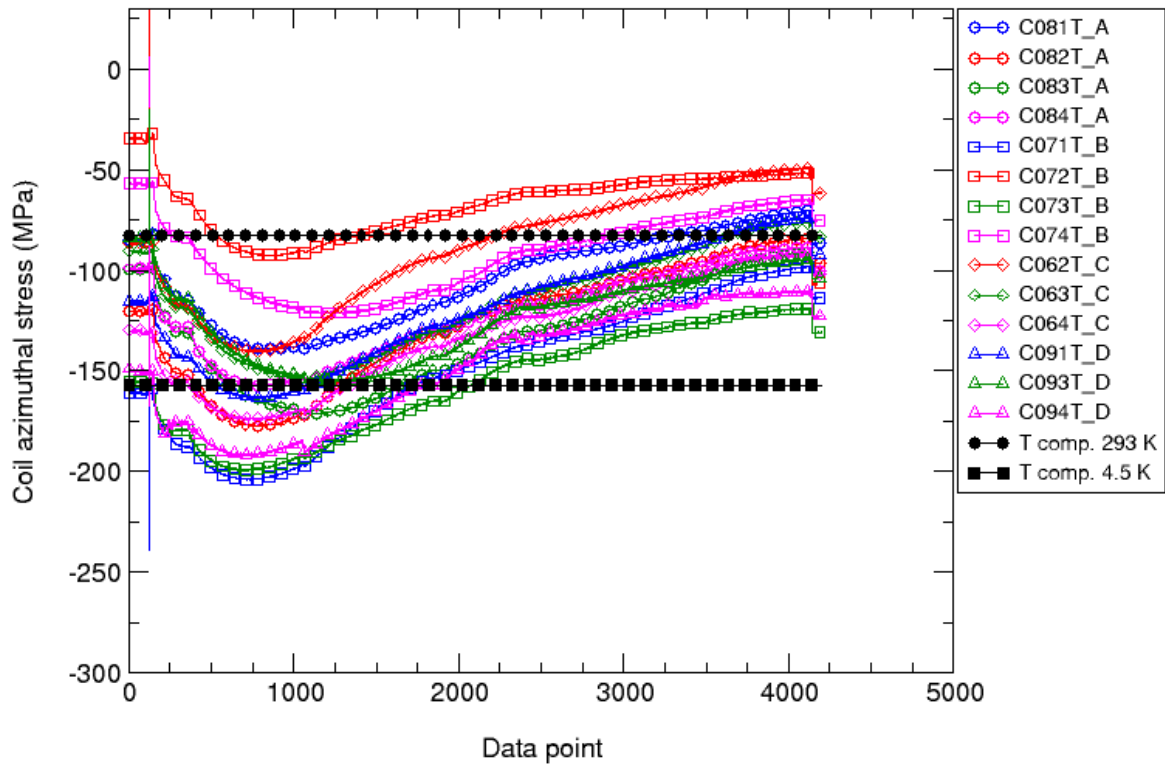


Fig. 76. Azimuthal stress (MPa) in the coil poles during warm-up: values measured (colored markers) and computed (black markers) from a 3D finite element model.

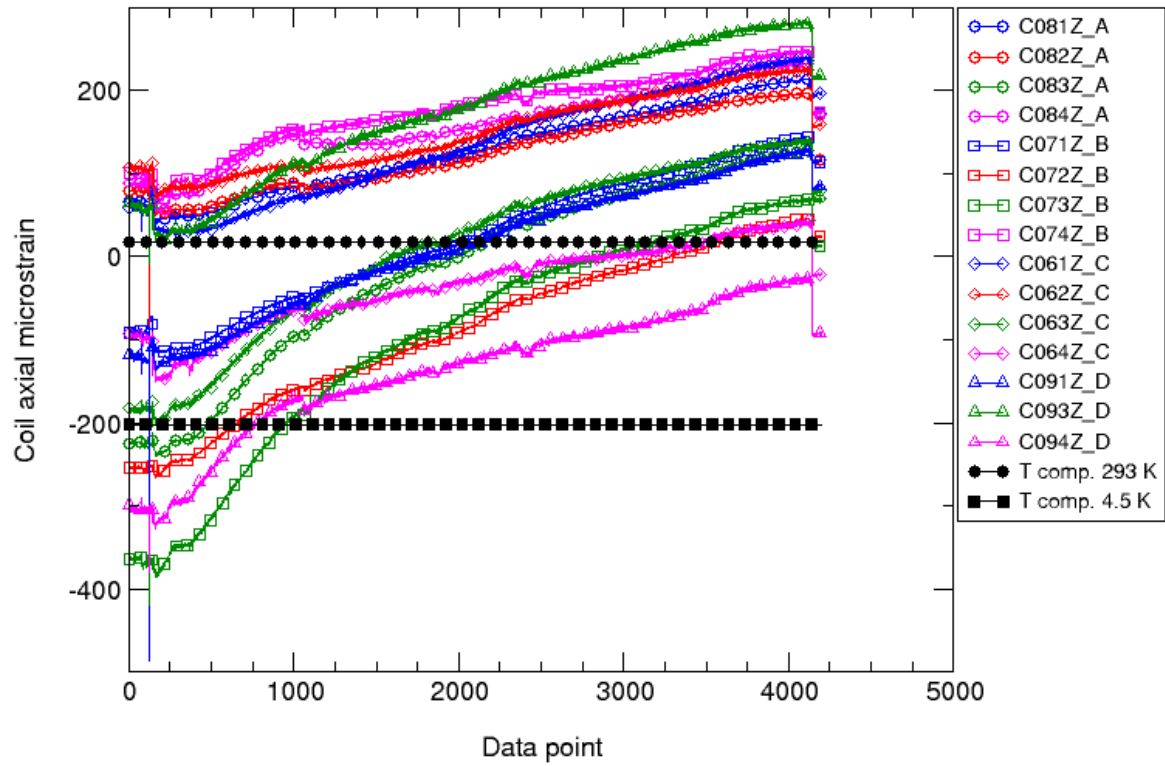


Fig. 77. Axial microstrain in the coil poles during warm-up: values measured (colored markers) and computed (black markers) from a 3D finite element model.

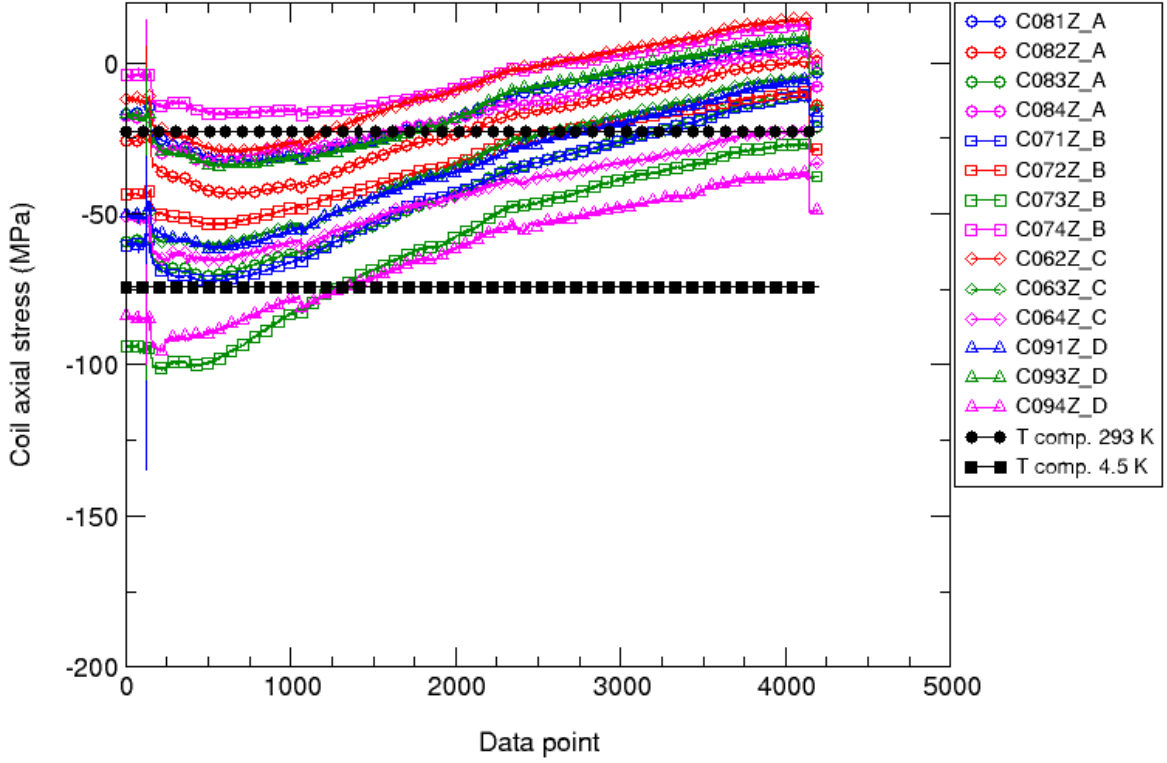


Fig. 78. Axial stress (MPa) in the coil poles during warm-up: values measured (colored markers) and computed (black markers) from a 3D finite element model.

## 9. Magnetic Measurements

Results of field quality measurements are expressed in terms of harmonic coefficients defined in a series expansion given by

$$B_y + iB_x = B_2 10^{-4} \sum_{n=1}^{\infty} (b_n + ia_n) \left( \frac{x + iy}{r_0} \right)^{n-1} \quad (1)$$

where  $B_x$  and  $B_y$  in (1) are the field components in Cartesian coordinates,  $b_n$  and  $a_n$  are the 2n-pole normal and skew coefficients at the reference radius  $r_0$  of 22.5 mm.

Probe centering is done using the standard technique of zeroing the dipole component assuming that it is purely generated from a probe offset in the quadrupole field. The right-handed measurement coordinate system is defined with the z-axis at the center of the magnet aperture and pointing from return to lead end.

The magnetic measurements were performed at the Fermilab Vertical Magnet Test Facility (VMTF) at 4.5 K. For the test, we utilized two tangential-type rotating coil probes with a similar geometry and different lengths of approximately 0.1 and 0.8 m. Each probe consists of 2 dipole, 2 quadrupole and 1 tangential windings. The radius of the probes (1.95 cm) was optimized to the diameter of the LHC warm bore used in this test. Because of the limited length of the warm bore, the probes could not reach the return end of the magnet. For the first measurement point, labeled as a position 1, the 0.8-m (0.1-m) probe center was located at ~8 cm (~44 cm) above the magnet geometrical center.

The positive direction of the z-axis for the scans is pointing from the magnet center to the lead end, from which the probe was inserted. Each measurement contains data from at least ~180 full rotations of the probe.

The cold magnetic measurement program was performed at 4.5 K only and consisted of the following measurements:

- Pre-quench Z-scans, from the magnet center to the lead end, at 6.5 kA,
- Z-scans at 12.3 Tm/m (LHC injection, estimated to be 0.655 kA), 100 Tm/m (estimated to be 5.3 kA) and 200 Tm/m (~11 kA). Measurements at 3 kA, 4.5 kA and 8 kA.
- Eddy current loops with the ramp rates 20 A/s, 40 A/s and 80 A/s up to 9.0 kA with the probe positioned in the center of the magnet.
- Dynamic effects measurement, which included a current accelerator profile, similar to the one used in LHC LQXB quads (15 min. duration of the injection plateau and the probe positioned in the center of the magnet).
- A stair step measurement, stopping 2 min at 1.5, 2, 4, 6, 8 and 9 kA and back.

Results of field quality measurements of technology magnets TQS are also presented for comparison.

### 9.1 Transfer Function and Geometrical Harmonics

The measured transfer functions (TF) in the magnets versus the excitation current is shown in Fig. 79. The loops are executed with ramp rate of 20 A/s. TQS and LQS, show a distinguishable similar pattern, which is determined from the iron characteristics. For example, one can see that TQS starts to saturate around 2.0-2.2 kA. For LQS, we could not perform full loops because of the conductor instability at low ramp rates and low currents [7]. Moreover, we observed good agreement, bellow 0.2%, between the measured and calculated values. For comparison, we plot an example of the measured and calculated TF for a TQC-type model (TQC02E). Due to the collared coil structure in the magnets, the effect of saturations occurs much higher, after 7 kA (see Fig. 79, dashed line and open points).

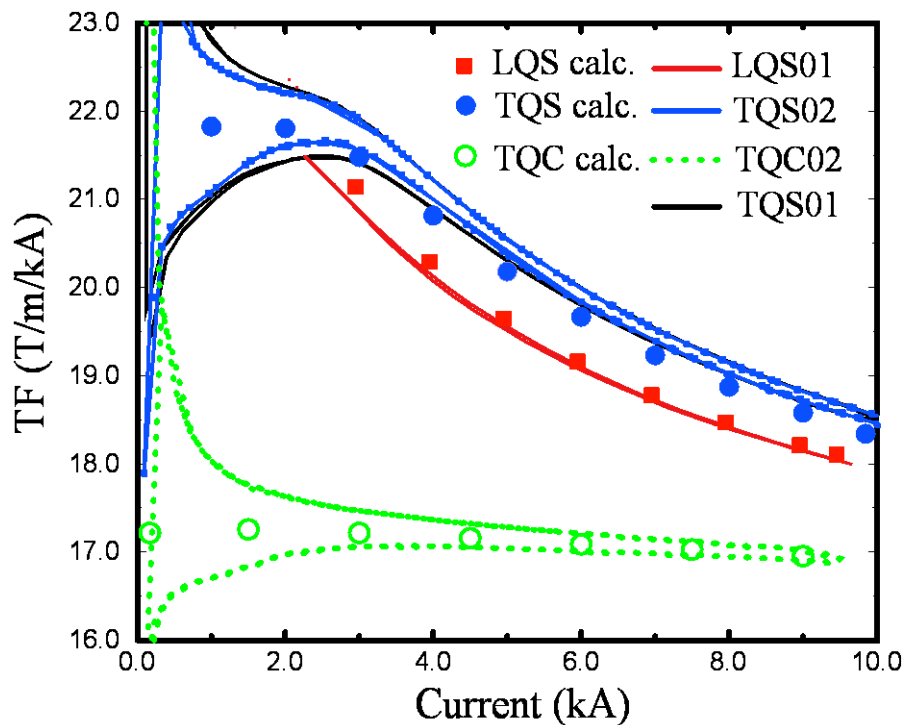


Fig. 79. Transfer functions for the magnets vs. the excitation current. The filled and open dots represent the calculations for TQS and TQC respectively. For comparison, the TQC02 TF is plotted too (dashed line).

Table 5 compares the average geometrical harmonics in the TQS and LQS magnets at 45 T/m (approximately 2.6 kA). At this gradient, the field penetrates fully in the superconductor and it is still below the iron saturation. Thus, we minimized the errors associated with these effects and possible imperfection in their simulation. Although achieving a particularly good field quality was not a TQS and LQS program target, one can see that harmonics differ from calculations [8] by less than ~6.2 units (normal octupole).

Table 6 compares the average harmonics measured at a current ramp up for LQS01 and TQS models at 12.3 T/m (LHC injection field), 100 T/m and 200 T/m (11 kA), close to the LHC IR quadrupole collision field. One may conclude, that except for the octupole and dodecapole during the injection, which should be corrected for the next step the program, LQS01 is practically an accelerator type quality magnet. The reason for such octupole in LQS01 is most likely due to a deviation of the magnet aperture from circular to elliptical. The  $b_4$  was not observed in the 1-m long TQS-TQC models. In LQS01 it may be generated during magnet assembly and/or by small differences in coil pairs fabricated with different fixtures (two sets of reaction and impregnation fixtures were used to make two LQ coils each, and coils made with the same set were placed facing each other during LQS01 and LQS01b assembly). This deviation will be addressed during next LQ assemblies.

**Table 5 Calculated and Measured TQS and LQS Harmonics**

$b_n \ a_n$	TQS			LQS	
	calc.	measured		calc.	measured
		01	02		
$b_3$	-	-1.46	2.98	-	3.43
$b_4$	-	-0.52	1.31	-	6.20
$b_5$	-	3.06	-1.45	-	-0.16
$b_6$	5.00	5.40	6.23	8.45	10.43
$b_7$	-	0.07	0.05	-	-0.10
$b_8$	-	-0.11	-0.13	-	-0.58
$b_9$	-	0.02	0.10	-	-0.14
$b_{10}$	0.04	0.02	-0.05	-0.03	-0.32
$a_3$	-	4.41	0.66	-	2.11
$a_4$	-	-1.99	0.82	-	1.34
$a_5$	-	0.71	-1.50	-	0.48
$a_6$	-	-0.37	0.12	-	-0.37
$a_7$	-	-0.11	-0.01	-	-0.30
$a_8$	-	-0.18	-0.10	-	-0.09
$a_9$	-	-0.02	0.02	-	-0.55
$a_{10}$	-	0.00	-0.08	-	0.24

**Table 6 TQ and LQS Harmonics at 12.3 T/m, 100 T/m and 200 T/m**

$b_n$ $a_n$	TQS01-02 average			LQS		
	12.3 T/m	100 T/m	200 T/m	12.3 T/m	100 T/m	200 T/m
$b_3$	0.73	0.01	0.06	3.34	2.29	2.61
$b_4$	-1.76	0.27	0.21	7.72	6.73	6.93
$b_5$	-0.88	1.57	0.39	0.06	0.17	-0.08
$b_6$	-11.83	3.83	1.58	-33.31	9.89	7.47
$b_7$	0.06	0.06	0.02	0.05	-0.06	-0.11
$b_8$	0.04	0.00	0.01	-0.28	-0.98	-0.38
$b_9$	0.03	0.02	0.00	0.08	0.19	0.13
$b_{10}$	0.12	0.03	0.00	0.56	0.35	-0.47
$a_3$	0.97	1.94	0.66	2.03	2.28	2.28
$a_4$	-3.70	-0.39	0.82	6.28	1.94	2.11
$a_5$	-0.24	0.30	-1.50	-0.50	-0.51	-0.65
$a_6$	0.13	-0.18	0.12	-1.14	-0.12	-0.29
$a_7$	-0.06	-0.09	-0.01	0.17	0.29	0.14
$a_8$	0.03	-0.10	-0.10	0.12	0.08	0.06
$a_9$	-0.01	-0.01	0.02	-0.29	-1.09	-0.16
$a_{10}$	0.00	-0.00	-0.08	0.05	0.37	0.12

## 9.2 Iron saturation effect

The iron saturation effect was extracted as an average value between up and down ramps of the measured hysteresis loops at 20 A/s and 40 A/s. The calculated and measured iron saturation effect in dodecapole for TQS and LQS magnets is shown in Fig. 80. One can see, that maximum observed dodecapole deviations are in the order of 2 units in LQS01 magnet and 3 units in TQS01-02 in current range from 2 kA to 9 kA. The larger iron saturation effect in these magnets is due to the iron pads placed next to the coil. As was discussed in [9], if it is necessary, the saturation effect can be corrected by introducing holes into appropriate places in iron pads and/or yoke, or by substituting the iron pads with stainless ones.

In comparison, the maximum dodecapole deviation due to the iron saturation in NbTi LHC IR magnets, which have the same iron yoke as TQC models, was approximately 0.2 units at the same fraction of the coil aperture.

## 9.3 Eddy current effect

Current excitation loops have been executed at current ramp rates of 20 A/s, 40 A/s, and 80 A/s for LQS01. Fig. 81 shows the measured dodecapole loops. The dots represent the “stair step” current profile measurement where the duration at every current step was set at 120 s. The measurements were started 5 s later after the current arrived at the plateau and the ramp rate between the steps was selected at level of 5 A/s. In this way, we minimized the possible eddy current effects to the measurement of the dodecapole hysteresis loop. Based on the presented results, one can conclude that LQS01 has relatively large interstrand coupling currents due to the low interstrand resistance. This problem can be solved by

introducing a high resistivity core inside the cable.

The LQS01 and TQS02 (TQC02) magnets had coils of the same design made of the same RRP conductor with larger magnetization that should result in similar coil effects and dodecapole loop widths. Fig. 82 shows the widths of dodecapole  $\Delta b_6 = (b_6^{\text{up ramp}} - b_6^{\text{down ramp}})$  loops at 90 T/m and different ramp rates. As expected, LQS01 and TQS02 show the same behavior, which is somewhat different from TQC02 dependence. This discrepancy could be attributed to the different coil structures. But for all of them, an extrapolation of  $\Delta b_6$  to zero ramp rate is clearly similar and shows larger coil magnetization effect

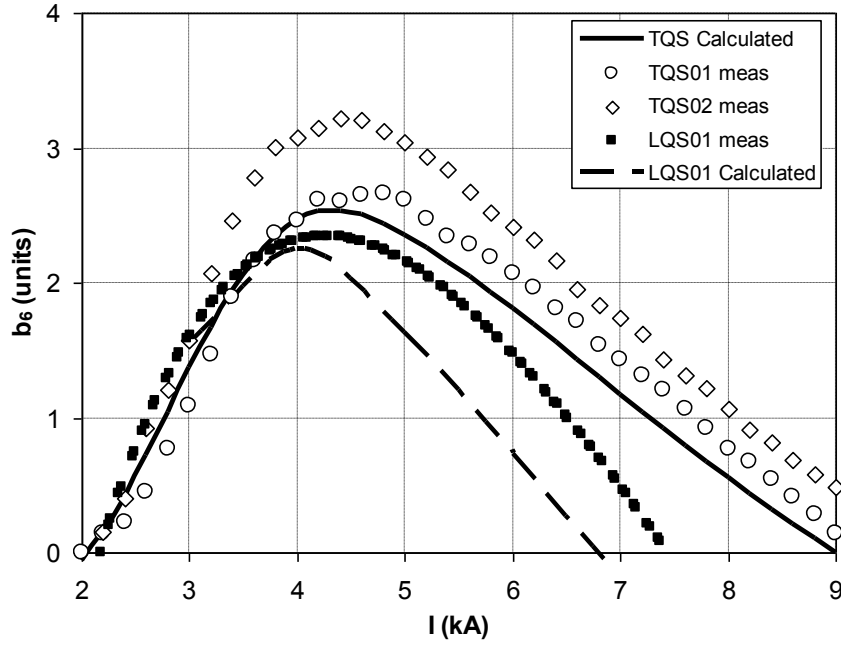


Fig. 80. Iron saturation effect in TQS01-02 and LQS01.

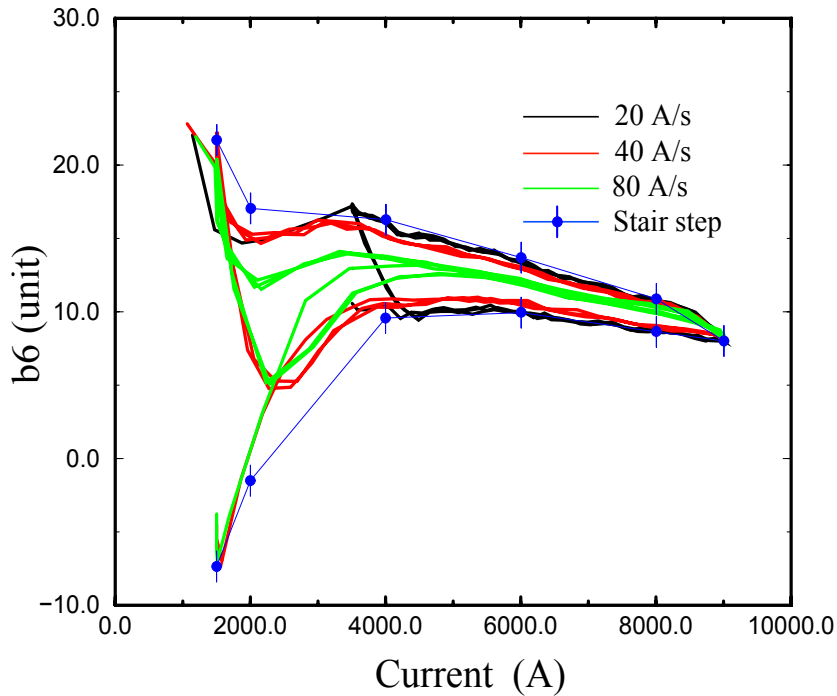


Fig. 81. LQS01 current loops executed at ramp rate of 20 A/s, 40 A/s and 80 A/s. The points represent the “stair step” measurement described in the text.

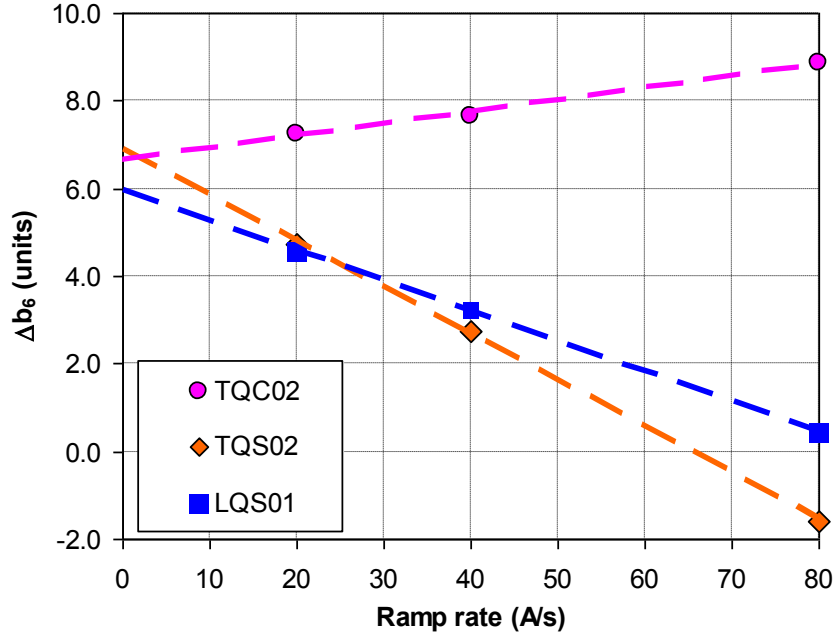


Fig. 82. Dodecapole loop width as function of the ramp rate.

#### 9.4 Long-term Dynamic Effects

Long-term dynamic effects in superconducting magnets play an important role in the operation of modern accelerators. This well-known phenomenon is usually associated with the decay and subsequent snapback of the allowed field components at injection [10]-[11].

To investigate these effects in the LQS01 quadrupole, we performed measurements with an accelerator current profile similar to the one used for the LHC IR quadrupole production tests, performed at Fermilab. The important characteristic of this profile is the duration of the injection plateau, which was set to  $\sim 900$  s. Our measurements were focused on decay and snapback in the normal dodecapole component, the first allowed multipole.

As we expected, the decay and snapback was not observed in LQS01 (Fig. 83). The inset of Fig. 83 shows, in fine scale, the linearity of the dodecapole during the injection plateau. The LQS01 magnet behavior reproduces the results from TQ model quadrupoles [9]. The long-term decay and snap-back was not observed also in Nb<sub>3</sub>Sn dipole model magnets made of similar conductors [12]. In comparison, average amplitude in the NbTi LHC IR quadrupoles was found to be  $0.39 \pm 0.11$  [13]. Moreover, the long-term dynamic effects were not found in next allowed harmonics,  $b_{10}$ .

#### 9.5 Z-scan with a 10-cm probe

At the end of the magnetic measurement program Z-scan at 4.5 K was performed with a 10-cm long probe. Due to limited length of the warm bore and probe insertion shaft, Z-scan was started at 44-cm above the geometrical center of the magnet moving toward the lead end. Scanning with a 10-cm probe gives us ability to examine the fluctuation of the harmonics in the body as well as to separate body from the lead end. Figures 84 and 85 summarize the normal and skew, low order harmonics as a function of z-coordinate (red dots and line). The green dots and line represent the results from the 81 cm probe measurements. One could see that they are in a good agreement.

As it was pointed out in Section 9.1 (see Table 6), the octupole field component was found large, about 8 units, at the center of the magnet. Moving toward the lead end, the octupole component decreases within the limits of  $\pm 1$  unit. The effect could be explained with some geometrical asymmetry (x vs. y) in the central segment of the magnet.



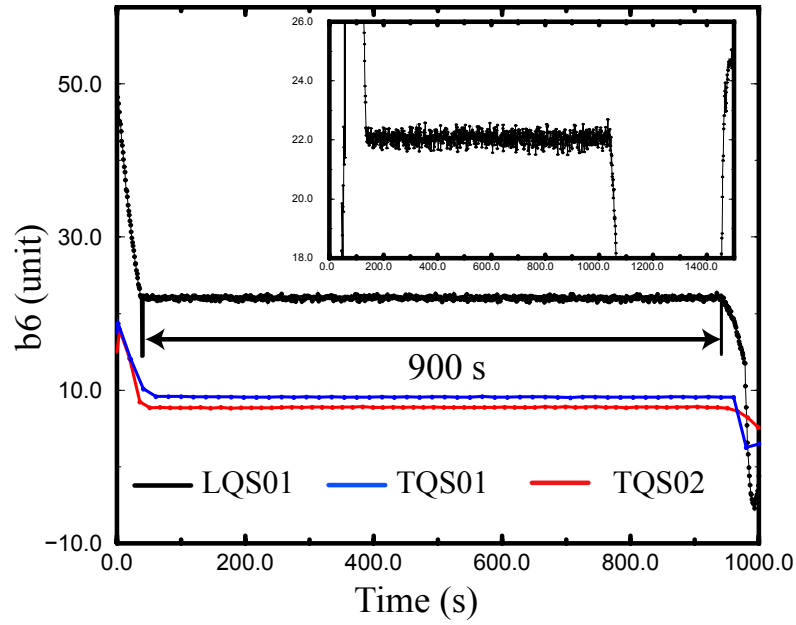


Fig. 83. Measurement of the decay and snapback of the dodecapole component for duration of injection of ~900 s in LQS and TQS magnets. No decay and snapback are observed.

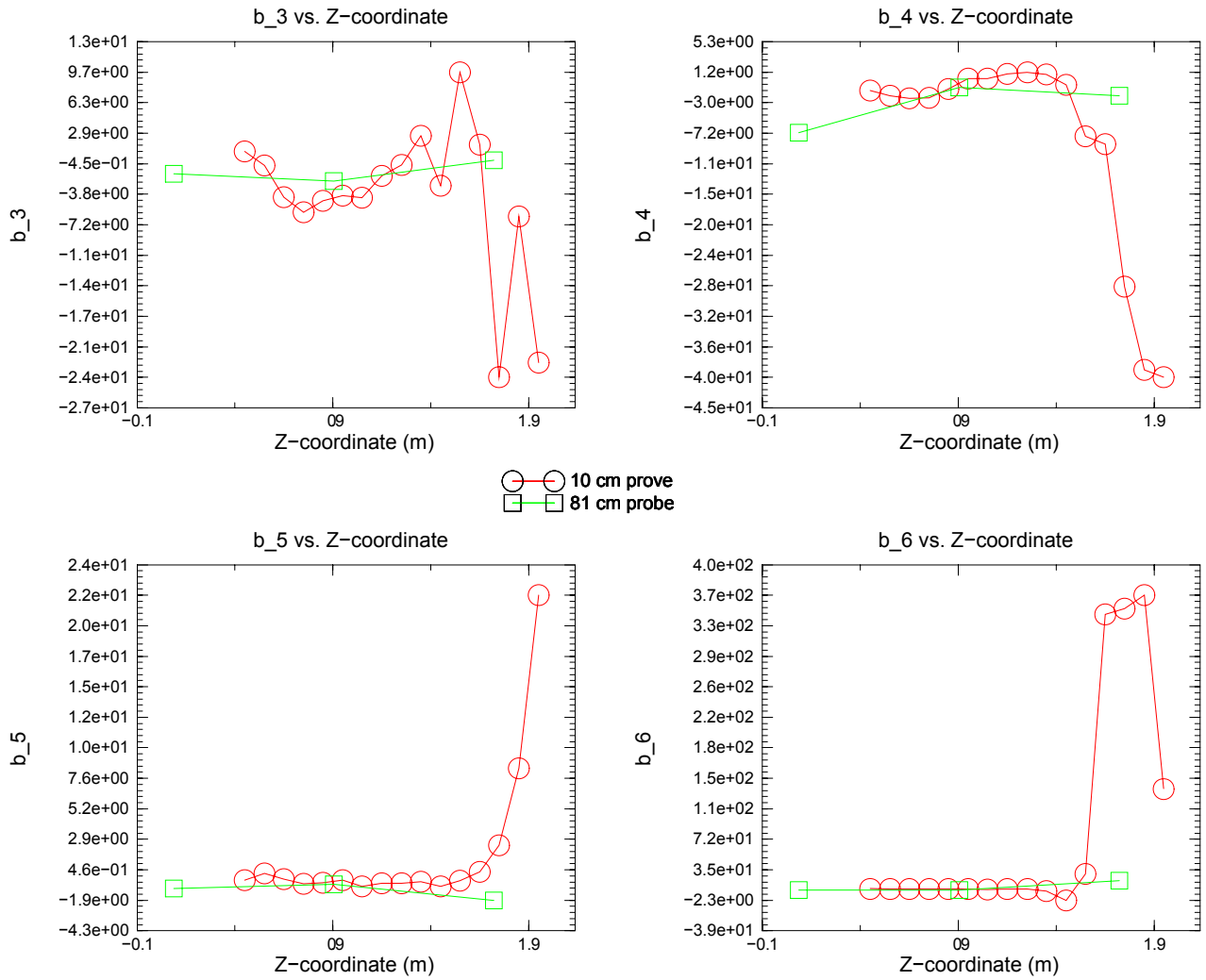


Fig. 84. Z-scan of LQS01b low-order normal harmonics (body and lead end) measured with a 10-cm probe (red dots and line) and 81-cm probe (green dots and line).

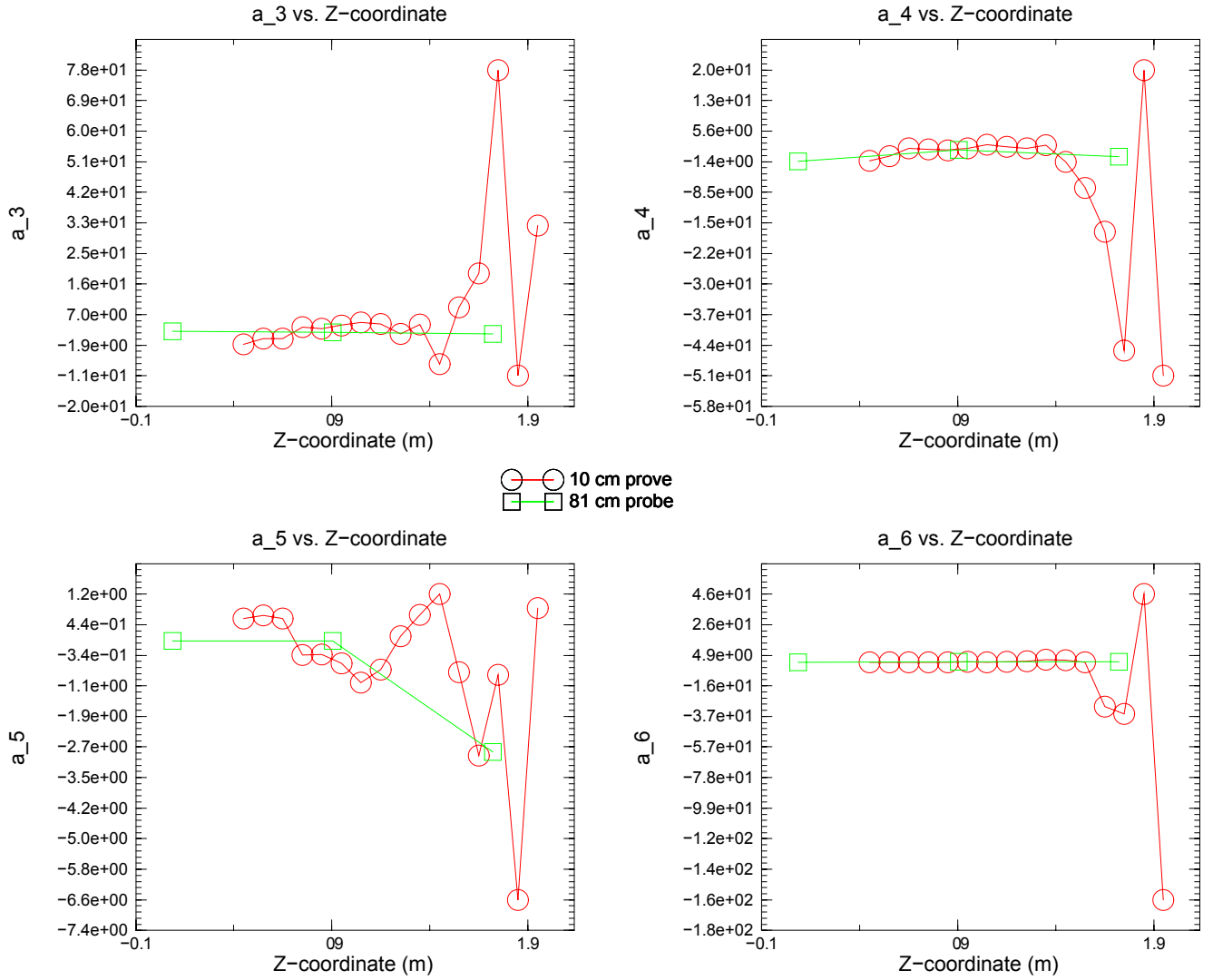


Fig. 85. Z-scan of LQS01b low-order skew harmonics (body and lead end) measured with a 10-cm probe (red dots and line) and 81-cm probe (green dots and line).

## 10. Spike Data Analysis

The voltage spike detection system (VSDS) based on a National Instruments PXI multifunction DAQ was used for study of thermo-magnetic instabilities in LQS01 magnet. The VSDS captures half-coil signals at a sampling rate of 100 kHz. More details on this system are presented in [14]-[15].

Due to large noise in the bucked half-coil signal of the VSDS no meaningful data was collected in TC1. This noise was correlated with the magnet current and its origin is not understood yet. No particular reasons were found for this noise during the VSDS checkout between the thermal cycles, but the current dependent noise was gone in TC2. Spike data was collected for 6 ramps in TC2.

Voltage spike Maximum as a function of the magnet current at 4.5 K in TC2 is shown in Fig. 86. Despite the low statistics LQS01b data is consistent with the LQS01a spike data (see Fig. 87).

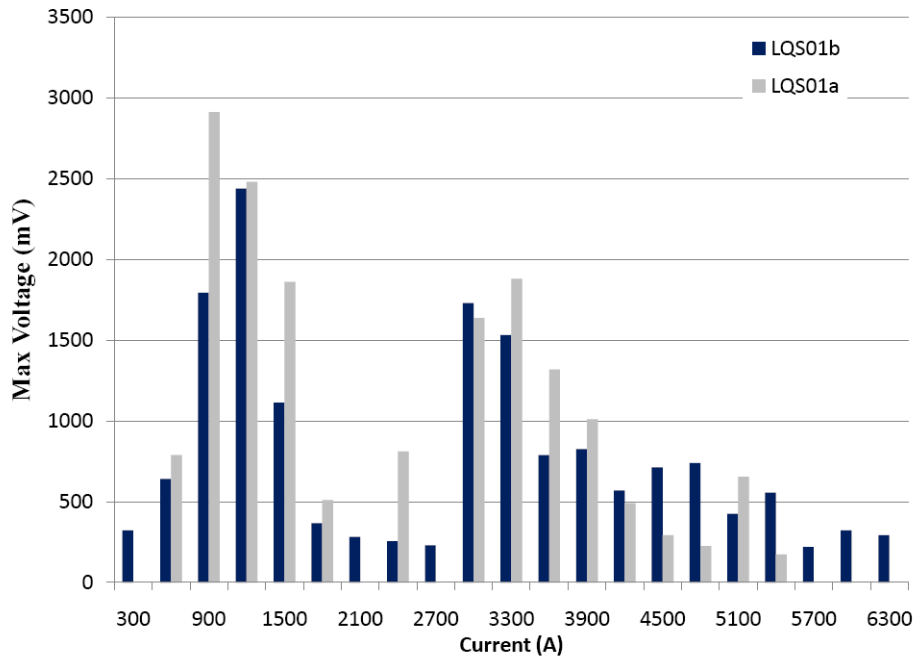


Fig. 86. Voltage spike maximum amplitude as a function of the magnet current at 4.5 K. Two-peak structure is a result of using different ramp rates: 200 A/s ramp rate up to 3 kA and 50 A/s above 3 kA.

Two-peak structure in spikes is caused by different ramping rates we used during the test. For the training quenches we were using 200 A/s ramp rate up to 3 kA, 50 A/s up to 5 kA, 20 A/s up to 9 kA and 10 A/s till magnet quench. Different ramp rates result in the different voltage spike distribution. From LQS01a test we know that spikes at high ramp rates are more localized and have smaller amplitude than at low high ramp rates (see Fig. 87). This was the main motivation for using high ramp rate (200 A/s) up to 3000 A during the LQS01 training – to pass through the high amplitude voltage spike region from 800 A to 3000 A.

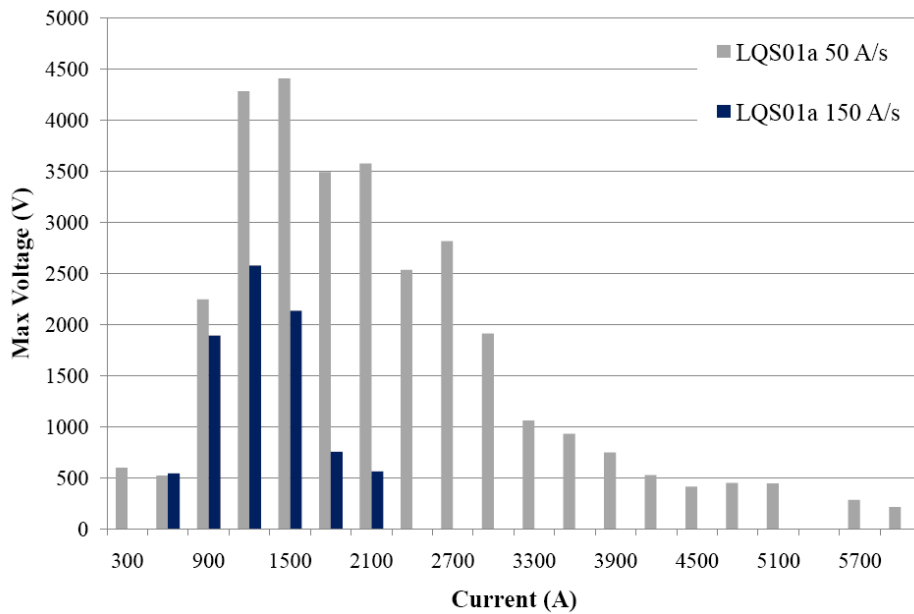


Fig. 87. Voltage spike maximum amplitude as a function of the magnet current at 4.5 K for different ramp rates.

## 11. Summary

The first LARP shell-type Nb<sub>3</sub>Sn Long Quadrupole (LQS01) made of 0.7-mm RRP strand with 54/61 sub-elements was disassembled and reassembled with higher and more uniform pre-stress after the first test in December 2009. Reassembled with the four original coils LQS01b performed exceptionally well by exceeding its target field gradient of 200 T/m and reproducing the performance of the best short model (TQS02c) made with the same type of conductor (RRP 54/61).

LQS01b reached 222 T/m ( $\sim 12.5$  kA) at 4.5 K. At 1.9 K the magnet reached 227 T/m (12.95 kA). The shallow slope of the temperature dependence, the large variations of the quench current and the temperature-dependent location of the quenches at temperatures 3 K and below, show that the limited stability of the conductor affected LQS01b performance below 4.5 K.

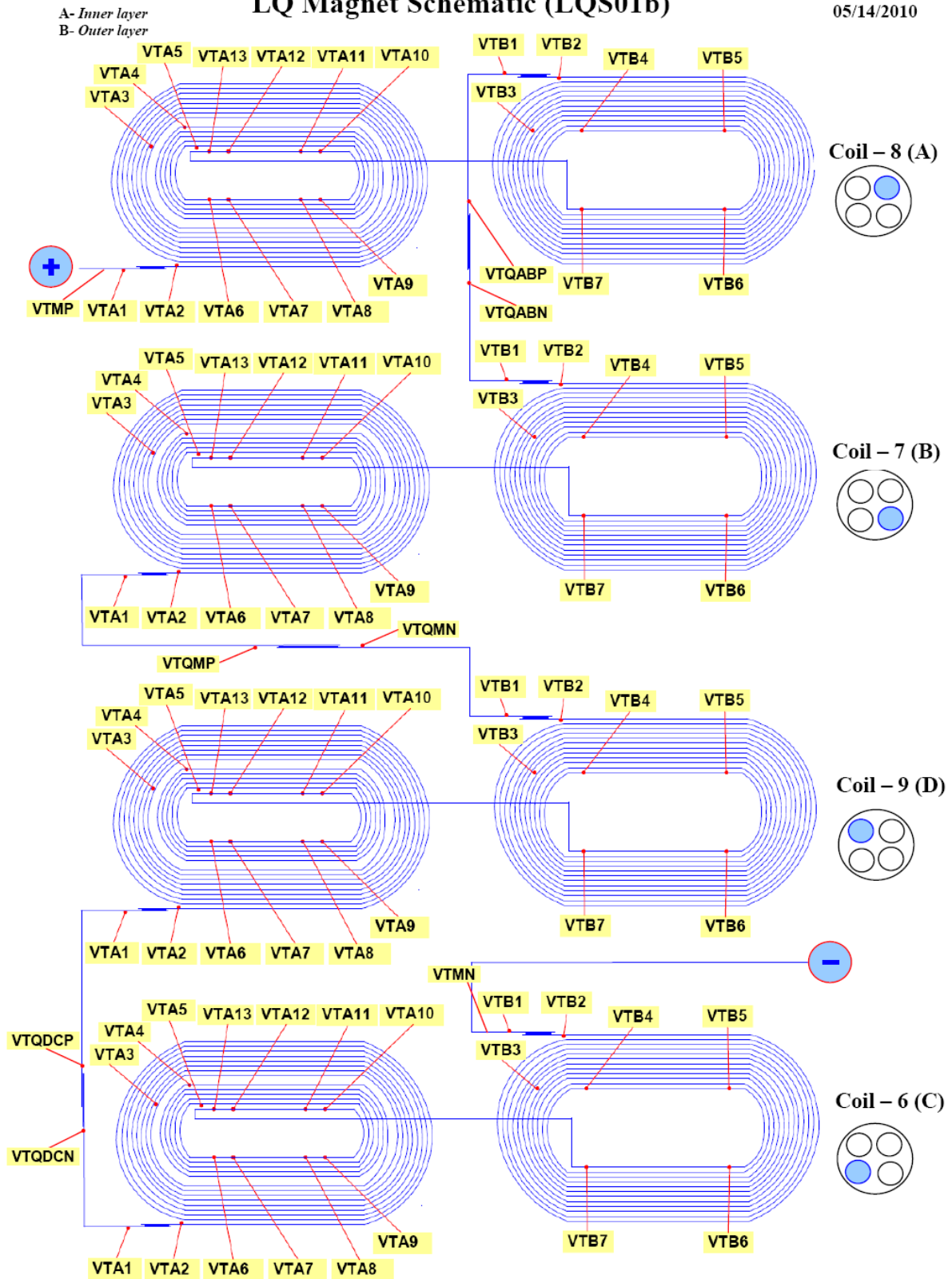
Since three coils were repaired during fabrication, LQS01b performance demonstrated that Nb<sub>3</sub>Sn coil fabrication technology has reached the level where long coils can be successfully fabricated and repaired. It also showed that a segmented shell-based structure can be successfully used for long Nb<sub>3</sub>Sn magnets, and that the quench protection tools used are adequate for protecting long Nb<sub>3</sub>Sn magnets.

## References

1. G. Chlachidze et al., “LARP LQS01 Magnet Test Summary”, TD-10-001, 2010
2. P. Ferracin et al., “Assembly and Loading of LQS01, a shell-based 3.7 m Long Nb<sub>3</sub>Sn Quadrupole Magnet for LARP”, *IEEE Trans. Appl. Supercond.*, accepted for publication.
3. P. Ferracin et al., “Mechanical performance of the LARP Nb<sub>3</sub>Sn quadrupole magnet LQS01”, Proceedings ASC2010, Washington DC (2010)
4. G. Ambrosio et al., “Final Development and Test Preparation of the First 3.7 m Long Nb<sub>3</sub>Sn Quadrupole by LARP”, *IEEE Trans. Appl. Supercond.*, accepted for publication
5. G. Ambrosio, et al., “Long Quadrupole Design Report”, LARP report available on-line: [https://plone.uslarp.org/MagnetRD/longquad/LQ\\_DR.pdf](https://plone.uslarp.org/MagnetRD/longquad/LQ_DR.pdf) and <http://tiweb.fnal.gov/website/controller/1505>
6. H. Felice, et al., “Performance of a Nb<sub>3</sub>Sn quadrupole under high stress”, Proceedings ASC2010, Washington DC (2010)
7. A.V. Zlobin, et al., “R&D of Nb<sub>3</sub>Sn accelerator magnets at Fermilab”, *IEEE Trans. Appl. Supercond.* Vol 15, 2005, p. 1113.
8. S. Russenschuck, “*Field Computation for Accelerator Magnets*”, Wiley-VCH, 2010.
9. R.C. Bossert et al., “Development and Test of LARP Technological Quadrupole Models of TQC Series”, *IEEE Trans. Appl. Supercond.*, Vol. 18, 2008, pp. 175-178
10. D. A. Finley et al., “Time dependent chromaticity changes in the Tevatron”, in Proc. 1987 PAC, Washington, DC, 1987, pp. 151-153.
11. G.V. Velez et al., “Measurements of the Persistent Current Decay and Snapback Effect in Tevatron Dipole”, *IEEE Trans. Appl. Supercond.*, vol. 17, 2007, pp. 1105-1108.
12. V.V. Kashikhin et al., “Field Quality Study in High-field Nb<sub>3</sub>Sn Accelerator Magnets”, Proc. of 2005 Particle Accelerator Conference, Knoxville, TN, May 2005, pp. 366-338.
13. G.V. Velez et al., “Magnetic Field Measurements of LHC Inner Triplet Quadrupoles Fabricated at Fermilab”, *IEEE Trans. Appl. Supercond.*, Vol. 17, 2007, pp. 1109-1112.
14. B. Bordini et al., “Voltage spikes in Nb<sub>3</sub>Sn and NbTi Strands”, *IEEE Trans. Appl. Superconduct.*, Vol. 16, Issue 2, June 2006, pp 366-369
15. D.F. Orris et al., “Voltage Spike Detection in High Field Superconducting Accelerator Magnets,” *IEEE trans. Appl. Superconduct.*, Vol. 15, Issue 2, June 2005, pp 1205-1208

## LQ Magnet Schematic (LQS01b)

05/14/2010



## Attachment II

### Thresholds for the Half-coil signals in FPGA based system:

#	Current Range	Threshold
1	0-400 A:	0.8 V
2	400-1500 A:	2.5 V
3	1500-3000 A:	2.5 V
4	3000-3600 A:	4.0 V
5	3600-4000 A:	3.0 V
6	4000-5000 A:	2.6 V
7	5000-6000 A:	1.8 V
8	6000-8000 A:	0.8 V
9	8000-15000 A:	0.8

### Thresholds for the Half-coil signals in VME based system:

#	Current Range	Threshold
1	0-500 A:	0.8 V
2	500-6000 A:	3.2 V
3	6000-15000 A:	0.8 V